UNIVERSITÉ DE GRENOBLE

THÈSE

Pour obtenir le grade de

DOCTEUR DE L'UNIVERSITÉ DE GRENOBLE

Spécialité : **Physique / Nanophysique**

Arrêté ministériel : 7 août 2006

Présentée par

Yulia KOTSAR

Thèse dirigée par **Eva MONROY**

préparée au sein du **Laboratoire Nanophysique et Semi-Conducteurs (CEA / INAC / SP2M)**
dans **l'École Doctorale de Physique**

Puits quantiques GaN/Al(Ga)N pour l'optoélectronique inter-sous-bande dans l'infrarouge proche, moyen et lointain

Thèse soutenue publiquement le **8 octobre 2012**
devant le jury composé de :

M Fernando CALLE
Rapporteur
M Yvon CORDIER
Rapporteur
M Henri MARIETTE
Président
M Guillaume CASSABOIS
Membre
Mme Eva MONROY
Membre
M Eric TOURNIE
Membre
Mme Agnes TRASSOUDAINE
Membre

Acknowledgement

This manuscript is an outcome of my research within the group of 'Nanostructures and Semiconductor' at Institute for Nanoscience and Cryogenics at CEA-Grenoble, France. For three years I had a chance to meet and to work with researchers who have a passion to science, hence it is a pleasure for me to express my most profound appreciation to all of them.

First of all I would like to express my graditude to my thesis supervisor Dr. Eva Monroy for her expert guidance, patience and constatnt encourgement along these three years. Thank you for fostering a positive atmosphere in the team and your boundless energy - that was really a pleasure to be a part of the group. Along the way, I have learned a lot from you and not only about the Nitrides!

I consider it is a great pleasure to express my thanks to Prof. Henry Mariette, Director of the group and Prof. Jean-Michel Gerard, Director of the SP2M for welcoming me to the lab and giving me the opprtunity to perform my research, which was posible as well thanks to the Europeen Project UNITRIDE (EU-FP7-STREP 233950).

I extend my thanks to the members of the jury for their time and for making all the way to Grenoble. To Prof. Fernando Calle and Yvon Cordier, the reporters of this work, for helpful comments and advices on the manuscript. To Prof. Guillaume Casabois, Prof. Eric Tournie and Prof. Agnes Trassoudaine for showing interest to the work and for interesting disscutions after the presentation.

I would further like to express my appreciation to all collaborators of Unitride Project for their excellent cooperation and efforts in achieveing common goals. Prof. Gad Bahir and his group at Technion for fast feedbacks on the samples and for contribution in electrical measurements of QCDs. To Prof. Francois Julien and his group at Universite Paris-Sud for valuable inputs on design of QCDs. To the group of Prof Nicolas Grandjean at EPFL, Swiss for fruitful collaboration.

I am thankful to all colleages who made a contribution to this work and with whom I had an opportunity to work throughout these three years. To Yoann, Yann, Jean and Rudi for always being available in the MBE crysis moments, to Edith and Stephanie for teaching me XRD technique, to Lucien for AFM trainings, to David and Florence for valuable FTIR discutions and for regularly ‘donating’ me their spectrometer, to Eirini for her numerous TEM images, to Joel for ‘waveguide discussions’, to colleagues from PTA for training me on different clean room equipments, and etc etc.

I would like to thank previous members of the group, clan of Prem and Alex, thank you for transferring your experiense to young generation and for the inteligent jokes. Aparna, for being the perfect officemate – we’ve successfully proved the possibility of 12-m^2-contradiction-theory. Fernando, for always being ready to listen about ISB challenges. Sirona, Buk and Mark, the current members of the group, I wish you all success in achieving your goals! I thank previous and current ‘thesards’ and ‘postdoctorants’ of SP2M for the nice atmosphere in the lab: Nitin, Sandeep, Gabriael, Vancent, Robert, Priya, Dipanka, Xiaojun, Rafa, Laura, Adrien, Damien, Karine, Diane and etc.

I am thankful to friends I made in France: to Anna, Vadim, Stéphanie, Francesco, Agnieszka, Rra..Laurent, Dilya, Rita, Emeline… Thanks for sharing my passion to sports and for reminding me that a PhD student should also have a life! Grenoble is a wonderful place to be, and I am grateful for having been able to spend time here!

В заключение хочу поблагодарить мою семью, которая является надежным тылом на протяжении всех моих ‘Европейских приключений’. Спасибо за поддержку и понимание!

Yulia / Юлия

Résumé

Ce mémoire résume des efforts dans la conception électronique, la croissance épitaxiale et la caractérisation des puits quantiques GaN/Al(Ga)N qui constituent la région active des composants inter-sous-bande (ISB) à base de semi-conducteurs nitrures pour l'optoélectronique dans l'infrarouge proche, moyen et lointain. Le dessin des puits quantiques GaN/Al(Ga)N pour ajuster la longueur d'onde d'absorption dans le spectre infrarouge a été réalisé en utilisant la méthode k.p à 8 bandes du logiciel Nextnano3 pour la résolution des équations de Schrödinger-Poisson. Les structures ont été synthétisées par épitaxie par jets moléculaires assistée par plasma (PAMBE).

Les trois premiers chapitres sont généraux. Le premier chapitre présente l'état du domaine et précise les objectifs de la thèse. Cette partie se termine par une description du contenu des chapitres suivants.

Le second chapitre précise les propriétés des nitrures du groupe III. Ce chapitre rappelle tout d'abord les différentes formes cristallines que peuvent prendre ces semiconducteurs, notamment la forme wurtzite qui est la plus stable, et explicite le problème de polarité, qui conduit à la présence du champ piézoélectrique interne spontané, et sa relation à l'orientation cristalline. Je commente ensuite la structure de bande de ces matériaux et leur dépendance à la température, ainsi que les valeurs de masse effectives publiées pour les électrons et les trous. Les propriétés élastiques sont ensuite précisées et utilisées pour évaluer les déformations attendues dans les matériaux contraints. Les polarisations engendrées par les piézoélectricités spontanée et induite par les déformations sont enfin précisées et leur effet sur la structure de bande des puits quantiques rappelée. Ensuite sont décrites les transitions inter-sous-bande, leurs règles de sélection ainsi que les effets multi-corps en présence de dopages élevés, qui amènent à des corrections dans le calcul des transitions entre les niveaux électroniques.

Le troisième chapitre décrit les techniques expérimentales sollicitées dans ces travaux. Je discute d'abord de la technique d'épitaxie qu'elle a utilisée, la technique d'épitaxie par jets moléculaires assistée par plasma. Après en avoir rappelé brièvement les principes généraux, le bâti utilisé est décrit. Le principe de la technique de

diffraction électronique en incidence rasante (RHEED) est ensuite présenté, ainsi que les informations qui peuvent en être tirées sur l'évolution du paramètre de maille du matériau en croissance, l'arrangement atomique de sa surface et la vitesse de croissance. Le chapitre se termine par une description des substrats utilisés et une présentation des techniques de caractérisation, diffraction de rayons X, microscopie à force atomique, spectroscopie de luminescence et spectroscopie infrarouge de type FTIR, mises en jeu dans ces travaux.

Dans le quatrième chapitre, les problèmes de gestion de la contrainte qui apparaissent liés au désaccord de maille pendant la croissance épitaxiale des hétérostructures GaN/Al(Ga)N sont investigués par combinaison de techniques *in-situ* et *ex-situ* pour deux séries de trois échantillons épitaxiés sur des tremplins GaN sur saphir avec d'un côté des couches tampon GaN et de l'autre des couches tampon AlGaN présentant la même teneur en aluminium que les couches AlGaN dans les superréseaux. L'étude commence par une analyse RHEED de la variation du paramètre de maille du matériau à la surface durant la croissance des superréseaux. En premier lieu et pour tous les échantillons on observe une oscillation périodique du paramètre de maille en surface lors de l'épitaxie des couches successives GaN et AlGaN. Cette oscillation est de nature élastique et en relation avec la saturation en gallium de la surface qui dépend de la composition du matériau sous-jacent. En plus de ce phénomène, on peut dans la plupart des cas observer une autre évolution du paramètre de maille, plus lente et attribuée à la relaxation des contraintes dans les couches. Cette relaxation n'est pas décelable pour les super-réseaux avec une teneur en aluminium de x=10% ou 30% réalisés sur couche tampon GaN alors qu'elle l'est pour les mêmes structures réalisées sur des couches tampon AlGaN avec des teneurs x=10% et 30%. Enfin, pour des super-réseaux avec des teneurs en aluminium de 44%, une relaxation rapide est observée quelle que soit la couche tampon utilisée. Une étude systématique par diffraction des rayons X confirme les conclusions précédentes quant à la présence de relaxation ou non des contraintes dans les différentes couches analysées. Une analyse par microscopie électronique en transmission vient compléter ces mesures.

Pour obtenir une absorption ISB efficace, on a besoin de niveaux élevés de dopage au silicium dans le puits quantiques, situation dans laquelle les théories à une particule conduisent à des déviations significatives par rapport aux résultats expérimentaux.

Donc une étude du dopage au silicium des super-réseaux GaN/Al(Ga)N pour les régions spectrales infrarouges proche et moyen est présentée dans le chapitre cinq. Dans cette étude, trois séries d'échantillons ont été réalisées avec des superréseaux AlN/GaN d'une part, et AlGaN/GaN avec des teneurs en aluminium de 10% et 20% d'autre part ; les niveaux de dopage avec le silicium se situent entre 5×10^{18} cm^{-3} et 2×10^{20} cm^{-3}. Des calculs réalisés au moyen d'un logiciel dénommé nextnano3 montrent que les effets attendus avec une élévation du niveau de dopage sont une augmentation de la longueur d'onde des transitions ISB en raison de l'écrantage des champs électriques internes. Cependant, les effets multi-corps non traités par ce logiciel peuvent mener à une diminution de la longueur d'onde. Effectivement, l'analyse FTIR de l'absorption inter-sous-bande dans ces échantillons montre de manière globale la prédominance des effets multi-corps, et de fait, que les structures ISB ne peuvent être traitées avec des modèles à une seule particule.

Le chapitre six est consacré aux détecteurs cascade quantique (QCD) opérant dans le proche et le moyen infrarouge. Après un bref rappel sur les avantages et inconvénients des détecteurs classiques à base de puits quantiques, notamment à base de matériaux arséniés, sont introduits le principe et les avantages potentiels des QCD. L'intérêt d'utiliser la filière GaN est notamment l'extension de la gamme des longueurs d'ondes et la rapidité de détection liée à l'interaction electron-phonon. Le premier détecteur étudié cible la gamme des télécommunications autour de 1.5 µm. Après une description de l'empilement des couches (AlN/GaN pour la détection ; AlN/AlGaN pour l'extraction) et de sa modélisation, une série de caractérisations structurales a été menée et montre le contrôle des épaisseurs et de la planéité des couches. Les autres détecteurs étudiés visent la gamme 3-5 µm avec des structures où les puits quantiques GaN sont plus épais et les barrières AlN sont remplacées par des barrières AlGaN dans la zone active aussi bien que dans la zone d'extraction. Deux séries de structures avec des barrières AlGaN avec des teneurs en aluminium x=35% et x=65% sont étudiées en vue d'une absorption attendue à 4 µm et 3.3 µm respectivement. Les analyses structurales par microscopie électronique montrent une différence de qualité en faveur des structures à plus faible teneur en aluminium. Dans chaque série, l'effet du niveau de dopage silicium des puits quantiques GaN sur l'absorption et la réponse de détecteurs photovoltaïques est également étudié. Comme

précédemment, un décalage de l'absorption vers les plus faibles longueurs d'onde est observé avec l'augmentation du niveau de dopage. La réponse de deux photodétecteurs montre un pic pour chaque longueur d'onde visée pour les structures présentant les plus faibles niveaux de dopage; les structures avec des niveaux de dopage plus importants ne montrent pas d'effet photovoltaïque. La détection évidente à 14 K décroît pour disparaître au-delà de 80 K.

Le septième chapitre est consacré à la réalisation d'une structure capable d'absorber des radiations dans le domaine THz (longueurs d'onde comprises entre 30 et 1000 µm). Il décrit une structure de couches semiconductrices constitué d'un puits quantique en échelon $GaN/Al_xGa_{1-x}N$ x=5% entouré de barrières $Al_xGa_{1-x}N$ x=10%. Ce dessin particulier est intéressant pour obtenir des écarts en énergie plus faibles. La présente structure visant une absorption à 4.3 THz est réalisée sur un tremplin GaN sur substrat de silicium. Les analyses structurales confirment la bonne qualité cristalline de la zone active et l'absorption à 4.3 THz est obtenue comme attendu en mode de polarisation TM.

Finalement, le huitième et dernière chapitre tire des conclusions et donne quelques perspectives en ce qui concerne l'amélioration de la qualité cristalline des matériaux.

Index

1 Introduction and targets 1
1.1 Introduction to III-nitride semiconductors 1
1.2 III-nitrides for infrared optoelectronics: Motivation and targets 2
1.3 Organization of the manuscript 6

2 Introduction to III-nitride semiconductors and intersubband transitions 9
2.1 Properties of III-nitride semiconductors 9
2.1.1 Crystalline structure and polarity 9
2.1.2 Band structure of III-Nitrides 12
2.1.3 Spontaneous and piezoelectric polarization 15
2.2 Physics of intersubband transitions 18
2.2.1 Selection rules 18
2.2.2 Many-body effects 20

3 Experimental techniques 23
3.1 Plasma-assisted molecular beam epitaxy 23
3.1.1 PAMBE equipment 23
3.2 PAMBE growth of III-Nitrides 27
3.2.1 Heteroepitaxial growth 27
3.2.2 Strain relaxation in GaN/Al(Ga)N heterostructures 29
3.2.3 Growth of GaN 31
3.2.4 Growth of AlN 35
3.2.5 Growth of AlGaN 35
3.3 Characterization techniques 36
3.3.1 X-Ray Diffration 36
3.3.2 Atomic Force Microscopy 38
3.3.3 Photoluminescence 39
3.3.4 Fourier Transform Infra-Red Spectroscopy 40
3.4 Substrates 43
3.5 Sample preparation from FTIR spectroscopy 45

4 Strain relaxation mechanicsms in GaN/AlGaN superlattices 47
4.1 Introduction 47
4.2 GaN/AlGaN superlattices: Electronic structure 49
4.3 Growth conditions for GaN/AlGaN SLs 52
4.4 Strain measurements 53
4.5 Conclusions 66

5 Effect of the QW doping on ISB absorption in GaN/Al(Ga)N SLs 67
5.1 Modeling of the superlattice electronic structure 68
5.2 Silicon location 70
5.3 Effect of Si on the interband optical properties 72
5.4 Effect of Si on the ISB optical properties 75
5.5 Conclusions 78

6 Near- and mid-IR quantum cascade detectors 79
6.1 Quantum Cascade Detector: Motivation and working principle 79
6.2 QCD for fiber optics telecommunication 82
6.3 QCD for 3-5 µm spectral range 86
6.4 Conclusions 96

7 Terahertz ISB absorption 97
7.1 Motivation 100
7.2 Step-QW superlattices for terahertz absorption 104

8 Conclusions and perspectives 105
8.1 Conclusions 105
8.2 Perspectives 106

References 109

Glossary 117

Publications and conference contributions 119

Chapter 1

Introduction and targets

1.1 Introduction to III-nitride semiconductors

The III-nitride semiconductors are the important and auspicious materials for optoelectronic and electronic applications. Being direct wide bandgap semiconductors III-nitrides are the choice for light-emitting diodes (LED) to cover spectral range from deep UV (high Al content AlGaN/GaN system) to green (InGaN/GaN system) using quantum wells (QWs) as an active media. III-nitride LEDs have already found a number of applications, including indoor and outdoor illumination, traffic and emergency vehicle signals, data storage, water purification, disinfection of medical tools and etc. LED technology, prompted by spectacular progress in terms of efficiency, output power and spectral coverage in the last two decades, is a rapidly progressing field of research.

GaN technologies as well are very promising for high-power applications in the microelectronics field. III-nitrides have superior material properties, such as higher electrical breakdown field (from 3.3 MV/cm for GaN to 11.7 MV/cm for AlN), high electron mobility ($\approx$ 2000 $cm^2/V{\cdot}s$), and wide bandgap (from 3.4 eV for GaN to 6.2 eV for AlN) in comparison with conventionally used for electronic components Si or GaAs material systems. GaN-based devices demonstrate superior performance in terms of breakdown voltage, current capacity, high frequency, efficiency and reduced size of the power modules.

Another prospect field for III-nitride materials is photovoltaics. The interest to III-nitrides for solar application stems from the possibility to make InGaN alloys optically active over the full spectrum of sunlight. This is an alternative to multi-junction cells approach with potential efficiency up to 60% (compared to the theoretical limit of 30% for silicon technology). However, due to immature epitaxial growth methods for In-

rich alloys and insufficient knowledge of material properties, only preliminary prototypes for InGaN solar cells have been reported, leaving a space for future research activities (Wu, 2009; Lang, 2011).

However, the GaN technology has several drawbacks associated to the defect structure of epitaxial films and the lack of cheap substrates for homoepitaxial growth. In order to make III-nitrides an economically-competitive technology, silicon wafers are pursued as an alternative substrate choice. However, GaN and AlGaN layers are highly strained when epitaxially deposited on Si substrates with <111> crystal orientation and a large difference in thermal coefficients between GaN and Si leads to decohesion and cracking. However, recent progress on in situ growth monitoring methods has made it possible to produce GaN on 8 inch silicon wafers using metalorganic chemical vapor deposition (MOCVD).

2.1 III-nitrides for infrared optoelectronics: Motivation and targets

As described above, GaN-based semiconductors have rapidly become the materials of choice for UV-blue-green optoelectronics and white lighting. Much less effort has been devoted to InN and In-rich alloys, which appeared as the natural nitride-based choice for red optoelectronics. A major breakthrough in 2002, stemming from much improved quality of InN films grown using molecular beam epitaxy (MBE), resulted in the bandgap of InN being revised from 1.9 eV to a much narrower value of 0.64 eV (~1.9 µm wavelength) (Davydov, 2002). This finding extended the interband optoelectronic capabilities of the III-nitride family into the infrared (IR) spectral region. However, this IR technology is penalized by the high residual doping, poor thermal stability and surface effects characteristic of InN (Wu, 2009).

Thus, an alternative approach, using intersubband (ISB) transitions, has been proposed to develop an IR technology. The IR spectral region is well covered with optical devices based on the III-As and III-P material systems (Fig. 1.1). ISB devices, mainly detectors and lasers for applications in gas sensing, medicine and chemical industry, using GaInAsN/AlAs (Ma, 2007), GaAs/AlGaAs (Gunapala, 2005; Walther, 2007) GaInAs/AlAsSb (Yang, 2006; Giorgetta, 2007) have been well developed and

can be tuned from mid- to far-IR regions. However, this technology cannot be easily extended to the near-IR due to the small conduction band offset of these materials, neither can it cover the range from 30 to 40 µm (Adachi, 1994), which correspond to the Reststrahlen band in arsenides. With the large conduction band offset between GaN and AlN (≈1.75 eV) and the progress achieved in epitaxial growth of thin III-N films, the gaps in As technologies are now accessible using III-nitride materials. In contrast to InAs/AlSb materials, the lateral valleys of GaN and AlN are placed high in energy, which opens prospects for near-IR ISB light emitters.

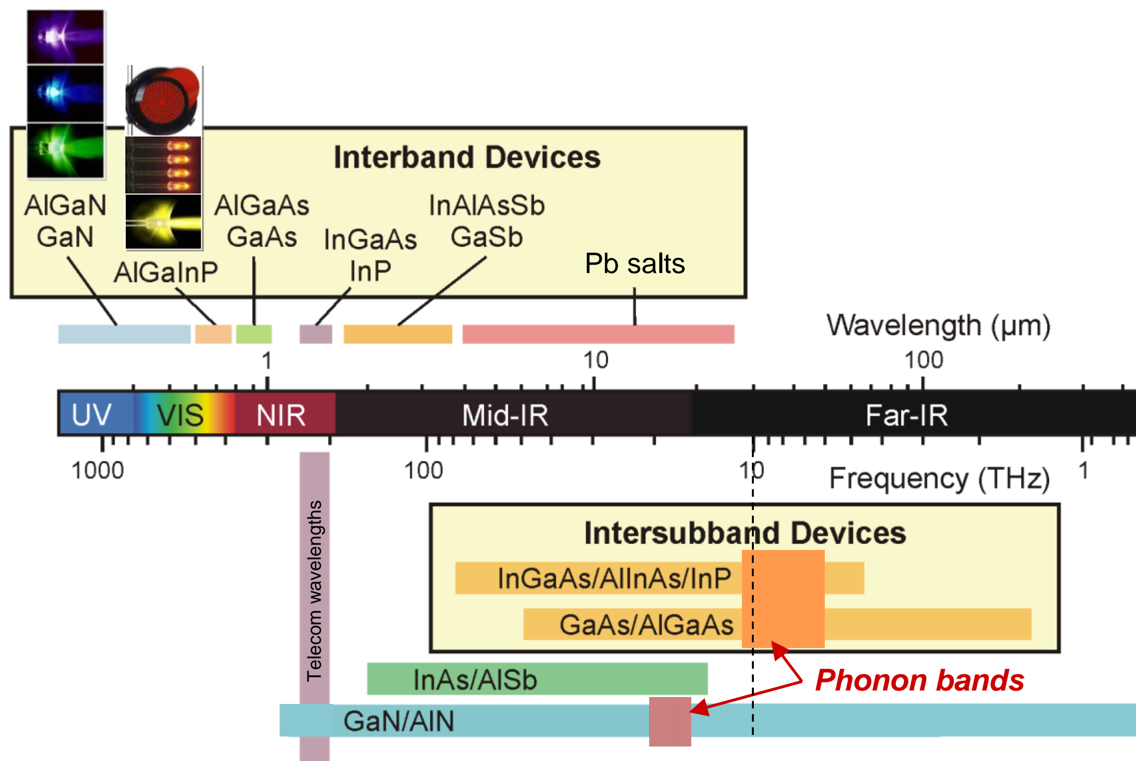

Figure 1.1. *Spectral coverage by interband and ISB devices based on different material systems.*

On the other hand, III-nitrides have a potential for operation in terahertz (THz) region, which has a variety of applications such as information and communication technology, quality and environment monitoring, security and medical screening, etc. In 2002, the first As-based THz quantum cascade laser (QCL) was demonstrated, with operation wavelength peaked at 4.4 THz (Khöler, 2002). QCLs rely on transitions between quantized conduction band states of a suitable designed semiconductor multi-quantum-well structure (Faist, 1994). These devices are in-plane emitters, with the

electric-field vector perpendicular to the plane of the layers. Figure 1.2 shows a schematic description of the active region. An electron injected into the active region undergoes first a lasing transition between the two sublevels (3 → 2) of the active region, and is rapidly extracted to the lowest sublevel (2 → 1) by a fast non-radiative transition, which maintains the population inversion. Then, the electron must tunnel through the miniband in the next injector region towards the upper level of the second active region. By using several tens or even 100 periods in a series (a cascade), higher optical gain and multiple photons per electron are obtained. The emitting wavelength can be tuned in the range from a few microns to well above 10 μm, by changing design parameters, such as the quantum well (QW) thickness and barrier height. In the THz spectral region, the lower radiative state is resonantly coupled into the upper injector level, which is separated by approximately the LO-phonon energy (E_{LO} = 36 meV in GaAs) from the second injector level, providing a fast relaxation path towards the upper radiative state.

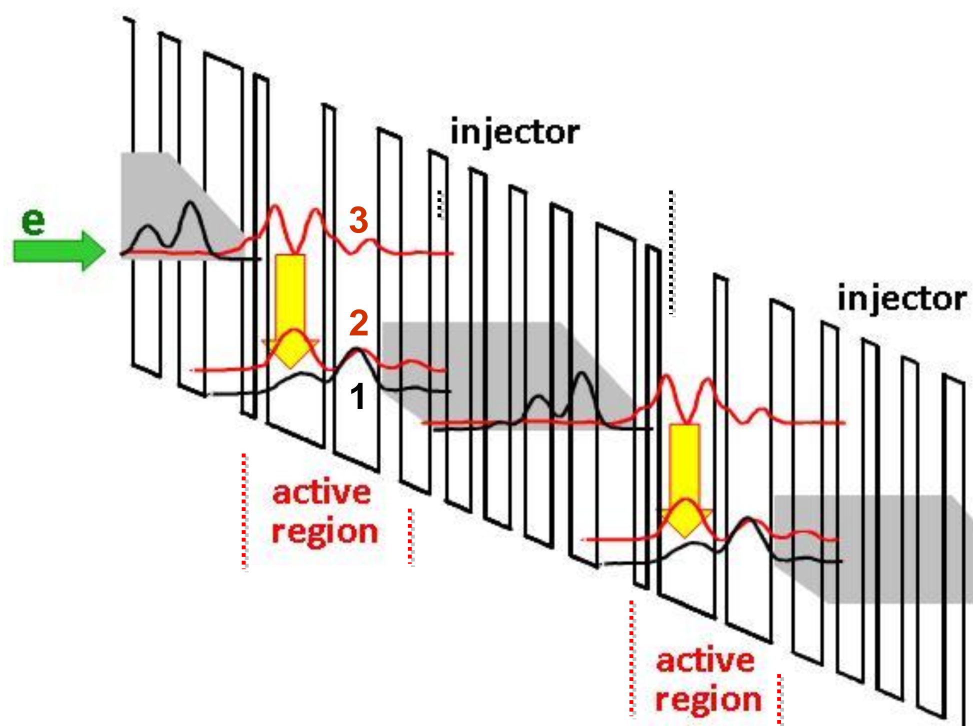

Figure 1.2. *Schematic presentation of the conduction band profile of a GaAs/AlGaAs QCL.*

Rapid progress has been made in terms of device performance. To date, THz QCLs have been demonstrated in the 0.85-5 THz range (Scalari, 2009), with pulsed operation up to 186 K (Williams, 2007; Kumar, 2009), and output powers of up to 250 mW pulsed (Williams, 2001). However, GaAs-based QCLs have limitations regarding their operation temperature, and thermal backfilling and thermally activated phonon scattering make impossible operation of the device at room temperature. These drawbacks can be overcome using III-N material systems, thanks to their large LO-phonon energy of GaN (92 meV), which significantly exceeds the room-temperature thermal energy. As well, strong electron-phonon interaction provides possibility to perform ultrafast devices with rapid depopulation of the lower laser state (Iizuka, 2000).

The aim of this work was to improve the performance and the understanding of the material issues involved in the GaN/AlGaN ISB technology. As optical and electrical performance of the ISB devices depends on the quality of the epilayers it is important to study the issues like strain management in the device active region, i.e. in GaN/AlGaN SLs. Furthermore, targeting longer wavelength (smaller e_1-e_2 energy separation) implies enhanced doping of the heterostructures in order to observe ISB absorption. Therefore considerable attention has to be devoted to silicon doping and the associated many-body effects. With this knowledge, I have contributed to the development of prototypes of ISB detectors for near- and mid-IR spectral region based on the quantum cascade principle.

This work was a part of the European project (UNITRIDE, FP7 FET-Open #233950), initiated on May 2009, which aimed at the assessment of the III-nitride ISB technology for the development of a new generation of high-performance IR optoelectronic devices.

My task was first simulation by Nextnano^3 8-band k.p Schrödinger-Poisson solver of the electronic structures of ISB heterostructures targeting certain operation wavelength. Following the design, I was in charge of the growth of superlattice (SL) structures using plasma-assisted molecular beam epitaxy (PAMBE). In particular, I studied the strain relaxation in nitride heterostructures and modified the growth conditions to minimize the generation of defects. To probe the material properties and

the quality of the grown layers, I used X-ray diffraction (XRD), atomic force microscopy (AFM), photoluminescence (PL) spectroscopy and Fourier Transform Infrared Spectroscopy (FTIR). The IR optical and electro-optical characterization of the samples was performed as well at the University Paris-Sud in the group of Prof. F.H. Julien or in Technion (Israel) in the group of Prof. G. Bahir. Some additional studies, like the effect of annealing on the Si diffusion, were performed in collaboration with Prof. D. Hofstetter in the University of Neuchâtel (Switzerland). Transmission electron microscopy was performed under the supervision of Dr. Eirini Sarigianidou (INPG, Grenoble).

1.3 Organization of the manuscript

This thesis is a contribution to the study of PAMBE-grown III-nitride heterostructures designed to exhibit ISB absorption in the IR spectral region. It starts with this introductory ***chapter 1*** which gives a short overview of advantages and challenges associated to the wurtzite III-nitride material system. Particularly, I present the key application fields for III-N semiconductors and justify the motivation of this work.

Chapter 2 introduces the properties of the material which lies in the base of this work. The crystalline structure with its inherent polarity feature, electronic properties and internal electric fields in wurtzite III-N semiconductors are discussed. The second part of the chapter describes principle of ISB transitions, their selection rules and many-body effects, as a correction to two-level single particle theory.

Chapter 3 is devoted to the description of the deposition technique and the key growth conditions required for the synthesis of III-nitride heterostructures by PAMBE. The methods for calibrating the growth rate and composition of the alloys are introduced. In the last section of the chapter, I describe key the work principle of the main techniques used for optical and structural characterization: as X-ray diffraction spectroscopy (XRD), atomic force microscopy (AFM), photoluminescence (PL) and Fourier Transform Infra-Red (FTIR) spectroscopy.

The active region of the devices based on ISB transitions consists of GaN/AlGaN QWs, coupled QWs or superlattices, and strain issues arise due to the large lattice mismatch between the layers. ***Chapter 4*** presents studies of the misfit relaxation mechanisms in GaN/AlGaN SLs as a function of Al composition in the buffer and barrier layers. In order to have a complete insight to the mismatch outcome, *in-situ* and *ex-situ* measurements of strain relaxation are combined and discussed.

Chapter 5 focuses on the studies of silicon doping of the structures targeting the near- and mid-IR spectral regions. Carrier concentration is a crucial parameter for the observation of ISB transitions, therefore the optimal doping level is identified and the many-body effects appearing in highly doped structures are discussed. The experimental results are compared with the predictions by nextnano^3 8-band k•p Schrödinger-Poisson solver.

In ***chapter 6***, I present the contributions to the domain of IR detectors based on the quantum cascade principle. The first quantum cascade detector with operation at the fiber-optic telecommunication wavelength of ≈1.5 μm is presented. I show the potential of the structures targeting longer wavelength detection and the issues related to the structure quality and optimal doping level which limit the device performance.

Finally, ***chapter 7*** presents the first attempt of performing III-nitride ISB heterostructure targeting the far-IR spectral region. The chapter starts by introducing the approach to engineer the built-in electric field and the simulation of flattened conduction band. ISB absorption measurements in the far IR are presented.

Chapter 2

Introduction to III-nitride semiconductors and intersubband transitions

The simulation and fabrication of ISB devices require a deep understanding of both the material properties and the operating principles of ISB transitions. In the first section of this chapter I will present the crystalline structure and the band diagram of GaN, AlN and its alloys. I will continue with the explanation of the origin of the strong internal electric field in nitride heterostructures and its quantification. I will conclude by introducing the strain relaxation mechanisms in nitride heterostructures. The second section of this chapter will be devoted to ISB transitions, including their definition, selection rules and the shifts associated to many-body effects.

2.1 Properties of III-nitride semiconductors

2.1.1 Crystalline structure and polarity

GaN, AlN and its alloys can exist in the cubic zincblende (β) phase and in the hexagonal wurtzite (α) phase, the latter being thermodynamically favorable. This work is dedicated only to III-nitrides with hexagonal crystallographic configuration and the following overview of the material properties addresses only wurtzite-phase semiconductors.

The wurtzite crystal structure, presented in Fig. 2.1(a), belongs to the $P6_3mc$ space group in the Hermann-Mauguin notation. It consists of two hexagonal merged sublattices which are shifted along the [0001] direction by $u=3/8c$, where u is the anion-cation bond length along the <0001> axis and c is the height of the hexagonal prism (Fig. 2.1(b)). In the ideal wurtzite structure c is related to a, the base hexagon side, by

$$c = \sqrt{\frac{2}{3}}a, \tag{2.1}$$

However, the real structure presents a certain deviation from this equation, which depends on the nature of the metal cation.

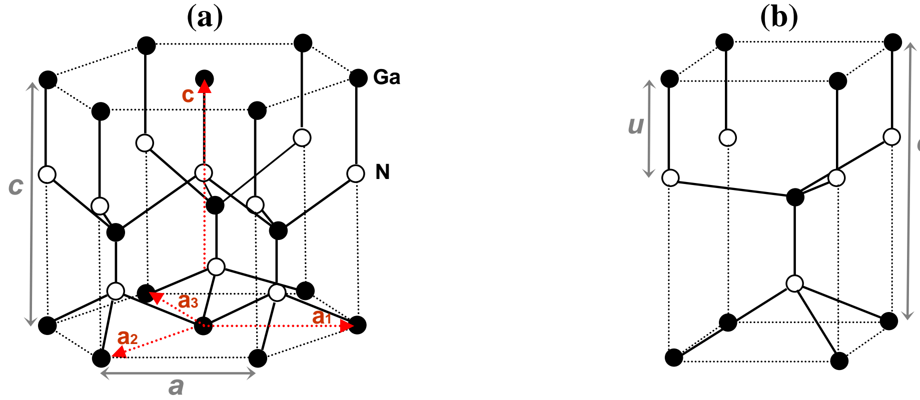

Figure 2.1. *(a) Wurzite structure of GaN and (b) hexagonal unit cell of GaN.*

The lattice parameters of GaN and AlN are presented in Table 2.1. Values for $Al_xGa_{1-x}N$ alloys vary linearly with composition and can be described by Vegard's law:

$$a(Al_xGa_{1-x}N) = x\, a(AlN) + (1 - x)\, a(GaN) \qquad [2.2]$$

Table 2.1. Lattice parameters of bulk GaN and AlN at room temperature.

Parameter	GaN	AlN
a, Å	3.189	3.112
c, Å	5.185	4.982
u, Å	0.377	0.382

The planes and directions in a hexagonal structure are conventionally described in terms of four Miller-Bravais indices, *hkil*, associated to the lattice vectors a_1, a_2, a_3 and *c* illustrated in Fig. 2.1(a). The base vectors are separated by angle of 120° and their vector sum is equal to zero. Therefore, the sum of the first three indices is necessarily zero: $i = -(h + k)$. In the hexagonal lattice, the directions defined by Miller-Bravais indices are not perpendicular to the corresponding planes.

In hexagonal prism, the planes that are perpendicular to the <0001> axis are called polar [{0001} *c*-plane in Fig. 2.2(a)], whereas the planes parallel to <0001> are referred as nonpolar [{1-100} *m*- and {11-20} *a*-planes in Fig. 2.2(a)], and the ones that make an angle different than 0° and 90° with <0001> are named semipolar [for example, (11-22) plane in Fig. 2.2(b)].

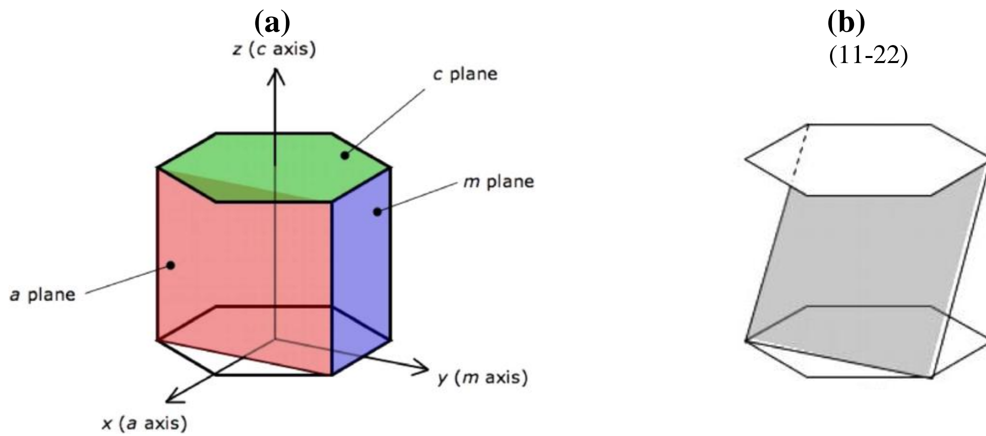

Figure 2.2. *Hexagonal unit cell with (a) common nomenclature of polar and non-polar planes and axis, and (b) semi-polar (11-22) plane (Masui, 2010).*

The wurzite structure is asymmetric in the [0001] and [000-1] directions. The axis sign is determined by the direction of the vector associated to the metal-nitrogen bond along the <0001> axis. The [0001] axis is considered positive when this vector points from the metal atom to the nitrogen atom (Fig. 2.3). We arbitrarily denote the material as metal-polar if grown along the [0001] or as nitrogen-polar if grown along [000-1].

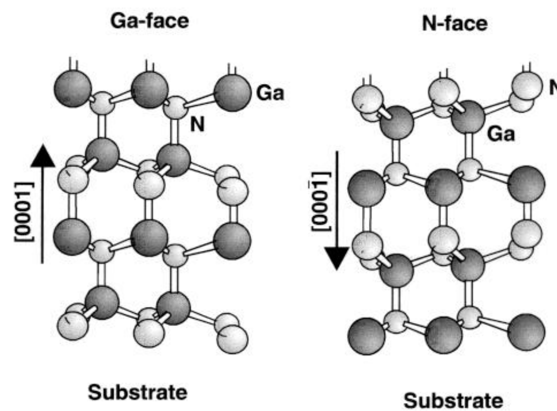

Figure 2.3. *Crystal structure of Ga- and N-polar wurtzite GaN (Ambacher, 1998).*

The polarity of the film can be controlled by the proper substrate choice and by growth conditions (Hellman, 1998; Keller, 2006). Crystal polarity affects bulk, surface (Sun, 1994), optical properties of the material (Kang, 2006) and growth features (Sun, 2008). Usually, Ga-face GaN is preferred as it is more chemically stable and it is easier to control its surface morphology during the growth.

2.1.2 Band structure of III-nitrides

The band structure of wurtzite GaN and AlN compounds was widely investigated by different approaches such as *ab initio* linearized plane wave method (Limtimein, 2002), time-resolved photoluminescence (TRPL) measurements and theoretical calculations based on the local density approximation (Chen, 1996; Suzuki, 1995), or muffin tin potential (Bourne, 1972). III-nitride semiconductors are materials with direct band gap; consequently for the optical properties the relevant k-space region located at k = 0 (Γ point on Fig. 2.4) and its vicinity.

(a) (b)

Figure 2.4. *Band structure of (a) GaN (Bloom, 1974) and (b) AlN (Kobayashi, 1983).*

As illustrated in Fig. 2.4, the lateral valleys for GaN and AlN are energetically far from band minimum, which is important for laser application in order to have negligible non-radiative electron scattering. The valence band of wurtzite III-nitrides is not degenerated in the Γ point, but it is split in three states – A (Γ_9), B (Γ_{7+}) and C (Γ_{7-}) - due to crystal field and spin-orbit coupling, as illustrated in Fig. 2.5.

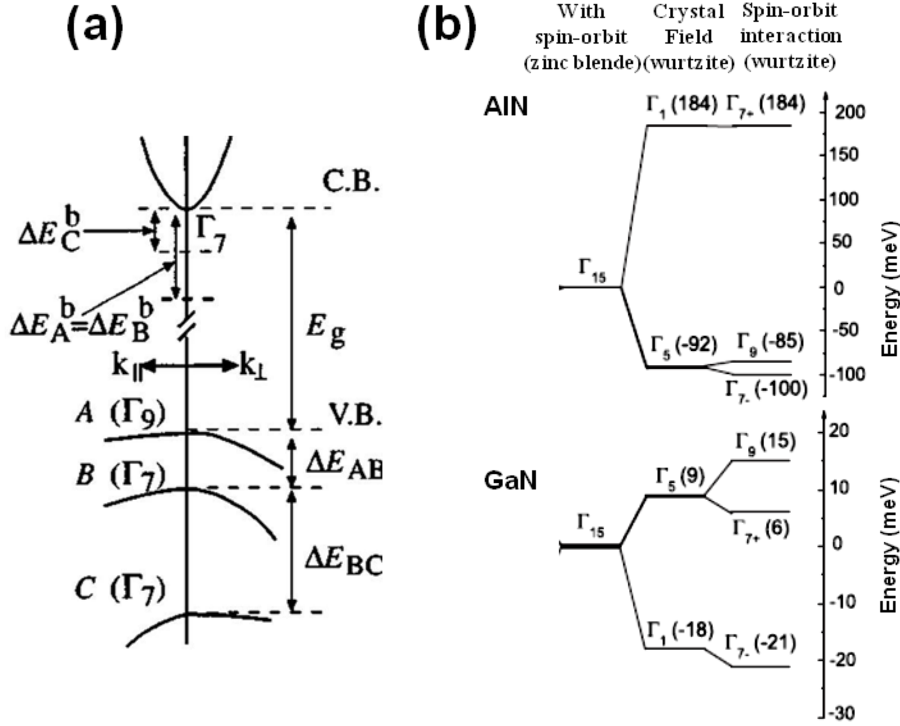

Figure 2.5. *(a) Conduction and valence band near Γ point of wurtzite III-nitrides (Jain, 1999). (b) Splitting and shifts due to the crystal-field splitting and spin-orbit interaction for AlN and GaN. The absolute energy value (in meV) is given in parenthesis. The threefold degenerate Γ_{15} level of the zincblende polymorphs is used as energy zero (Carvalho, 2010).*

Applying the **k•p** approach, these three levels can be obtained using a quasi-particle approximation:

$$\varepsilon(\Gamma_9) = \Delta_{cf} + \frac{1}{3}\Delta_{so_{II}} \qquad [2.3]$$

and

$$\varepsilon(\Gamma_{7+/-}) = \frac{1}{2}(\Delta_{cf} - \frac{1}{3}\Delta_{so_{II}}) \pm \frac{1}{2}\sqrt{(\Delta_{cf} - \frac{1}{3}\Delta_{so_{II}})^2 + \frac{8}{9}\Delta^2_{so_\perp}} \qquad [2.4]$$

where Δ_{cf} is the hexagonal crystal-field splitting, and $\Delta_{so_{II}}$ and $\Delta_{so_\perp}$ spin-orbit splitting components related to the orientation of the valence band states either parallel or perpendicular to the *c* axis (Chang, 1996). The energies of these three upper states in the valence band for AlN and GaN are illustrated in Fig. 2.5(b) and (c), respectively. The spin-orbit splitting is much smaller than the crystal-field splitting in III-nitrides.

In III-nitride materials, the electron effective mass is approximately isotropic, so that it can be considered as constant in all directions. In contrast, the hole effective mass is strongly anisotropic, which must be taken into account for band engineering of III-nitride heterostructures. Reported values of electron and hole effective masses are presented along with other band parameters in Table 2.2.

The difference in the electronic properties of two materials at the heterointerface is accommodated by the offsets in the conduction and valence bands. It is important to pay attention to this effects as for example, it has an influence on carrier behavior at the heterojunction which is used in high-power field-effect transistor (FET) devices and as well the offset found optical application in the ISB technology. Conduction and valence band discontinuities in III-nitride heterostructures are of type I which offers prospects to make this material active not only in ultraviolet but also in infrared spectral range. The large conduction band offset between GaN and AlN (about 1.75 eV) makes III-nitride an excellent material for near-IR ISB photonic device application.

Table 2.2. *Band parameters of bulk GaN and AlN at room temperature:* E_g *– band gap;* m_e* *and* m_h* *- effective masses of electrons and holes, respectively;* β *- Debye temperature;* α *- Varshni coefficient; b – bowing parameter;* ΔE_c *– conduction band offset.*

Parameter	**GaN**	**AlN**
E_g(T = 0K), eV	3.507 (Vurgaftman, 2001)	6.23 (Vurgaftmann, 2001)
m_e^*	0.20 m_o (Bougrov, 2001)	(0.32-0.40) m_o (Xu, 1993; Vurgaftman, 2001)
m_h^*	1.25 m_o (Santic, 2003)	1.44 m_o (Ramos, 2001)
β, K	0.590 – 0.909 (Li, 1997; Vurgaftman, 2003)	600 – 830 (Li, 1997; Vurgaftman, 2003)
α, meV.K^{-1}	1.799 (Guo, 1994)	1462 (Guo, 1994)
b, eV	1.00 (Yun, 2002)	
ΔE_c(GaN/AlN), eV	1.5 - 2.1 (Martin, 1996; Cociorva, 2002)	

In ternary compounds, the band gap dependence on the alloy composition is modeled using a quadratic polynomial whose nonlinear coefficient is called the bowing parameter, *b*. Therefore, in the case of AlGaN, the variation of the energy band gap with the Al concentration is given as

$$E_g(x) = (1-x)E_g(\text{GaN}) + xE_g(\text{AlN}) - b(1-x)x \quad [2.5]$$

The band gap of $AlxGa_{1-x}N$ is overestimated when calculated by the Vegard's law. Consequently, bowing parameter, *b*, accounts for the deviation from a linear interpolation.

The temperature dependence of the energy gap in GaN has been first evaluated experimentally by absorption (Teisseyr, 1994) and luminescence (Matsumoto, 1974), and can be estimated by the Varshni expression (Varshni, 1967)

$$Eg(T) = E(0) - \frac{\alpha T^2}{\beta + T} \qquad [2.6]$$

where *E*(*0*) is the energy gap at 0 K, and β and α are the Debye temperature and Varshni coefficients, respectively. The values of α and β are given in Table 2.2 for GaN and AlN.

2.1.3 Spontaneous and piezoelectric polarization

An intense polarization field is present in wurtzite GaN-based semiconductors along the <0001> axis due to the low symmetry of the crystal. The gravity centers of the positive and negative charges in the unit cell do not coincide, which creates a dipole along the <0001> direction. As this spontaneous polarization depends on the cation-nitrogen bond length, there is a difference in the magnitude of polarization for GaN and AlN. GaN has larger *u* and smaller *c*/*a* value in comparison with AlN, which results in smaller spontaneous polarization: -0.029 C/m^2 for GaN and -0.081 C/m^2 for AlN (Bernardini, 1997). The spontaneous polarization of $Al_xGa_{1-x}N$ nonlinearly depends on the composition of the alloy and can be calculated as (Bernardini, 2002):

$$P_{sp}(Al_xGa_{1-x}N) = xP_{sp}(AlN) + (1-x)P_{sp}(GaN) + bx(1-x) \qquad [2.7]$$

where P_{sp} is the spontaneous polarization of the bulk materials and *b* is the bowing parameter defined as (Bernardini, 2001):

$$b = 4P_{sp}(Al_{0.5}Ga_{0.5}N) - 2P_{sp}(AlN) - 2P_{sp}(GaN) \qquad [2.8]$$

As GaN/AlN is a lattice mismatched system, another important component of the polarization field is the piezoelectric polarization that appears as a response of the

material to the mechanical stress. The direction of *Ppz* vector depends on the strain state. For example, in case of tensile strain in polar heterostructures (AlGaN layer on GaN substrate) the piezoelectric vector points along [000-1] direction whereas in case of compressive strain (AlGaN layer on AlN substrate) it corresponds to the direction of [0001] axis.

The piezoelectric field can be defined as

$$Ppz = \vec{e} \bullet \varepsilon \qquad [2.9]$$

where $\vec{e}$ is the tensor of piezoelectric constants and ε is the strain field. Due to crystal symmetry there are only three independent piezoelectric constants e_{15}, e_{31} and e_{33}:

$$\mathrm{P_{PZ}} = \begin{pmatrix} 0 & 0 & 0 & 0 & e_{15} & 0 \\ 0 & 0 & 0 & e_{15} & 0 & 0 \\ e_{31} & e_{31} & e_{33} & 0 & 0 & 0 \end{pmatrix} \times \begin{pmatrix} \varepsilon_1 \\ \varepsilon_2 \\ \varepsilon_3 \\ \varepsilon_4 \\ \varepsilon_5 \\ \varepsilon_6 \end{pmatrix} \qquad [2.10]$$

The deformation along [0001] direction is $\varepsilon_z = (c - c_0) / c_0$ and deformation in the plane perpendicular to [0001] axis is $\varepsilon_x = \varepsilon_y = (a - a_0) / a_0$, where c_0 and a_0 are in-plane and out of plane lattice parameters of unstrained bulk material. Accordingly to Hooke's law the stress σ_{ij} is related to the strain ε

$$\sigma_{ij} = \sum_{kl} C_{ijkl} \varepsilon_{kl} \qquad [2.11]$$

where C_{ijkl} is the tensor of the elastic module. In the case of hexagonal crystal symmetry, this matrix contains six elastic modules, of which five are independent

$$C_{ij} = \begin{pmatrix} C_{11} & C_{12} & C_{13} & 0 & 0 & 0 \\ C_{12} & C_{11} & C_{13} & 0 & 0 & 0 \\ C_{13} & C_{13} & C_{33} & 0 & 0 & 0 \\ 0 & 0 & 0 & C_{44} & 0 & 0 \\ 0 & 0 & 0 & 0 & C_{44} & 0 \\ 0 & 0 & 0 & 0 & 0 & \frac{1}{2}(C_{11}-C_{12}) \end{pmatrix} \quad [2.12]$$

In the case of biaxial strain in a layer grown in a polar direction, i.e. there is no stress along *c* direction or shear stress and $\sigma_x = \sigma_y$, the strain-induced piezoelectric polarization along the [0001] direction can be expressed as

$$Ppz = 2\frac{a-a_0}{a_0}(e_{31} - e_{33}\frac{C_{13}}{C_{33}}) \quad [2.13]$$

and the in-plane and out-of-plane lattice constants are related as

$$\frac{c-c_0}{c_0} = -2\frac{C_{13}}{C_{33}}\frac{a-a_0}{a_0} \quad [2.14]$$

The piezoelectric component for the alloys can be computed by Vegard's interpolation

$$Ppz(Al_xGa_{1-x}N) = xPpz(GaN) + (1-x)Ppz(AlN) \quad [2.15]$$

Then for the strained wurtzite III-nitrides total electric field is represented as a sum of spontaneous and piezoelectric components. Therefore, understanding of the role of these fields is essential for the sample growth and devices design issues. When dealing with superlattices the electric field in the wells can be estimated from periodic boundary conditions as follows (Ng, 2001)

$$F_z^w = \frac{(Psp^b + Ppz^b - Psp^w - Psz^w)}{\varepsilon^w + \varepsilon^b(L^w / L^b)}$$

$$F_z^b = -\frac{L_w}{L_b}F_z^w \quad [2.16]$$

where superscripts b and w corresponds to the barrier and the well, L and ε are the layer thickness and dielectric constants.

2.2 Physics of intersubband transitions

ISB transitions were observed for the first time in 1982 in a transistor structure (Ando, 1982), but it is only one decade later that we find the first ISB device: the QW infrared photodetector (Levin, 1993). In 1994 Faist et al. (Faist, 1994) presented a major breakthrough in the ISB technology: an alternative to laser diode with a novel operating principle – the quantum cascade laser (QCL). This was the beginning of the tremendous development of the ISB technology, which has already resulted in commercially available devices operating in the mid- and far-IR.

2.2.1 Selection rules

To get a basic idea about ISB physics we consider a QW with two confined states in a single-particle approach. Any transition from a state i to a state f, interband or ISB, can be described with Fermi's golden rule:

$$W_{if} = \frac{2\pi}{\hbar} \left| \langle \psi_i | H' | \psi_f \rangle \right|^2 \delta(E_f - E_i - \hbar\omega) \qquad [2.17]$$

where H' is the interaction Hamiltonian, ψ and E are the wave functions and energy of confinement levels of the initial and final states, and $\hbar\omega$ is the radiation energy. As the radiation wavelength is much larger than the lattice periodicity in case of an interband transition, and than the QW width in case of an ISB transition, it is possible to apply dipole approximation:

$$H' = \frac{q^2 E_0^2}{4 m^{*2} \omega^2} \left(\vec{e} \cdot \vec{p} \right) \qquad [2.18]$$

where q denotes elementary charge, E_0 is the electric field amplitude, m^* is effective mass, and $\vec{e}$ and $\vec{p}$ are the polarization vector and momentum operator, respectively. Substituting Eq. 3.18 in Eq. 3.17 we obtain:

$$W_{if} = \frac{\pi}{\hbar} \frac{q^2 E_0^2}{2m^{*2}\, \omega^2} \left| \langle \psi_i | \vec{e} \cdot \vec{p} | \psi_f \rangle \right|^2 \delta(E_f - E_i - \hbar\omega) \quad [2.19]$$

The wave function of an electron ψ can be expressed as a product of a periodic Bloch function, *u*, and a slowly varying envelope function, *f*. Therefore, the matrix element $\langle \psi_i | \vec{e} \cdot \vec{p} | \psi_f \rangle$ splits into

$$\langle \psi_i | \vec{e} \cdot \vec{p} | \psi_f \rangle = \vec{e} \cdot \langle u_\nu | \vec{p} | u_{\nu'} \rangle \langle f_n | f_{n'} \rangle + \vec{e} \cdot \langle u_\nu | u_{\nu'} \rangle \langle f_n | \vec{p} | f_{n'} \rangle \quad [2.20]$$

where ν and ν' and n and n' are the band and subband indices of initial and final states, respectively. The first term describes selection rules for the interband transitions and it vanishes in the case of transitions within the same band. The second term is related to the ISB processes, and it consists of an overlap integral of Bloch functions, which is nonzero when considering the same subbands, and a dipole matrix element of the envelope functions that defines the selection polarization rule. If z is the growth direction then the free motion along x and y is given by

$$f_{nk}(r) = \frac{1}{\sqrt{A}} e^{ikr} \varphi_n(z) \quad [2.21]$$

where k is the wave vector and r is the position vector. Substituting Eq. 2.17 in to the dipole matrix element of the envelope functions and taking in to account that for $n \neq n'$ only term proportional to e_z does not vanish we obtain

$$\langle n | p_z | n' \rangle = \int dz \varphi_n^*(z) p_z \varphi_{n'}^*(z) \quad [2.22]$$

Thus, only the electric field with a component perpendicular to the semiconductor layers is involved into ISB transitions (polarization selection rule). Moreover, due to the inversion symmetry potential transitions only with opposite parity of envelope wave functions are allowed in symmetric QWs. This later rule can be overthrown by breaking the QW symmetry either by design or by an electric field. The polarization selection rule imposes a certain additional geometrical complexity to experiment performance and device realization. Structures respond only to TM-

polarized light, which imposes the use of surface gratings or waveguide configurations to couple the light into the active region.

2.2.3 Many-body effects

To observe ISB absorption, the ground state of the QW has to be populated with electrons. Therefore, doping is an essential parameter for device design, and the requirement of high doping levels brings into consideration the effect of electron-electron interactions. Extensive research efforts have been devoted to study ISB transitions in the presence of dense electron plasma (Kandaswamy, 2010; Shtrichman, 2001; Bloss, 1989). In heavily doped structures, a large deviation of the ISB energy from theoretical prediction is observed (Li, 2004).

In order to understand optical properties of the nitride structures for ISB application it is important to take into account the influence of many-body effects. Many-body phenomena can be classified in two groups: the effects on the energy levels (exchange interaction and direct Coulomb interaction) and the effect on the absorption frequency (depolarization shift and exciton shift).

a) Depolarization shift and exciton shift

The depolarization shift (also known as plasmon screening) and the exciton shift can modify the ISB transition energy from its nominal value E_{21} to

$$\breve{E}_{21} = E_{21}\sqrt{1+\alpha-\beta}, \qquad [2.23]$$

where α and β correspond to the depolarization and exciton shifts, respectively.

The external radiation excites the electron from the ground states to the higher level and at the same time interacts with electron plasma which results in modulation of the carrier density and increase of the transition energy (Shtrichman, 2001). It is a plasmon shift of the transition caused by the screening response of the electron gas. The contribution of this effect can be estimated as

$$\alpha(n) = 2T_{ee}n / E_{21} \qquad [2.24]$$

where n is the sheet carrier density and T_{ee} is the ISB Coulomb integral for laterally homogeneous systems:

$$T_{ee} = \frac{-e^2}{2\pi\varepsilon\varepsilon_0} \int dz \int dz' \psi_{n'}(z)\psi_n(z) \left| z - z' \right| \psi_{n'}(z')\psi_n(z') \qquad [2.25]$$

The β component is associated with exciton shift which is interaction between excited electron with the hole in the ground state

$$\beta(n) = -\frac{2n}{E_{21}} \int dz \int dz \, \psi_{n'}(z)^2 \psi_n(z)^2 \frac{\partial V_{xc}[n(z)]}{\partial n(z)} \qquad [2.26]$$

where V_{xc} is the exchange-correlation potential

$$V_{xc}(r_s) = -\frac{e^2 k_F(r_s)}{\pi}[1 + Bx \ln(1 + \frac{1}{x})] \qquad [2.27]$$

with $x = r_s/A$, $A = 21$, $B = 0.7734$ and $r_s = [3/4\pi a_0^3 n(z)]^{1/3}$, $a_0 = (\varepsilon / m)\, a_B$, and a_B is the Bohr radius (Bloss, 1989).

b) Exchange interaction and direct Coulomb interaction

The 2D gas contribution to the ISB energy can be described via Hartree-Fock approximation. The exchange (Fock) interaction is the result of electron-electron interaction in two dimensional gas. It accounts for the electron repulsion with parallel spins which are kept apart by the orthogonality of their wavefunctions resulting from Pauli principle. It mainly influences the ground highly populated state by lowering its energy, which results in total blue shift of ISB transition. The exchange interaction has negligible effect on the excited state when it can be considered to be unpopulated. However, at significant doping levels when electrons are present on the second subband it is important to account for the exchange interaction between subbands.

The exchange interaction energy of an electron at the ground state with the rest of the electrons can be estimated as

$$E_{exch} = -\frac{e^2}{2\varepsilon}\int_0^{k_F}\frac{d^2k'}{(2\pi^2)}\int dz\int dz'\frac{e^{-q|z-z'|}}{q}|\psi_1(z')|^2|\psi_1(z)|^2 \qquad [2.28]$$

where $q = |z\text{-}z'|$, $k_F = (2\pi n)^{1/2}$, and n is the sheet electron density in QW (Bandara, 1988). Taking into account only first two terms of Taylor series expansion of the exponential the Eq. 2.24 can be represented in a following way

$$E_{exch}(k) \approx \frac{-e^2 k_F}{4\pi\varepsilon}\left(\frac{2E(k/k_F)}{\pi} - 0.25(\frac{k_F}{k_l})\right) \qquad [2.29]$$

where $k_l = \pi/L$ with L being QW thickness and E is the complete elliptic integral.

Another important term is the direct Coulomb (Hartree) term which tends to screen electric field. The direct Coulomb interaction energy which is smaller than the exchange interaction term is given by

$$E_{dir} = \frac{3ne^2}{8\varepsilon k_l^2 L} \qquad [2.30]$$

where n is the $2D$ carrier density, e is the electron charge, ε – dielectric constant and L – QW's width.

Accounting above describes many-body effect the final transition energy can be estimated as

$$E_{21}^{final} = \breve{E}_{21} - E_{exch} - E_{dir} \qquad [2.31]$$

Chapter 3

Experimental techniques

This chapter will present the short description of the experimental techniques used in this work and their physical principles. I will start with the introduction of the plasma-assisted molecular beam epitaxy and the use of in situ characterization equipment such as Reflection High Energy Electron Diffraction. I will also describe growth conditions for GaN, AlN and its alloys. Then, a second section is devoted to characterization techniques, including optical characterization by Photoluminescence and Fourier Transform Infra-Red Spectroscopy, morphological characterization by Atomic Force Microscopy and structural characterization by X-Ray Diffraction.

3.1 Plasma-assisted molecular beam epitaxy

3.1.1 PAMBE equipment

Epitaxial growth is the process when a crystalline layer formed on a substrate by deposition of new material onto the surface keeping a certain lattice alignment. In the case of MBE the formation of the epilayer occurs under ultra high vacuum conditions due to the interaction of one or several molecules or atomic beams of the constituent on the substrate surface maintained at the certain elevated temperature. MBE has a number of advantages over other growth techniques:

- good control over layer thickness due to low growth rate;
- excellent interface and surface morphology;
- precise control of the beam fluxes;
- growth of complex heterostructures with many different layers;
- high purity starting materials;
- relatively low growth temperature.

An additional advantage is possibility to use *in situ* control by means of diagnostic methods like modulated beam mass spectrometry (MBMS) and Reflection High-Energy Electron Diffraction (RHEED).

The III-nitride heterostructures studied in this thesis were grown in a plasma-assisted MBE (PAMBE) equipment which is schematically depicted in Fig. 3.1. The main building blocks of this system are introduction chamber, transfer chamber and deposition chamber. In order to load the samples the introduction chamber is open under nitrogen flux and after that evacuated up to 10^{-9} mbar. The transfer chamber is an ultra-high transfer module permanently kept at the pressure of about 10^{-10} mbar. The growth chamber is evacuated to $\approx 10^{-11}$ mbar by a cryogenic pump and cryogenic cooling of the walls of the chamber with liquid nitrogen. The molecular beams of Al, Ga, In and Si are generated from high-purity metals in effusion cells. A mechanical shutter in front of every effusion cell is used to interrupt the beam flux in order to start or stop the doping and deposition. A molybdenum sample holder with an In glued substrate is fixed on an axis manipulator which provides facilities to automatically rotate and heat the substrate. The substrate rotation is needed in order to obtain homogeneity in the layer thickness and composition. The growth in this type of systems occurs under a nitrogen pressure of about 5×10^{-6} mbar.

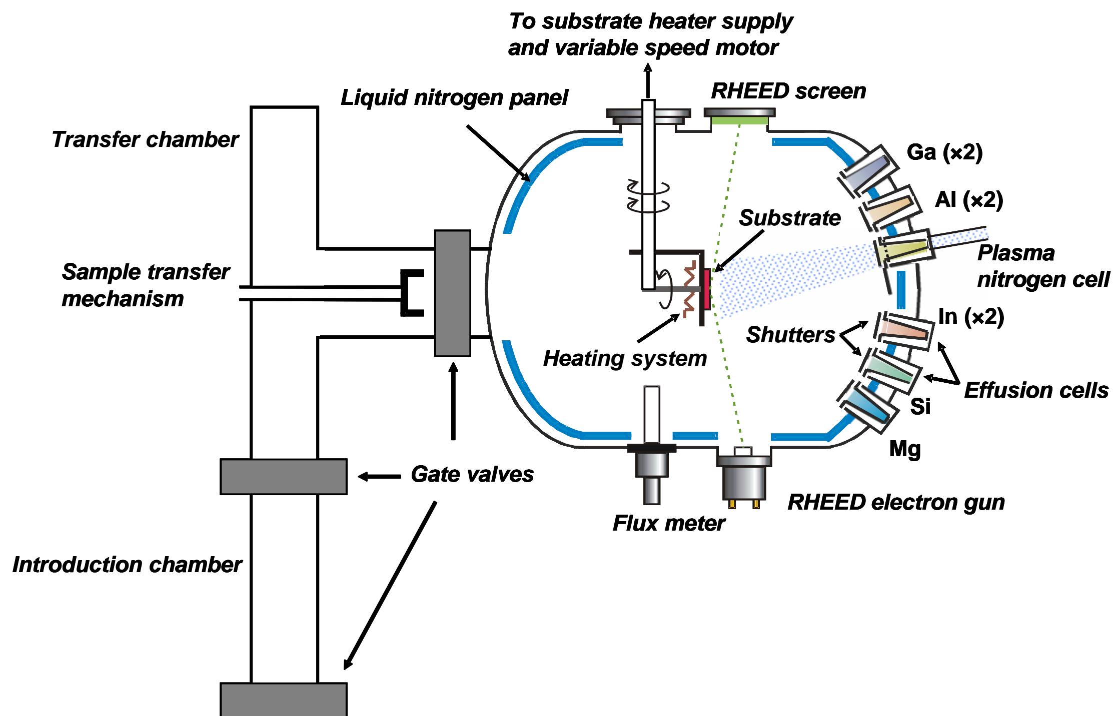

Figure 3.1. *Schematic of the plasma-assisted MBE used in this thesis.*

Since N_2 molecules are not reactive with Ga and cannot be thermally dissociated, they are cracked in a plasma cell in order to obtain mono-atomic nitrogen. Thus, the

above described MBE system is equipped with an automatic nitrogen plasma source HD25 supplied by Oxford Applied Research (Fig. 3.2). The N_2 molecules are excited and dissociated by a radio frequency waves.

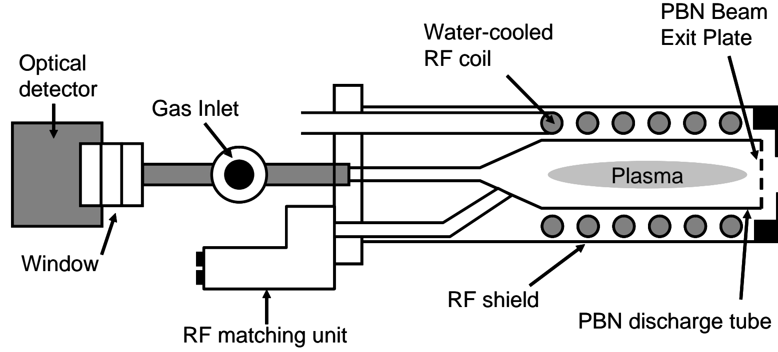

Figure 3.2. *Schematic of nitrogen plasma source HD25 from Oxford Applied Research.*

The ultra high vacuum (UHV) conditions enable to analyze and control *in situ* the growth process by RHEED, which provides information about surface structure of the substrate and growing epilayer. A high-energy beam accelerated by the voltage of 32 kV is directed towards the sample surface at a grazing angle. The electron beam penetrates only the uppermost atomic layers. Diffracted by the crystal surface, the electron beam impinges on a phosphor screen mounted opposite to the electron gun. Therefore the structure of the growing interface is represented in a reciprocal space (Fig. 3.3(a)). The radius of Ewald sphere is much larger than the separation of the rods and the intersection of the sphere and rods occurs some way along their length, resulting in a streaky, rather than spotty, diffraction pattern (Fig. 3.3(b)). The relationship between atom arrangements and diffraction pattern can be derived from Bragg equation

$$d = \frac{2\lambda L}{S} \qquad [3.1]$$

where d is the interplanar distance, L is the distance between the sample and the screen, S is the distance between elongated streaks. The calculated d corresponds to the diffraction along the <11-20> azimuth direction of wurtzite material. The RHEED pattern can provide information about growth kinetics, polarity of the material and 2D

or 3D nature of the growing surface, relaxation processes, etc (Smith, 1998; Foxon, 1999; Hughes, 1999; Grandjean, 1997).

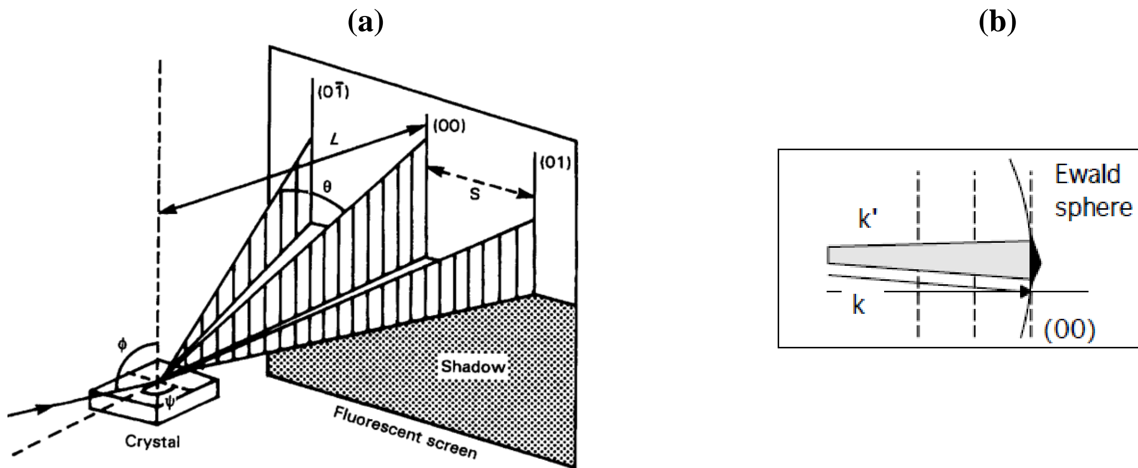

Figure 3.3. *(a) Schematic description of the RHEED measurements. (b) Ewald sphere construction (http://www.chemistry.msu.edu/).*

When growth proceeds layer by layer, the oscillatory variations in the RHEED intensity are directly related to the growth rate (Fig. 3.4). This RHEED feature has been used in order to calibrate the growth rate, control alloy composition and thickness of the layers. The damping of the oscillation intensity occurs when the growth proceeds and increase of the amplitude when the surface recovers. The oscillation period corresponds to the growth of the single layer.

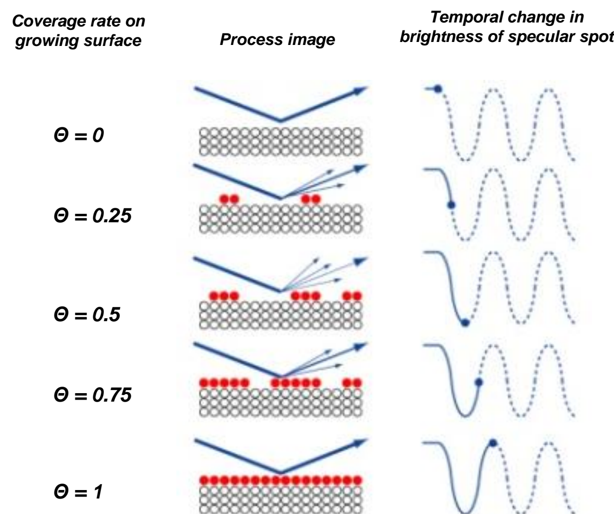

Figure 3.4. *RHEED oscillation during the epilayer deposition.*

3.2 PAMBE growth of III-Nitrides

3.2.1 Heteroepitaxial growth

There are several processes lying at the heart of the MBE growth (Madhukar, 1983):

- impingement of the molecular beams on the substrate;
- surface diffusion;
- incorporation of the atoms into the lattice of the material;
- thermal desorption or accumulation on the growing surface of the atoms not incorporated into the crystal lattice.

The processes occurring during MBE growth schematically illustrated in Fig. 3.5. The main parameters that define the kinetics of the growth are the impinging flux of the species, and their sticking diffusion and desorption coefficients at the growth temperature.

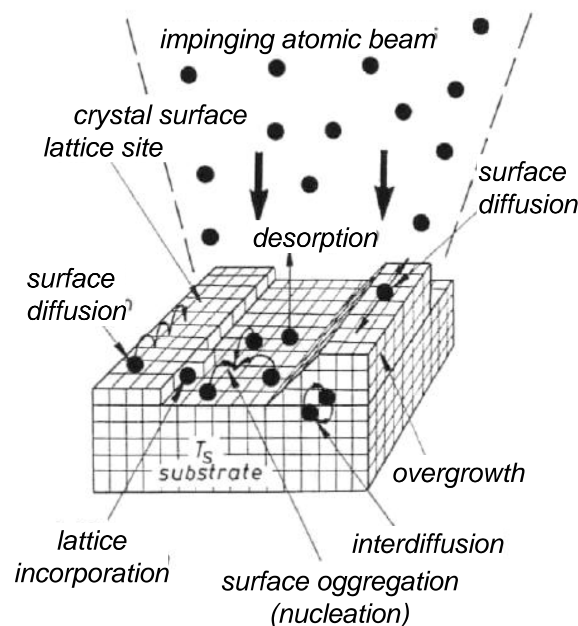

Figure 3.5. *Schematic illustration of the main surface processes during MBE growth (Hermann, 1986).*

If both the growing layer and the substrate are of the same material the process called homoepitaxy; if the materials are different it is known as heteroepitaxy. In the

case of GaN, due to the lack of native crystals with a reasonable quality and price, growth is generally made by heteroepitaxy on lattice mismatched substrates such as silicon, sapphire or SiC. Furthermore, the significant lattice mismatch between binary compounds (2.5% GaN/AlN and 11% GaN/InN) leads us to consider the various possibilities of growth modes. In heteroepitaxial growth there are three possible modes can be identified (Fig. 3.6):

- Frank Van der Merwe mode (layer-by-layer growth) is two-dimensional growth process when a new layer is nucleated after completion of the layer below. The misfit strain during the growth can be released by formation of dislocations (Frank, 1949).
- Volmer-Weber growth mode (3D growth mode) consists in first phase of large number of surface nuclei of deposited material that forms droplets and clusters on the surface. Thus VW growth often results in a high mosaicity of the material inside the layer (Volmer, 1926).
- Stranski-Krastanow mode is an intermediate between FV and VW growth modes. The first deposited layer is atomically smooth and compressively strained up to a certain critical thickness when the elastic energy reaches its maximum value. At this point the phase transition from 2D to 3D growth takes place (Stranski, 1938).

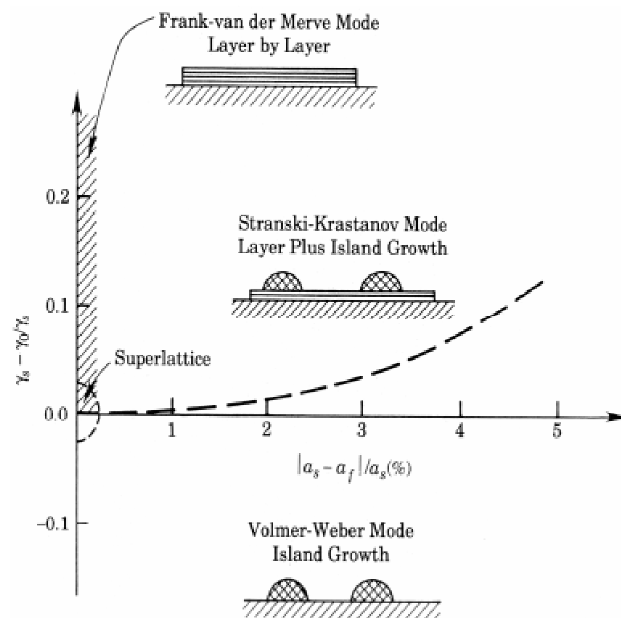

Figure 3.6. *Energy ratio (Substrate to film) versus lattice mistmatch, showing three main grwth modes (Tu, 1992).*

The three major growth modes are shown in the Fig. 3.6. in a plot of relative energy potential W of the substrate to the film versus the lattice mismatch. Under the proper conditions, layer-by-layer growth can be achieved when the lattice mismatch is negligible. If the film has a high surface energy per unit area compared to the substrate, clusters form in the Volmer-Weber mode. The intermediate mode is Stranski-Krastanov mode, when there is a few monolayers thick wetting layer is formed before the clusters start to appear.

3.2.2 Strain relaxation in GaN/Al(Ga)N heterostructures

The strain in heterostructures can be released elastically by undulation of the surface, or plastically by introducing defects in the epilayers. These extended defects can affect the device properties causing nonradiative recombination, carrier scattering, and enhanced diffusion of dopants and impurities. There are several types of plastic relaxation: crack propagation – commonly observed in III-nitrides under tensile stress-, decohesion of the layer, introduction of misfit dislocations (MDs) or glide of pre-existing threading dislocations (TDs). There are three types of TDs can be found in wurtzite III-N films: edge-, screw- and mixed-types. Edge dislocations make up the majority of the TD density in III-nitrides. The line direction of these dislocations lies along the [0001] axis and the Burger vector is one of the basal vectors 1/3[2-1-10], 1/3[-12-10] or 1/3[-1-120], see Fig. 2.6(b). Screw type dislocations have line direction and Burger vector both lie along the [0001], Fig. 2.6(c), and mixed type dislocations have Burger vector equal to a sum of *a* and *c* lattice translation vectors, Fig.2.6(c).

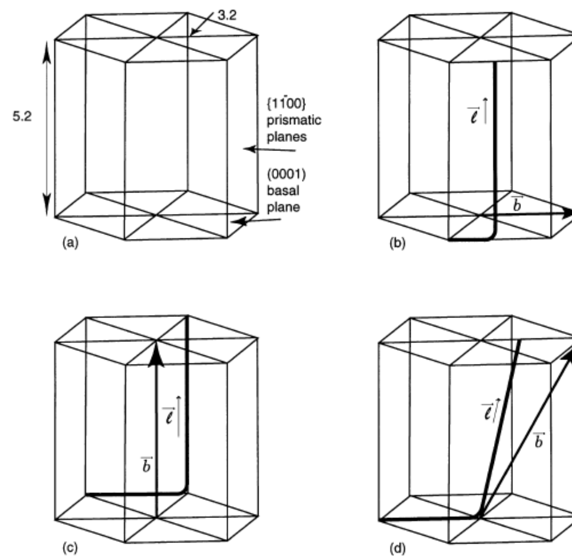

Figure 2.6. *(a) Unit cell of wurtzite GaN. (b) Edge-type dislocation. (c) Screw-type dislocations. (d) Mixed-type dislocations (Mathis, 2001).*

In the case of nitride heterostructures grown along the [0001] axis, which is the predominant growth orientation in commercial devices, the formation of regular networks of MDs is hindered since the most crystallographically favorable slip system, the (0001) basal plane with <11-20>{0002} slip directions, lies parallel to the heterointerfaces (Ponce, 1997). However, MDs can be detected at heterointerfaces when shear stress is intentionally or unintentionally induced by three dimensional growth (Moran, 2004; Kehagias, 2005), by crack formation (Hearne, 2000; Floro, 2004), or in close proximity to V-defects (Liu, 2006). Therefore, the relaxation mechanism depends not only on the structure itself, but also on the growth conditions.

During the last two decades, it was shown that the heteroepitaxy of III-nitrides exhibits numerous extended defects such as TDs (Wu, 1996; Ponce 1997; Ning, 1996), stacking faults (SFs) (Stampfl, 1998; Northrup, 1998; Potin, 2000; Vermaut, 1999) and inversion domains (Northrup, 1996; Potin, 1999). The main defects are TDs and SFs. The corresponding dislocations are perfect or partial, their Burgers vectors **b** are shown in Table 3.1. A basal stacking fault (BSF) is a mistake in the normal ABABABA… hexagonal stacking sequence along the [0001] direction. They are known as intrinsic (I1 and I2) and extrinsic (E). Their stacking sequence (SS) and displacement vector (**R**) are given in Table 3.1. For prismatic stacking faults (PSFs) the displacement **R** takes place out of the basal plane (Drum, 1965; Blank, 1964). In

GaN and AlN, two displacement vectors have been reported to characterize the PSFs in $\{11\bar{2}0\}$ planes (Northrup, 1998; Vermaut, 1999). Inside nitride layers grown along the **c**-axis, SFs are limited close to the interface with the substrate (Northrup, 1996).

Table 3.1. *Dislocations and stacking faults in hexagonal structure. P: prismatic, B: basal and SS: stacking sequence.*

Dislocations $\vec{b}$	Type	Character
$1/3<11\bar{2}0>$	a	Perfect
$1/3<11\bar{2}3>$	a+c	Perfect
$<0001>$	c	Perfect
$1/3<1\bar{1}00>$		Shockley partial
$1/6<20\bar{2}3>$		Frank-Shockley partial
$1/2<0001>$		Frank partial
Stacking Faults $\vec{R}$	**Type**	**SS or plane**
$1/3<1\bar{1}00>$	B-I_1	AB<u>ABC</u>BCB
$1/6<20\bar{2}3>$	B-I_2	AB<u>ABCA</u>CA
$1/2<0001>$	B-E	AB<u>ABCAB</u>AB
$1/2<1\bar{1}01>$	P	$\{11\bar{2}0\}$
$1/6<20\bar{2}3>$	P	$\{11\bar{2}0\}$

3.2.3 Growth of GaN

The growth of GaN(0001) by PAMBE is extensively discussed in the literature (Adelmann, 2003; Mula 2001; Neugebauer, 2003). GaN growth can be described by precursor-mediated models (Lieberman, 1994). The schematic illustration of the process occurring during GaN layer growth is presented in Fig. 3.7. Atomic nitrogen and Ga atoms arrive and adsorb onto the growing surface where they can be moved to a chemisobed state. However, from chemisorbed state Ga adatoms can be transferred to a physisorbed state and thermally desorbed from the surface. When chemisorbed Ga meets an N atom the forward reaction is occurring forming GaN layer.

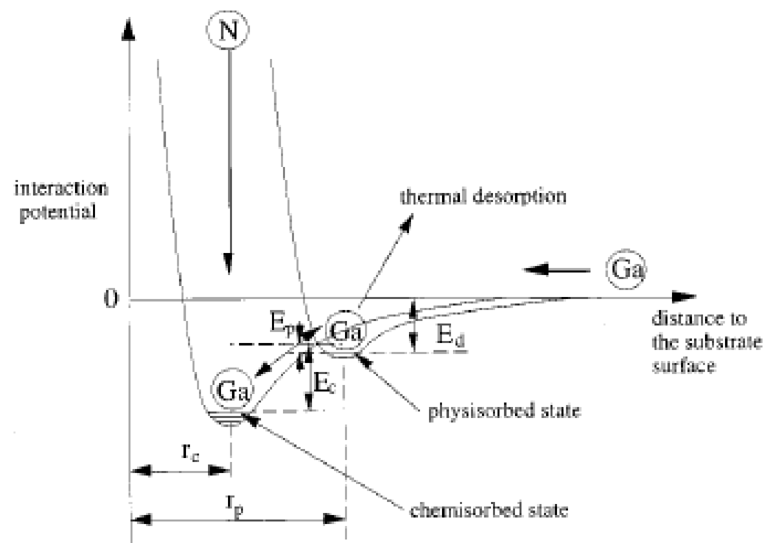

Figure 3.7. *Schematic illustration of the GaN growth kinetics (Myoung, 1999).*

The growth kinetics is determined by the control of the metal-to-nitrogen (III/V) flux ratio and substrate temperature. GaN deposition under N-rich conditions proceeds in a layer-by-layer mode that starts with RHEED oscillations that attenuate as the surface roughness increases (see Fig. 3.8). After a few nanometers, the RHEED becomes spotty and the samples are facetted with a high surface roughness. Deposition of 2D GaN layers requires Ga-rich conditions. However, high Ga flux forms metal droplets on the surface, which is detrimental to layer quality. In order to obtain GaN layers with smooth surface morphology, it is needed to perform the deposition under slight metal-rich conditions, at growth temperatures that allow a certain Ga desorption rate. In these conditions, it is possible to stabilize a Ga adlayer at the growing surface with a thickness independent of the Ga flux (Heying, 2000; Mula, 2001). This Ga excess forms a laterally-contracted biatomic Ga layer (Fig. 3.9) which minimizes the (0001) surface energy and postpones plastic and elastic relaxation (Neugebauer, 2003; Bellet-Amalric, 2004).

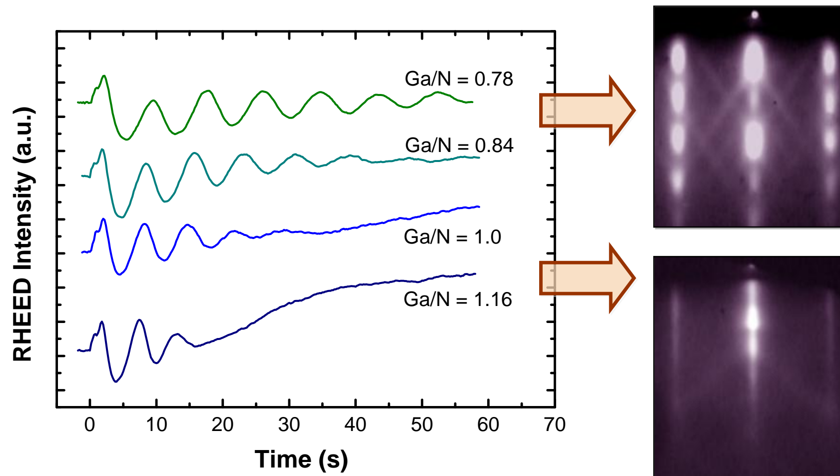

Figure 3.8. *RHEED intensity oscillations and pattern at different III/V ratios.*

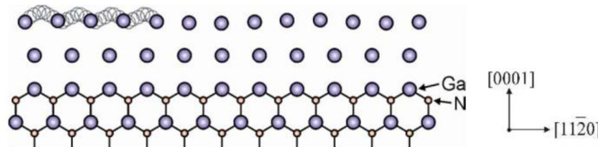

Figure 3.9. *Schematic view of the laterally-contracted Ga bilayer model (Northrup, 2000).*

Adelmann *et al.* observed a correlation between Ga Flux and Ga coverage of the surface at certain constant substrate temperature (Adelmann, 2003). It is possible to analyze quantitatively amount of Ga on an epilayer by means of the RHEED. The GaN surface was exposed for a short time to different Ga fluxes and in each case the RHEED intensity was studied during Ga evaporation process (Fig. 3.10). Four regimes can be distinguished.

A- There is a small quantity of Ga is present on the GaN surface for $\Phi <$ 0.3 ML/s.

B- Less than 1 ML of Ga at the growth front is reamined (0.3 ML/s $< \Phi <$ 0.5 ML/s).

C- Bilayer of Ga in the growth front ~ 2.4 MLs is formed for flux between 0.5 ML/s and 1 ML/s.

D- The system reaches the Ga accumulation regime, forming metal droplets for flux > 1 ML/s.

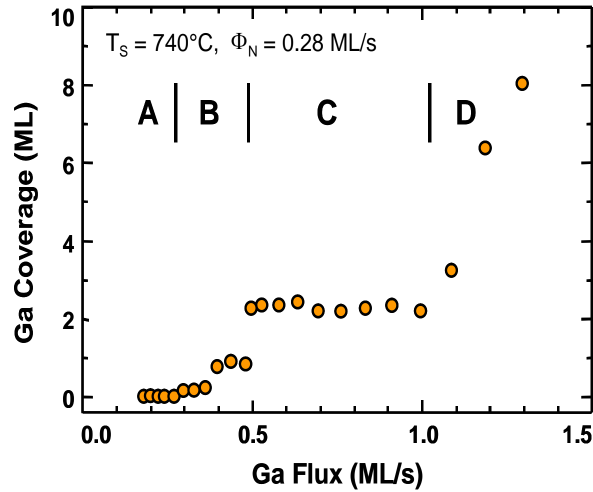

Figure 3.10. *Ga coverage on top of the GaN(0001) surface as a function of the Ga flux.*

Fig. 3.11 shows Ga flux dependence on the substrate temperature. In order to keep a certain Ga amount on the growing surface at higher temperature the higher Ga flux should be supplied. It was observed that smooth GaN with atomic steps can be obtained during Ga-rich growth in the Ga bilayer regime

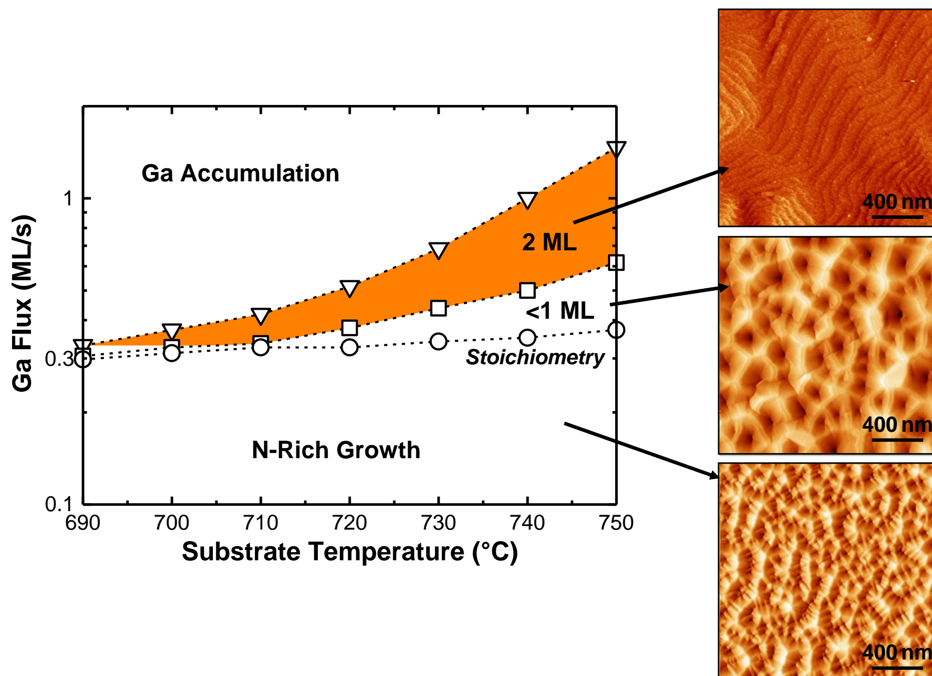

Figure 3.11. *Ga coverage regimes as a function of both substrate temperature and impinging Ga flux.*

3.2.4 Growth of AlN

The 2D growth of smooth AlN layers also requires metal rich conditions. In case of Al excess on top of epilayer RHEED pattern has two extra lines along <11-20> azimuth (Fig. 3.12) which corresponds to Al layer with smaller in plane lattice constant in comparison with AlN. However, Al cannot be desorbed at the standard GaN growth temperatures, around 700°C. Thus, in order to eliminate accumulated Al the growth interruption under N is needed.

Smooth AlN can also be deposited under stoichiometric growth conditions with excess of Ga on the growing interface in order to minimize the surface energy. The Ga – N bond is weaker that Al – N, and therefore Al is preferentially incorporated.

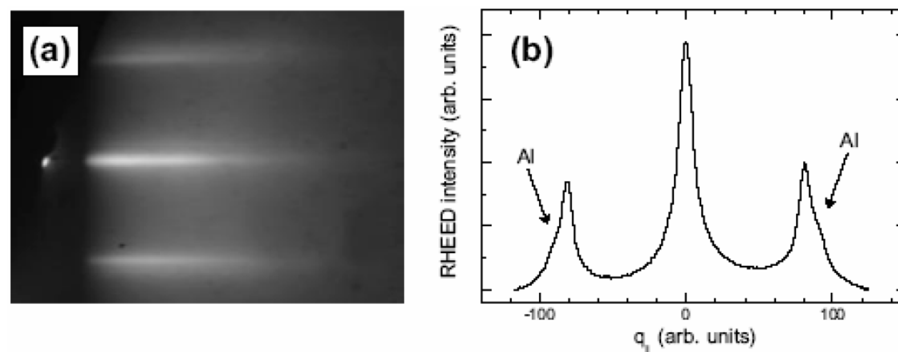

Figure 3.12. *(a) RHEED image of an Al-rich AlN surface (azimuth <11-20>). (b) Intensity profile along the <11-20> direction. The extra streaks due to the Al excess are indicated by the arrows.*

3.2.5 Growth of AlGaN

The two-dimensional (2D) growth of AlGaN layers also requires metal-rich conditions (Iliopoulos, 2002; Monroy, 2003). For relatively low Al content (< 50%), it is possible to obtain a layer-by layer growth mode under slightly Ga-rich conditions. As the sticking coefficient of Al is unity, we fixed the Al/N ratio at the required Al content and Ga is used in excess, to obtain a surfactant effect that favors 2D growth.

For Al contents above 40%, it is necessary to decrease T_S to maintain 2D growth, and In can be used as a surfactant to stabilize the surface (Monroy, 2003). Decreasing T_s promotes a balance of diffusion barrier between Al, Ga and N, and enhances the

sticking coefficient of In to the surface, which allows modification of surface free energy and kinetics.

3.3 Characterization techniques

3.3.1 X-Ray Diffraction

The structural quality and composition identification of the epitaxial layers were performed by means of a Seiftert XRD 3003 PTS system (Photographed on Fig. 3.13). The x-ray beam coming out from a source is reflected and converted into a parallel beam by the parabolic mirror. A beam of parallel (0.01° divergent) and monochromatic x-rays of wavelength λ = 0.154056 nm (Cu $k_{\alpha 1}$) is incident on a crystal at the angle ω, which is angle between the sample plane and the incident beam. Since the crystal has a periodic structure we can apply the Bragg's law

$$2d \sin \omega = n\lambda \qquad [3.2]$$

where n is the integer and d is the interplane spacing.

A highly parallel and monochromatic incident x-ray beam is achieved by using two monochromators each consisting of two Ge(220) monocrystals. So-called '4-crystal' scheme (-n, +n, +n, -n) results in a x-ray beam with a wavelength spread $\Delta\lambda / \lambda = 2.2\times10^{-5}$ and $\Delta\Theta = 0.0033°$. In order to chose a proper plane family the sample position is precisely controlled with a goniometer with four possible angular rotation mechanisms.

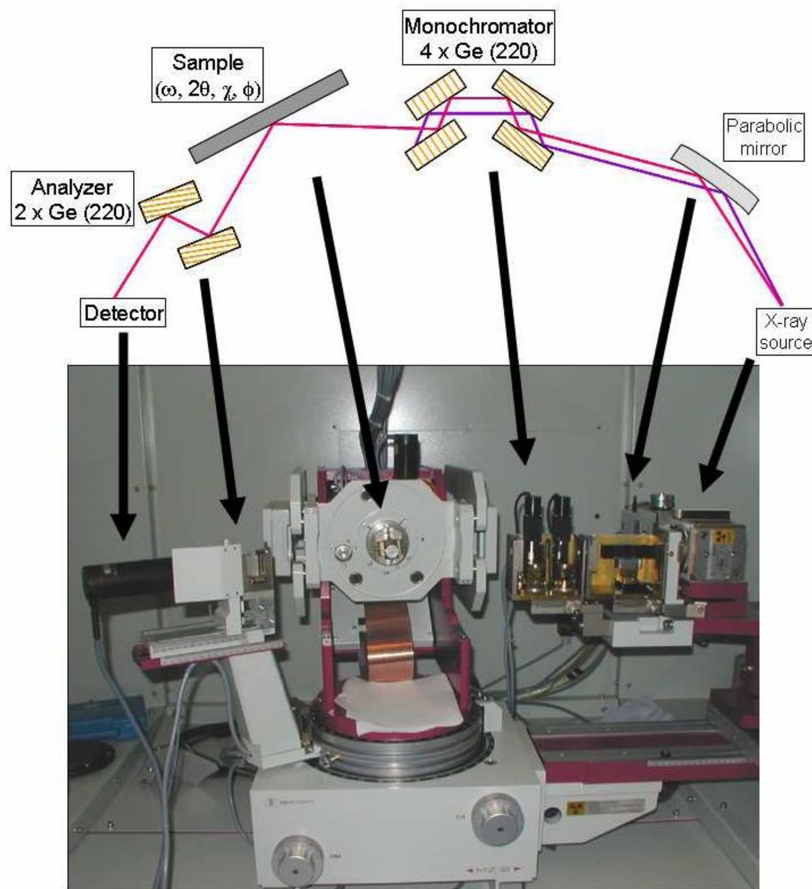

Figure 3.13. *Illustration of the X-ray diffraction system.*

The detector aperture is 2° which can be reduced by inserting slides in order to enhance the resolution. For high-resolution (HR) XRD measurements, an analyzer is placed between the sample and the diffracted beam. It consists of two Ge(220) monocrystals which improve the angular precision of the diffracted beam (≤ 0.001°). In this configuration, the direct beam intensity is higher than 10^6 counts per seconds (cps) and the noise is less than 1 cps.

The average c lattice parameters of the superlattices, $<c_{SL}>$, and of the AlGaN buffer layers, c_{AlGaN}, can be extracted from θ-2θ scans (Table 4.2) using Bragg's equitation:

$$\lambda = 2d_{hkl}\sin\theta \qquad [3.3]$$

and the superlattice period $T = t_w + t_b$ can be obtained from angular separation of two SL satellites in the θ-2θ scan.

$$T = \frac{\pm n\lambda}{2(\sin\theta_{\pm n} - \sin\theta_0)} \qquad [3.4]$$

where λ is the wavelength of the incident wave, d is the interplane distance, Θ is the angle between incident beam and scattering planes, Θ_0 and $\Theta_{\pm m}$ are the zero order and $\pm m$ order superlattice satellites.

3.3.2 Atomic Force Microscopy

The surface topology of the grown samples was studied by means of atomic-force microscopy (AFM) in the tapping mode. The schematic of the AFM is illustrated in Fig. 3.14.

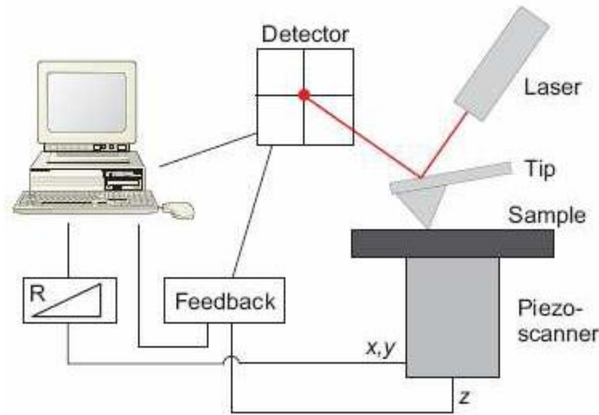

Figure 3.14. *Schematic of an AFM setup.*

The probe tip is integrated into a cantilever that is sensitive to the forces between the sample surface and the tip. In the tapping mode, the cantilever is oscillated at its resonant frequency

$$\omega_0 = \sqrt{\frac{k}{m}} \qquad [3.5]$$

The probe lightly "taps" on the sample surface during scanning, contacting the surface at the bottom of its swing. In this mode the gradient of the force effect on the resonant frequency

$$\omega = \omega_0\sqrt{1 - \frac{1}{k}\frac{\partial F}{\partial z}} \qquad [3.6]$$

When the tip approaches the surface the oscillation amplitude decrease rapidly. By maintaining constant oscillation amplitude a constant tip-sample interaction is maintained and an image of the surface morphology is obtained.

The minimum force that can be detected is defined as

$$(\frac{\partial F}{\partial z})_{\min} = \frac{1}{A}\sqrt{\frac{4Bkk_B T}{\omega_0 Q}} \qquad [3.7]$$

where A is the rms oscillation amplitude, B the detection bandwidth, $Q = \Delta\omega / \omega$ the quality factor of the resonance. According to Eq. (3.7) there are several parameters to adjust in order to increase the image quality:

- the force constant k should be small and the resonant frequency ω_0 should be high;
- high quality factor;
- low temperature.

3.3.3 Photoluminescence

Photoluminescence (PL) spectroscopy is a nondestructive method of probing the ground electronic states in the semiconductor structure. The mechanism of PL implies excitation of the material by a laser with energy exceeding the semiconductor band gap. The absorption of light in the sample results in a transfer of electrons from the valence to the conduction band. The return to equilibrium occurs via non-radiative processes (phonon emission) or radiative processes (photon emission). The absorption and carrier relaxation mechanisms have to agree with the energy and momentum conservation rules. As III-nitride materials have direct band gap both the photon absorption and emission conserve the momentum i.e. phonons are not required to assist the process. Besides energy band gap, PL spectroscopy provides information about electron and hole confined states in QW, donor or acceptor levels in the band gap due to presence of impurities or defects in the material or alloy inhomogeneities, for instance. From the broadening of the PL peak we can get information on the crystal quality.

Figure 3.15 illustrates the PL setup used in this work. The excitation of III-nitride structures was performed by frequency-doubled continuous-wave Ar^+ laser with λ = 488 / 2 = 244 nm. The signal was collected into a 45-cm-focal-length Jobin-Yvon monochromator and detected by an ultraviolet-enhanced charge-couple device (CCD).

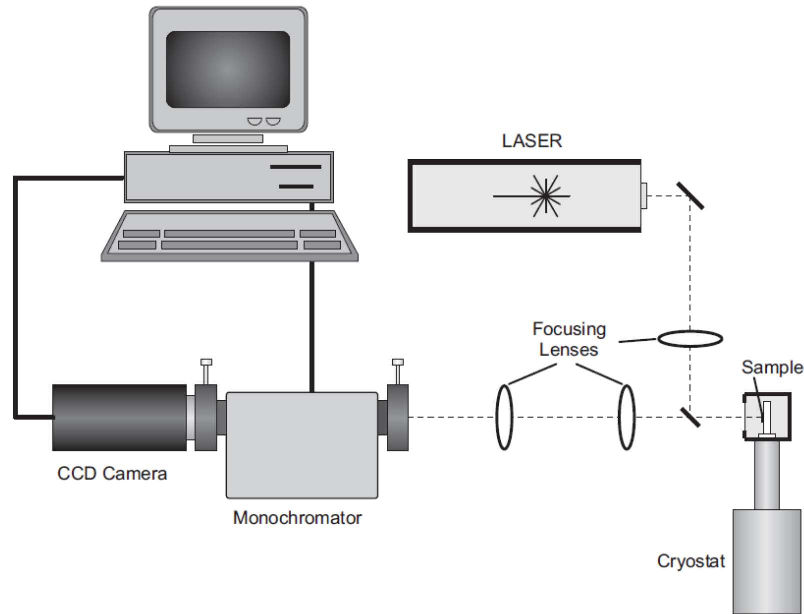

Figure 3.15. *Photoluminescence setup.*

Time-resolved photoluminescence (TRPL) has been used in order to study carrier relaxation processes. The principle is the excitation of the material by a laser pulse and study of the intensity evolution of the emission. The excitation source was a pulsed frequency-tripled Ti-sapphire laser with λ = 270 nm. In this TRPL setup, the monochromator had a focal length of 32 cm. In both PL and TRPL experiments the samples were mounted in a cold finger He cryostat and the diameter of the laser spot was about 50 μm.

3.3.4 Fourier Transform Infra-Red Spectroscopy

Fourier Transform Infra-Red (FTIR) spectroscopy uses infrared light in order to observe absorption, emission or photoconductive properties in semiconductor heterostructures. In this work in order to measure absorption spectra of the III-nitride heterostructures and identify ISB transitions Fourier Transform infra-red (FTIR) spectrometer Vertex 70v from Bruker was used. The schematic of the Vertex 70v is

illustrated in Fig. 3.16. It equipped with interferometer, sources, beamsplitters and detectors to cover whole IR spectral range. The sample compartment can be open while keeping source and detector compartment under vacuum.

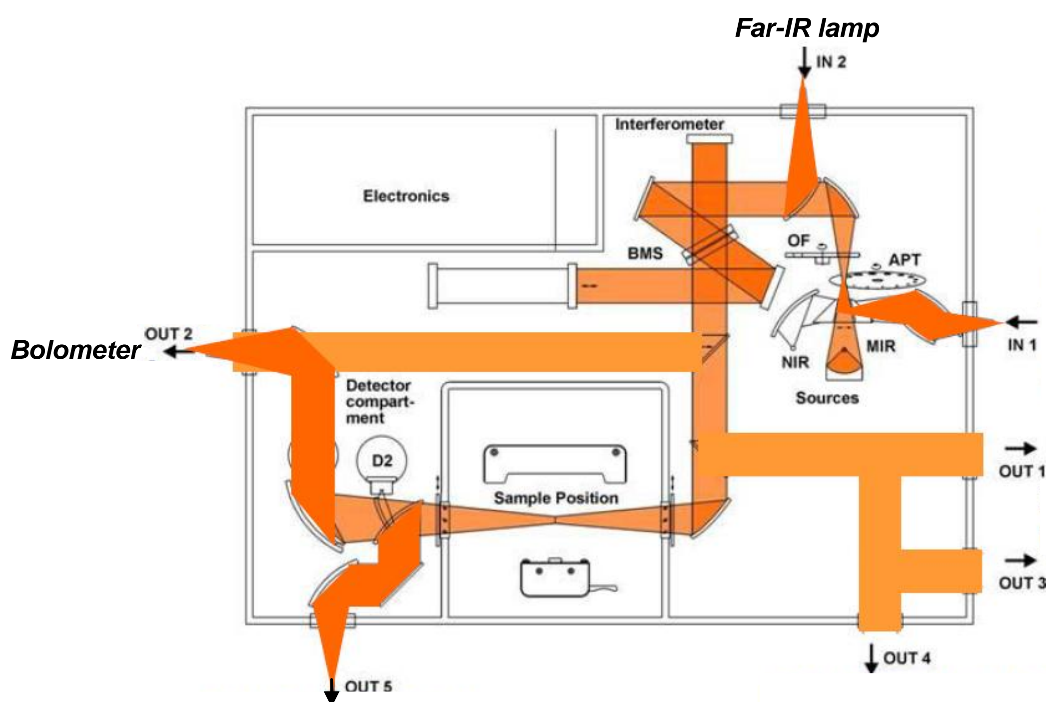

Figure 3.16. *Schematic configuration of Vertex 70v and optical path in the spectrometer.*

The working principle of the FTIR spectrometer is based on the using Michelson Interferometer (Fig. 3.17(a)). The interferometer consists of a beam splitter, a fixed mirror and a moving mirror. Ideally, the beam splitter is made of a special material that transmits half of the radiation striking it and reflects the other half. Therefore beam splitter separates IR light from a source into two optical beams: one is transmitted through and reflects off of a flat fixed mirror, and the other one reflects off of the beam splitter to the mirror with constantly moving mechanism. The beams reflected from the mirrors are recombined at the beam splitter. As the moving mirror travels back and forth, various wavelengths of light go in and out of phase. By recording the signal observed by the detector at precise intervals, the raw data for the interferogram is generated (Fig. 3.17(b)). The main peak corresponds to the interference of two beams with zero optical path difference. The reduction of the separation of the fringes when the path difference is large makes them more difficult to see. Then the interferogram is translated into absorption spectrum using Fast Fourier Transform algorithm.

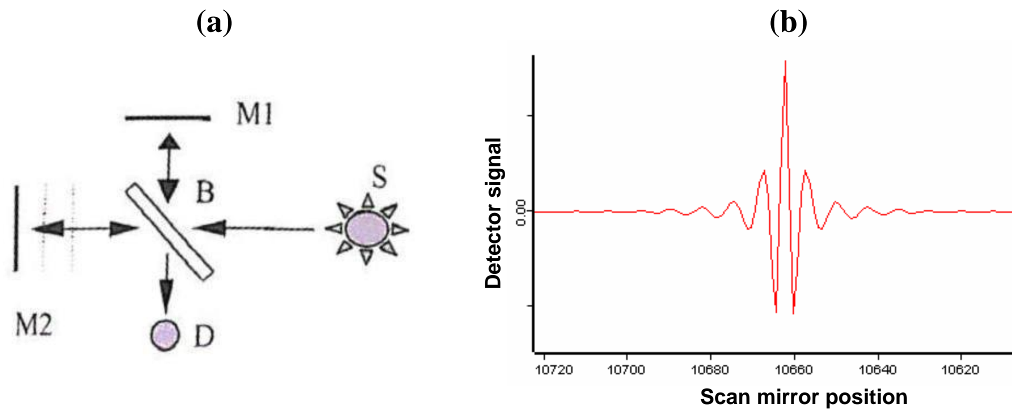

Figure 3.17. *(a)Schematic of interferometer: S – source, B – beam splitter, M1 – fixed mirror, M2 – moving mirror, D - detector . (b) Interferometer interferogram obtained by the detector.*

The particularity of Vertex 70v is that its interferometer has a 'rocksolid' permanent alignment. It incorporates dual retroreflecting cube corner mirrors in pendulum arrangement. Unlike flat mirrors, cube corner are practically immune to mirror tilt. This is an important consideration since the light returning to the beam splitter must be precisely recombined or reduction in the stability, resolution, and spectral quality will occur. The high throughput design insures the highest possible signal-to-noise ratio.

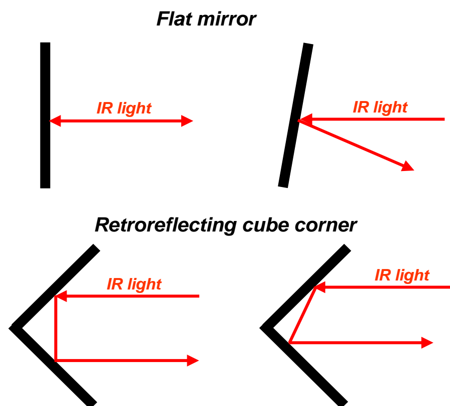

Figure 3.18. *Comparison of the effect of mirror tilt on a flat mirror vs retroreflecting cube corner.*

Vertex 70v is vacuum technique that eliminates detrimental atmospheric effects. Humidity of the air, CO_2 and other components of the air inside the spectrometer cause unwanted absorption that results in a numerous absorption lines in the measured

spectra (Fig. 3.19). Evacuating of the spectrometer is not necessary for the near-IR experiments however vacuum is preferred for the mid- and far-IR measurements.

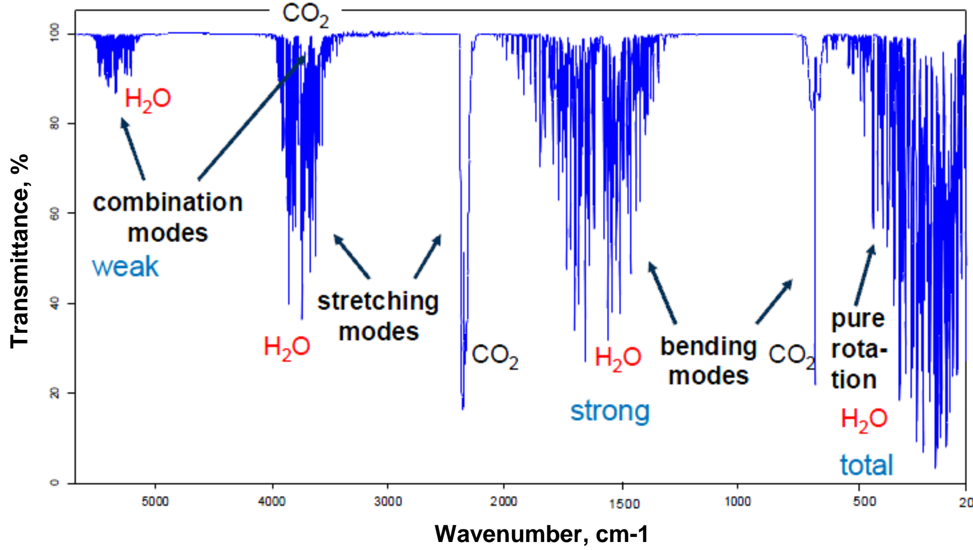

Figure 3.19. *Air vapor IR spectrum.*

Vertex 70v is equipped with a HeNe laser that emits red light with wavelength of 633 nm. The laser controls the position of the moving interferometer mirror and also is used in order a proper positioning of the sample. The main spectrometer's accessories used for different spectral ranges are presented in Table 3.1.

Table 3.1. *Accessories of the Vertex 70v for different IR spectral ranges.*

	Near-IR	**Mid-IR**	**Far-IR**
Source	Tungsten	Globar	Hg-Arc
Beam splitter	CaF_2	KBr	Si
Detector	InGaAs	MCT	Bolometer

3.4 Substrates

In order to achieve a good quality structures the homoepitaxial growth of III-nitrides should be performed on bulk material. However, epitaxial thin films are generally grown on foreign substrates as no source of bulk GaN for substrate manufacturing exists. The lack of a GaN substrate necessitates heteroepitaxy on compatible materials, commonly sapphire, SiC or Si(111). GaN manufacturing technology mainly uses sapphire for optoelectronic application and SiC or Si for

fabrication of high power devices. When choosing a substrate it is essential to identify the parameter compatibility with the active heterostructure (lattice mistmatch, thermal exposition coefficients) and fulfill the property requirements for the final device (thermal conductivity, optical transparency).

Sapphire is the conventional choice for III-nitride growth, for example it is the state-of-the-art for LED manufacturing technology. There are four conventional orientations of sapphire commonly used for heteroepitaxial growth: (10-10), (0001), (2-1-10) and (11-20). In present work mainly polar *c* polar films was considered. For example the lattice mismatch between GaN and (0001) sapphire is 13.9% consequently heteroepitaxy on such severely lattice-mismatched substrates makes the nucleation layer one of the most critical aspects of the growth.

The choice of the substrates used in this work was based on its optical transparency for ISB devices in IR spectral region and on the reasonable dislocation density.

- GaN-on-sapphire templates supplied by Lumilog. The template consists of ≈10-µm-thick (0001)-oriented GaN with very low dislocation density of $\approx 10^8$ cm^{-2}. The top epilayer of the substrates have an atomically smooth layer with atomic terraces typical for MOVPE growth (Fig. 3.20(a)).
- AlN-on-sapphire templates produced from DOWA consists of 1.0±0.3 µm thick (0001)-oriented AlN. The FWHM of X-ray ω-scan rocking curve is <100 arcsec for the (0002) reflection, and dislocation density of $\approx 10^9$ cm^{-2}. The top epilayer of the substrates have an atomically smooth layer with atomic terraces typical for MOVPE growth (Fig. 3.20(b)).
- GaN-on-Si(111) template consists of a commercial high electron mobility transistor (HEMT) structure grown by MOVPE on floating-zone Si(111). The FWHM of X-ray ω-scan rocking curve is ≈925 arcsec for the (0002) reflection and ≈1662 arcsec for the (10-12) reflection. An AFM image of the substrate is shown in Fig. 3.20(c).
- GaN(11-22)-on-sapphire templates from CRHEA, fabricated by G. Nataf and Ph. De Mierry (Mierry, 2009). The template consists of 1 µm thick GaN

epitaxial layer deposited by MOVPE on *m*-sapphire. An AFM image of the substrate is shown in Fig. 3.20(d).

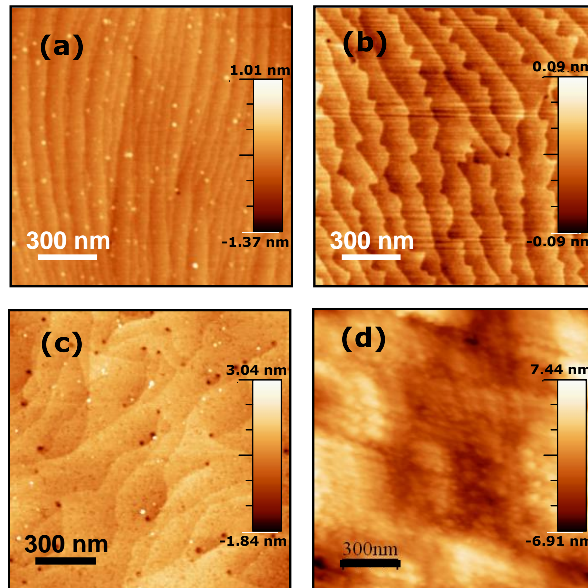

Figure 3.20. *AFM images of (a) GaN-on-sapphire templates, (b) AlN-on-sapphire templates, (c) GaN-on-Si(111) template, (d) GaN(11-22)-on-sapphire template.*

Figure 3.21 illustrates near- and mid-IR transmittance of the above described substrates measured by FTIR spectroscopy. The GaN(AlN)-on-sapphire templates are transparent in near-IR but have a cut off at ≈6 μm while GaN-on-Si(111) substrates are optically active until Restrahlen band of GaN.

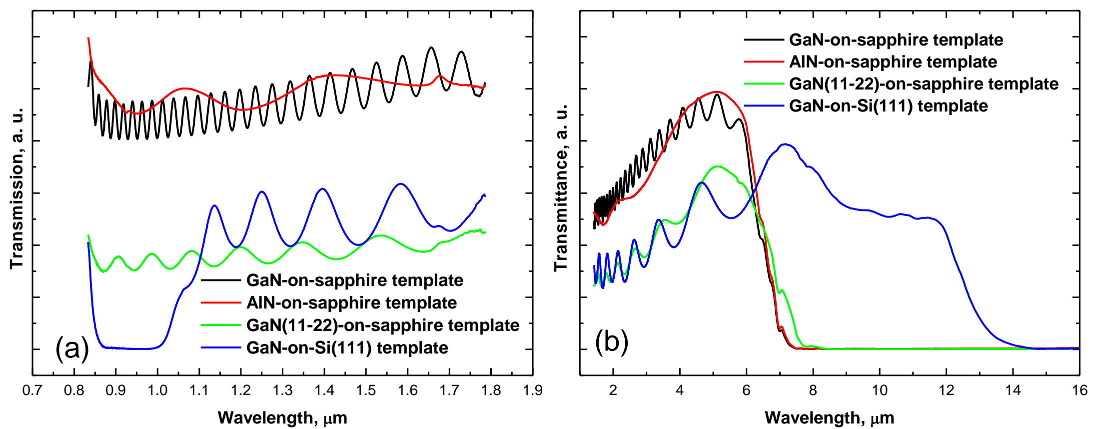

Figure 3.21. *Transmittance of substrates in (a) nea-IR and (b) mid-IR.*

3.5 Sample preparation for FTIR spectroscopy

As it was discussed in Chapter 2, the selection rule for ISB transitions imposes certain requirements on the performance of absorption measurement. The ISB transition is associated with light polarized perpendicular to the QWs. Therefore it implies special sample geometry. The sample geometry used for FTIR specroscopy is depicted in Fig. 3.22. For IR absorption measurement to build a multipass wave guiding structure the substrate sides of the samples were mirror polished and two opposite facets were lapped at 30° and 45° for HEMT-on-silicon and GaN-on-sapphire, respectively.

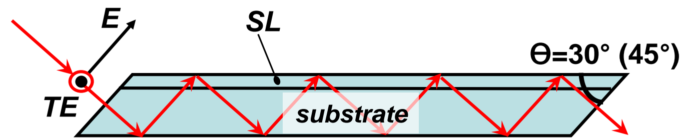

Figure 3.22. *Waveguide multipass gyometry for ISB measurements.*

The number of the reflections can be calculated using following formula

$$N = \frac{1}{2}\left(1 + \frac{l}{h\tan\theta} - \frac{1}{\sin^2\theta}\right), \qquad [3.8]$$

where l and h are the wavelength and thickness of the sample, respectively, Θ is the angle between the incoming beam and surface of the sample.

The facets of waveguiding structure for samples grown on silicon and sapphire templates are polished at different angles. In case of 45° geometry of silicon template the effect of total reflectance take place at GaN/Si interface as it seen in Fig. 3.23.(a). However, it is possible to avoid this problem by reducing the angle to 30° (Fig. 3.23(b)). The critical angle for the GaN and silicon materials is 42° therefore any angle inferior would allow penetration of the IR light from silicon substrate to GaN epilayer.

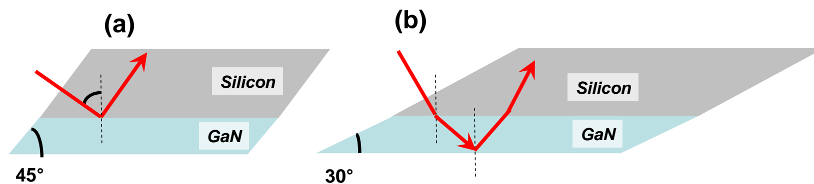

Figure 3.23. *Multipass waveguiding geometry of HEMT-on-Si template with two facets polished at (a) 45° and (b) 30°.*

Chapter 4

Strain relaxation mechanisms in GaN/AlGaN superlattices

The active region of ISB devices consists in general of several periods of GaN/Al(Ga)N QWs. In this chapter I will describe the modeling of GaN/AlGaN superlattices to tune their e_2-e_1 ISB transition in the near- and mid-IR spectrum. I will then describe the growth conditions that lead to 2D structures with sharp interfaces. As GaN/AlGaN is a lattice mismatched system for high device performance, it is crutial to understand the effects of strain and misfit relaxation at the buffer layer / active region interface, as well as the strain generated by layer alternation within the active region. Therefore, this chapter will present study of misfit relaxation process in GaN/AlGaN SLs with various Al mole fractions in barriers, and deposited on different buffer layers, i.e. under tensile and under compressive strain.

4.1 Introduction

The active region of ISB devices consists in general of several periods of GaN/Al(Ga)N QWs or coupled-QWs. As GaN/AlN is a lattice mismatched system (2.5% in-plane lattice mismatch), it is important to understand the effects of strain and misfit relaxation at the contact layer / active region interface, as well as the strain generated by layer alternation within the active region. Strain modifies the band profile by changing the semiconductor band gap and inducing piezoelectric polarization, with the subsequent effects on interband and ISB transitions. Moreover, in the case of GaN/AlN heterostructures, the interfaces can be unstable when grown under tensile stress (Boguslawski, 2000), which eventually leads to the formation of alloyed interfaces at high growth temperatures. This interface degradation affects the QW potential profile leading to a red shift of the ISB transition energies (Nicolay, 2007).

The strain in heterostructures can be released elastically by undulation of the surface, or plastically by introducing defects in the epilayers. Extended defects can affect the device properties causing nonradiative recombination, carrier scattering, and

enhanced diffusion of dopants and impurities. There are several types of plastic relaxation: crack propagation – commonly observed in III-nitrides under tensile stress, decohesion of the layer, introduction of misfit dislocations (MDs) or glide of pre-existing threading dislocations (TDs). In the case of nitride heterostructures grown along the [0001] axis, which is the predominant growth orientation in commercial devices, the formation of regular networks of MDs is hindered since the most crystallographically favorable slip system, the (0001) basal plane with <11-20>{0002} slip directions, lies parallel to the heterointerfaces (Ponce, 1997). However, MDs can be detected at heterointerfaces when shear stress is intentionally or unintentionally induced by three dimensional growth (Moran, 2004; Kehagias 2005), by crack formation (Hearne, 2004; Floro, 2004), or in close proximity to V-defects (Liu, 2006). Therefore, the relaxation mechanism depends not only on the structure itself, but also on the growth conditions.

Regarding GaN/AlGaN heterostructures, Bykhovski et al. (Bykhovski, 1997) calculated the theoretical critical thickness by assuming strain relaxation via formation of MDs with Burgers vector b = 1/3<11-20>, taking into account the interaction between dislocations. They theoretically predicted the possible arrangement of dislocations for different relaxation strengths concluding that relaxation in GaN/AlN SLs starts at a thickness of the individual layers slightly over 3 nm. However, there is no experimental confirmation of the assumed relaxation mechanism. In general, GaN/AlGaN heterostructures grown under tensile stress on GaN substrates tend to crack along the <11-20> crystallographic direction at a certain critical thickness (Hearne, 2000; Einfeldt, 2001). Associated to these cracks, relaxation via MDs following the secondary <11-23>{11-22} slip system has been reported in AlGaN layers deposited on GaN by metalorganic vapor phase epitaxy (MOVPE) (Floro, 2004). In the case of crack-free GaN/AlGaN SLs deposited on AlGaN by MOVPE, the growth of the SL induces a tilt of the a-type TDs towards <1-100>. The inclination angle depends on the lattice misfit between the SL and the underlayer (Cherns, 2008). The diagonal movement is due to a staircase-like movement of the dislocations through the stack, with a misfit segment at each well. Strain relaxation via TD inclination has also been observed in AlGaN layers deposited on mismatched AlGaN (Cantu, 2005).

In a previous PhD work (Kandaswamy, 2010a), the stress release in GaN/AlN (1.5 nm / 3 nm) SLs designed for 1.55 µm wavelength ISB absorption and deposited on AlN- and GaN-on-sapphire templates by PAMBE was analyzed (Kandaswamy, 2009). Strain relaxation was minimized by the growth of both GaN and AlN under Ga excess conditions. In this case, crack propagation is inhibited and the SL strain state gets independent of the substrate after about 20 periods. The initial relaxation of the SL is due to the formation of 60° ⅓‹11-20› dislocations in the basal plane, which fold into the prismatic plane and terminate at the surface. An inclination of the TDs propagated from the substrate is also observed. In addition, we identified a periodic relaxation associated to stacking fault (SF) loops in the AlN barriers.

In this work, I present a study of relaxation mechanisms in GaN/AlGaN SLs grown by PAMBE along the polar [0001] direction and designed for mid-infrared ISB absorption. We have considered the case of growth on GaN (tensile stress) and on AlGaN (compressive stress) buffer layers, both deposited on GaN-on-sapphire templates. To get a good insight into the strain relaxation, I analyzed the SLs using *in situ* and *ex situ* characterization techniques.

4.2 GaN/AlGaN superlattices: Electronic structure

The superlattice structures described in this chapter are designed to present e_1-e_2 ISB absorption in the near- and mid-IR spectral regions. To design samples I used the Nextnano^3 8×8 k·p Schrödinger-Poisson solver (Birner, 2007) developed by the Walter Schottky Institut of the Technische Universität München, Germany. With this software, it is possible to calculate not only the electronic configuration of common *c*-plane III-nitrides but also other semipolar or nonpolar orientations, by indicating the growth axis. The main advantages of the Nextnano^3 solver are that the material parameters are fully accessible and the simulations take into account the spontaneous and piezoelectric polarization coefficients, together with the strain state. In principle, these calculations do not consider many-body effects like exchange interaction and depolarization shift.

The GaN/AlN material parameters used for the simulations are described in Table 4.1 (Kandaswamy, 2008). For ternary alloys, the bowing parameter of the band

gap energy was taken as zero, and for spontaneous polarization we assumed a bowing of +0.019 C/m^2 (Fiorentini, 2002).

Table 4.1. *GaN and AlN parameters used for the calculations of band diagrams with the nextnano^3 solver.*

Parameters		GaN	AlN
Lattice constants, nm	*a*	0.31892	0.3112
	c	0.51850	0.4982
Spontaneous polarization, Cm^{-2}		-0.029	-0.081
Piezoelectric constants, Cm^{-2}	e_{13}	-0.49	-0.60
	e_{33}	0.73	1.46
Elastic constants, GPa	C_{11}	390	396
	C_{12}	145	140
	C_{13}	106	108
	C_{33}	398	373
Dielectric constant		10	8.5
Luttinger parameters	A_1	-5.947	-3.991
	A_2	-0.528	-0.311
	A_3	5.414	3.671
	A_4	-2.512	-1.147
	A_5	-2.510	-1.329
	A_6	-3.202	-1.952
	A_7	0	0
	$E_P^{//}$ [eV]	14	17.3
	$E_P^{\perp}$ [eV]	14	16.3
Deformation potentials, eV	a_{c1}	-4.6	-4.5
	a_{c2}	-4.6	-4.5
	D_1	-1.70	-2.89
	D_2	6.30	4.89
	D_3	8.00	7.78
	D_4	-4.00	-3.89
	D_5	-4.00	-3.34
	D_6	-5.66	-3.94
Band offset, eV		1.8	

A first series of GaN/AlGaN superlattices was designed to study their growth and structural properties and particularly the mechanisms of strain relaxation. The active region of the samples consists of 40 periods of 7 nm / 4 nm GaN/$Al_xGa_{1-x}N$ (x = 0.1, 0.3, 0.44) QWs. I consider a doping level in the QWs of [Si] = 5×10^{19} cm^{-3}, to

guarantee ISB absorption. The calculated band diagrams for various Al compositions are depicted in Fig. 4.1.

The sawtooth-like profile is attributed to the spontaneous and piezoelectric polarization present in wurtzite III-nitrides. The increase of Al composition in the barriers from x = 0.1 to x = 0.44 results in an enhancement of the internal electric field that red shifts the e_1-h_1 interband transition below the GaN bandgap. The structures were designed so as to have an ISB transition energy between the two first electronic levels in the QW e_2-e_1 ~ 80 meV (~ 15 µm wavelength), ~ 130 meV (~ 10 µm), and ~ 180 meV (~ 7 µm), for $Al_xGa_{1-x}N$ barriers with an Al mole fraction x = 0.1, 0.3, and 0.44, respectively.

To assess the effect of the lattice misfit on the electronic properties we compare two strain states: SL fully strained on GaN (tensile stress) and SL fully strained on $Al_xGa_{1-x}N$ (compressive stress) with the Al mole fraction corresponding to the barriers. According to the results in Fig. 4.1, strain affects more the e_1-h_1 interband transition than the e_2-e_1 ISB transition. The variation of e_1-h_1 is mainly due to the strain-induced modification of the bandgap. In contrast, e_2-e_1 is mostly determined by the internal electric field, since the two first electronic levels are located in the triangular section of the QWs. The ISB energy difference increases slightly in the SLs with a smaller in-plane lattice parameter which is related to the enhancement of the electric field in the QW, due to the larger piezoelectric coefficients of AlN in comparison to GaN (Bernardini, 1997). However the effect is relatively weak: ~ 14 meV for GaN/$Al_{0.44}Ga_{0.56}N$, i.e. 30% of the expected ISB absorption line width ($\Delta E/E \approx 20$ %, where ΔE is the full width at half maximum of the absorption and E is the absorption peak energy (Kandaswamy, 2009)), decreasing to ~ 0.8 meV for GaN/$Al_{0.1}Ga_{0.9}N$, i.e. only 2% of the expected line width.

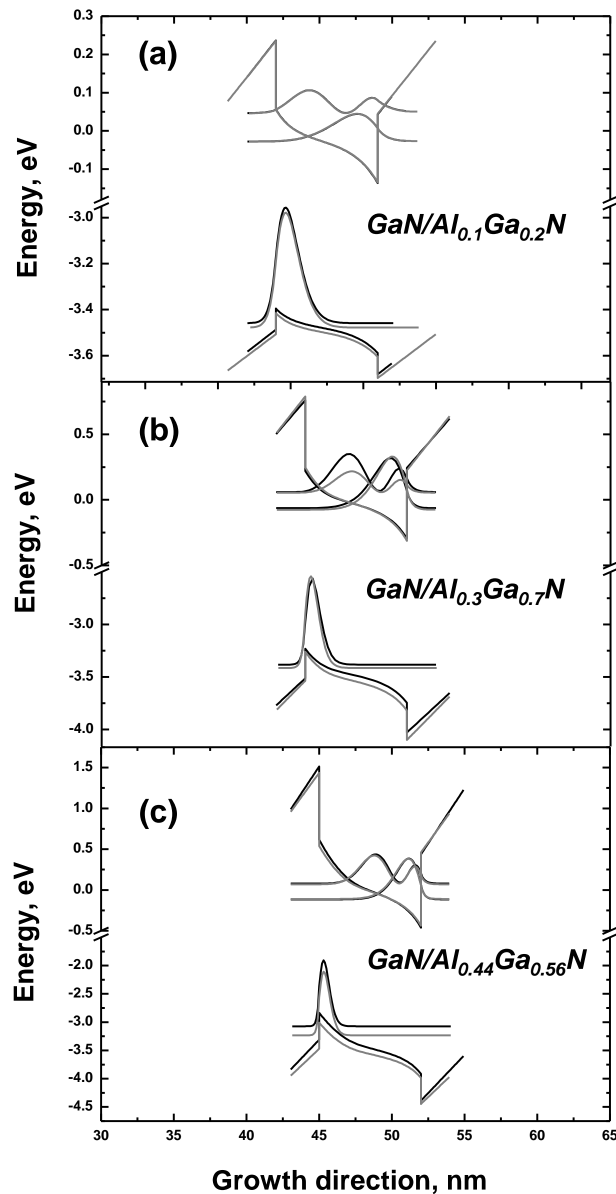

Figure 4.1. *Conduction band profile and squared envelope functions of QWs in GaN/*$Al_xGa_{1-x}N$ *(7 nm/4 nm) SLs with (a) x = 0.1, (b) x = 0.3, (c) = 0.44. Black (red) lines describe the structures fully strained on* $Al_xGa_{1-x}N$ *(GaN).*

4.3 Growth conditions for GaN/AlGaN SLs

The III-nitride heterostructures investigated in this work have been grown by the plasma-assisted molecular beam epitaxy technique described in the previous chapter. One of its advantages is the ultra-high vacuum environment and the use of the high-purity materials, which minimize contamination of the epilayers. The relatively low growth temperature of ≈720°C and a growth rate of about 270 nm/h allow having a

precise control of the growth process, resulting in abrupt interfaces and high reproducibility of the SLs. GaN layers with smooth surface morphology require slightly Ga-rich conditions at the growth temperature when Ga desorption still exist. At these conditions it is possible to achieve a dynamical equilibrium state with a certain Ga amount on top of the growing surface independently of the Ga flux (Heying, 2000; Northrup, 2000; Mula, 2001; Adelmann, 2003). The maximum Ga coverage that can be stabilized on the surface before accumulation of Ga droplets is ~2.5 ML. In order to delay elastic and plastic relaxation I calibrated Ga flux at the Ga accumulation limit. At this conditions Ga excess forms a laterally contracted biatomic layer that minimize the (0001) surface energy and prevents creation of the pits which are favorable relaxation channel in GaN-based material (Song, 2005; Northup, 1999).

Growth of 2D AlGaN also requires metal-rich conditions (Iliopoulos, 2002; Monroy, 2003). When growing alloys with Al content not exceeding 50% it is possible to achieve a good quality films under slightly Ga rich conditions. As the Al-N binding energy is much higher than the one of Ga-N, it is enough to fix Al/N ratio at the required Al content and the excess of Ga segregate at the growing surface not incorporating into the epilayer. The Al mole fraction was determined by RHEED oscillations during the AlN growth under Al-limited conditions.

4.4 Strain measurements

The vacuum environment during the MBE growth allows using a electron-beam-based characterization technique like RHEED in order to optimize the growth conditions and assess the relaxation processes in the heterostructures. We studied *in situ* misfit relaxation by RHEED measuring the distance between the (-10) and (10) streaks in the <11-20> azimuth, which is inversely proportional to the in-plane lattice parameter. As RHEED is a surface sensitive technique, the measured data describes the structure of the uppermost ~ 3 ML.

Figure 4.2(a) presents the evolution of the in-plane lattice parameter measured by RHEED during the growth of GaN/$Al_{0.1}Ga_{0.9}N$ (7 nm/4 nm) SLs deposited on a 300-nm-thick GaN (black line) or $Al_{0.1}Ga_{0.9}N$ (grey line) buffer layer. If we focus on the general trend, a uniform behavior of in-plane lattice parameter is observed in case of

the SL grown on GaN, which might point to pseudomorphic growth. In contrast, the SL deposited on $Al_{0.1}Ga_{0.9}N$ presents an initial gradual relaxation during about 20 periods. Once steady-state conditions are reached, a periodic fluctuation of in-plane lattice parameter remains in both SLs, as illustrated in the magnified image in Fig. 4.2(b). The origin of this periodic relaxation, observed in all the SLs under study, will be discussed later.

A similar behavior was observed in case of $GaN/Al_{0.3}Ga_{0.7}N$ SLs (Fig. 4.2(c)): Growth on GaN shows an uniform trend along the whole 40 periods, whereas the same SL deposited on $Al_{0.3}Ga_{0.7}N$ presents a gradual relaxation during the first 5 periods. If we further increase the Al mole fraction of the barriers to 44% (Fig. 4.2(d)), we observe the onset of relaxation in the structures grown on GaN. In this case, a gradual relaxation is observed in both SLs, which reach the same final strain state after about 20 periods.

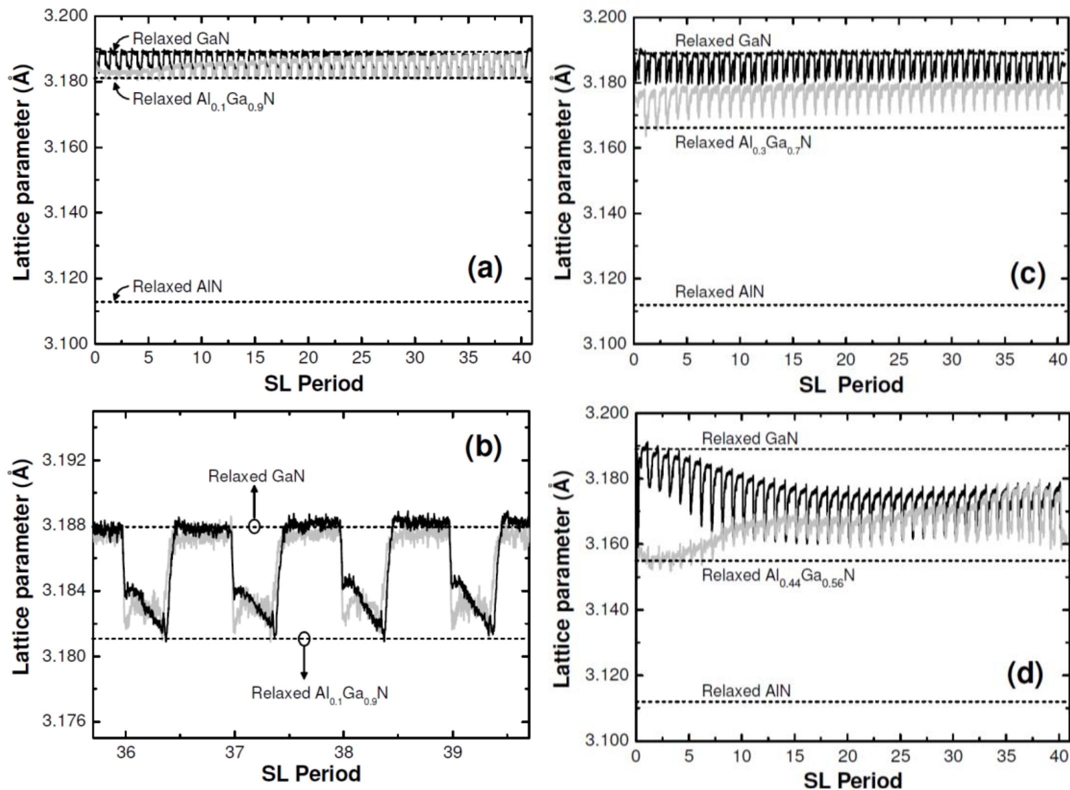

Figure 4.2. *RHEED measurement of the evolution of the in-plane lattice parameter during the growth of 40-period $GaN/Al_xGa_{1-x}N$ (7 nm / 4 nm) SLs grown either on $Al_xGa_{1-x}N$ (grey line) or on GaN (black line) buffer layers for (a,b) x = 0.1, (c) x = 0.3 and (d) x = 0.44. The lattice parameters of relaxed AlN, $Al_xGa_{1-x}N$ and GaN are indicated by dashed lines. Figure (b) is a magnified view of (a) illustrating the evolution of the in-plane lattice parameter in the last SL periods.*

An *ex situ* confirmation of the average RHEED trends was provided by HRXRD. We performed a symmetrical θ-2θ type of scan with the sample and the detector rotated by θ and 2θ, respectively. In reciprocal space it is represented as vertical measurement. The θ-2θ scans of the (0002) x-ray reflection of the GaN/$Al_xGa_{1-x}N$ (x = 0.1, 0.3, 0.44) SLs are presented in Figure 4.3. The simulations superimposed on the experimental scans were performed using the program X'Pert Epitaxy 4.0 from Phillips Analytical. It must be kept in mind that it is difficult to extract reliable information on the strain state and alloy composition from simulations of the θ-2θ scans. For instance, calculations using different well (barrier) thickness can fit the same experimental θ-2θ scans by keeping the period (well+barrier) thickness constant and tuning the Al content of the barriers. Therefore, chemical data and the strain state of the buffer layers are extracted from asymmetric reciprocal space maps, as described below, and the obtained data are used as input for the simulations, to verify that they indeed provide a good fit to the θ-2θ scans.

Analyzing the shape of the reflections in the θ-2θ scans, we can observe that in the case of $x = 0.1$ and $x = 0.3$ (Figs. 4.3(a) and (b), respectively) the structures deposited on $Al_xGa_{1-x}N$ buffer layers present broader SL reflections with asymmetric shape, which is consistent with a larger misfit relaxation. In the SLs with x = 0.44, the main SL reflection (labeled SL0 in the figure), presents an asymmetric shape with a tail towards larger (smaller) angles for the structure grown on GaN (AlGaN), which indicates a gradual misfit relaxation, as described in ref. (Bellet-Amalric, 2004) for III-N 2D layers. This result is consistent with the gradual evolution of the in-plane lattice parameter observed by RHEED (Fig. 4.2(d)).

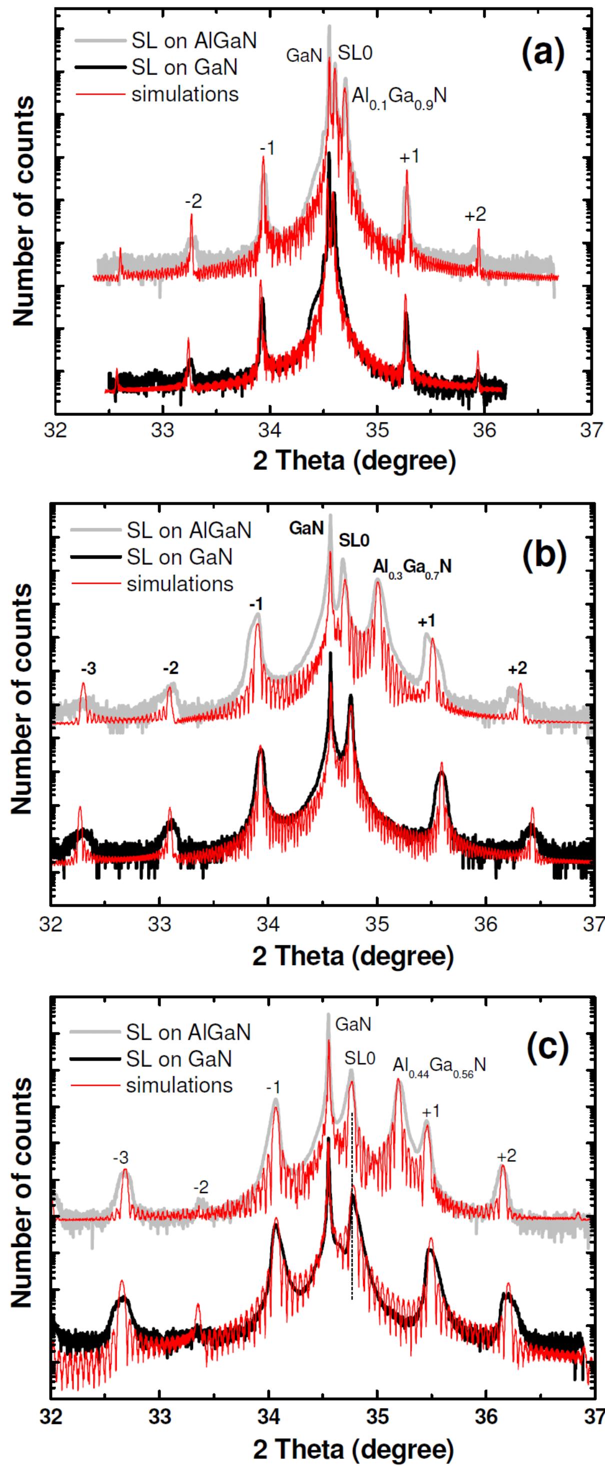

Figure 4.3. *X-ray θ -2θ scan of the (0002) reflection for 40-period GaN/$Al_xGa_{1-x}N$ (7 nm / 4 nm) SLs deposited on GaN and on $Al_xGa_{1-x}N$ buffer layers for aluminum mole fraction (a) $x = 0.1$, (b) $x = 0.3$, and (c) $x = 0.44$. The superimposed thinner simulations (red curves) were performed using the program X'Pert Epitaxy 4.0 from Phillips Analytical.*

Interference peaks or Kiessig fringes are also seen in some θ-2θ scans at the base of the diffraction peaks (Fig. 4.4); these fringes are associated with the reflection from

bottom and top of the SL. Therefore, the total thickness of the structures (Table 4.2) were calculated using following equation

$$H = \frac{(n_i - n_j)\lambda}{2(\sin\theta_i - \sin\theta_j)} \quad [4.1]$$

where λ is the X-ray wavelength, and θi and θj are the angles corresponding to the *i* and *j* order fringes. The extracted values, summarized in Table 4.2, are consistent with the total thickness of the superlattices consisting of 40 periods of GaN/AlGaN.

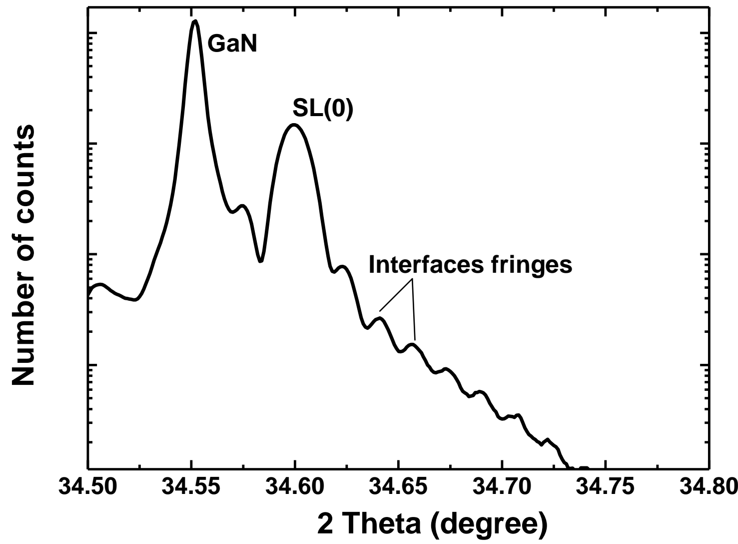

Figure 4.4. *X-ray θ-2θ scan of the (0002) reflection for 40-period GaN/$Al_{10}Ga_{90}N$ (7 nm / 4 nm) SLs deposited on GaN with Kiessig fringes at the base of the diffraction peaks.*

As mentioned above, the Al mole fraction is calculated from asymmetrical reciprocal space maps, which provide also information on the relaxation state of the AlGaN buffer layers. Figure 4.5 shows the RSMs around the (10-15) reflection of the GaN/$Al_xGa_{1-x}N$ (x = 0.1, 0.3, 0.44) SLs on GaN and $Al_xGa_{1-x}N$ buffer layers. Several SL satellites presented in the reciprocal space maps indicates excellent periodicity of the layers. The average SL in-plane lattice parameters, $\langle a_{SL} \rangle$, and the in-plane lattice parameter of the AlGaN buffer layers, a_{AlGaN}, were calculated from the RSMs using the $\langle c_{SL} \rangle$ values extracted from the θ-2θ scans (more precise than the ones extracted from the RSMs). The obtained values are summarized in Table 4.2. As the *c* value is used in the calculation of *a*, the latter has larger error bars. Increased error in *c*

parameter for the SL grown on $Al_{0.3}Ga_{0.7}N$ buffer layer comes from overlapping of zero-order SL peak and buffer reflection.

Table 4.2. *Parameters of GaN/ $Al_xGa_{1-x}N$ SLs or $Al_xGa_{1-x}N$ buffer layers extracted from HRXRD spectroscopy: average lattice parameters of the SL and of the AlGaN buffer layer, percentage of relaxation of the AlGaN buffer layer, SL period and total SL thickness.*

Parameter	**10%**		**30%**		**44%**	
	on GaN buffer	**on AlGaN buffer**	**on GaN buffer**	**on AlGaN buffer**	**on GaN buffer**	**on AlGaN buffer**
$\langle a_{SL} \rangle$, Å	3.189	3.188	3.194	3.173	3.176	3.179
$\langle c_{SL} \rangle$, Å	5.180	5.180	5.162	5.164	5.156	5.158
a_{AlGaN}, Å	-	3.192	-	3.170	-	3.165
c_{AlGaN}, Å	-	5.166	-	5.122	-	5.094
R_{AlGaN}, %	-	94	-	86	-	51
T, nm	13.9	13.9	13.3	12.1	13.1	13.3
H, nm	598	411	520	-	-	-

In the case of the AlGaN buffer layers, having the values of the lattice parameters *a* and *c*, it is possible to extract the alloy composition and relaxation state. The alloy composition and the strain both influence on lattice parameters of the structure. The buffer layers are tensile strained on GaN-on-sapphire templates in the beginning of the growth and they tend to relax after a certain critical thickness. Writing Eq. 2.14 for alloyed layer which is valid in case of the biaxial strain and presenting relaxed lattice parameters of alloy via Vegard's law (Eq. 2.2) we obtain

$$f(x) = \frac{c - xc_0(AlN) + (1-x)c_0(GaN)}{xc_0(AlN) + (1-x)c_0(GaN)} + 2\frac{C_{13}}{C_{33}}\frac{a - xa_0(AlN) + (1-x)a_0(GaN)}{xa_0(AlN) + (1-x)a_0(GaN)} = 0 \quad [4.4]$$

The Al composition of the buffer layers were found iteratively by minimizing *f*(*x*) in Eq. 4.4 i. e. finding *x* at which Eq. 4.4 tends to zero (Kisielowski, 1996; Schuster, 1999). The values of *x* are summarized in Table 4.2, together with the relaxation degree of the $Al_xGa_{1-x}N$ buffers layers, defined by

$$R = \frac{a^{AlGaN}_{measured} - a^{GaN}_{theor}}{a^{AlGaN}_{theor} - a^{GaN}_{theor}} 100\% \quad [4.2]$$

If we look at the RSM in Fig. 4.5, in case of $GaN/Al_xGa_{1-x}N$ SLs with x = 0.1, 0.3 (Fig. 4.5(a) and (c)) grown on GaN the structures look fully strained, whereas in the case of $Al_xGa_{1-x}N$ (x=0.3, 0.44) buffers and for the $GaN/Al_{0.44}Ga_{0.66}N$ SL on GaN the

SL reflections are shifted along Qx from the reflection of the buffer, which is in agreement with relaxation observed by RHEED.

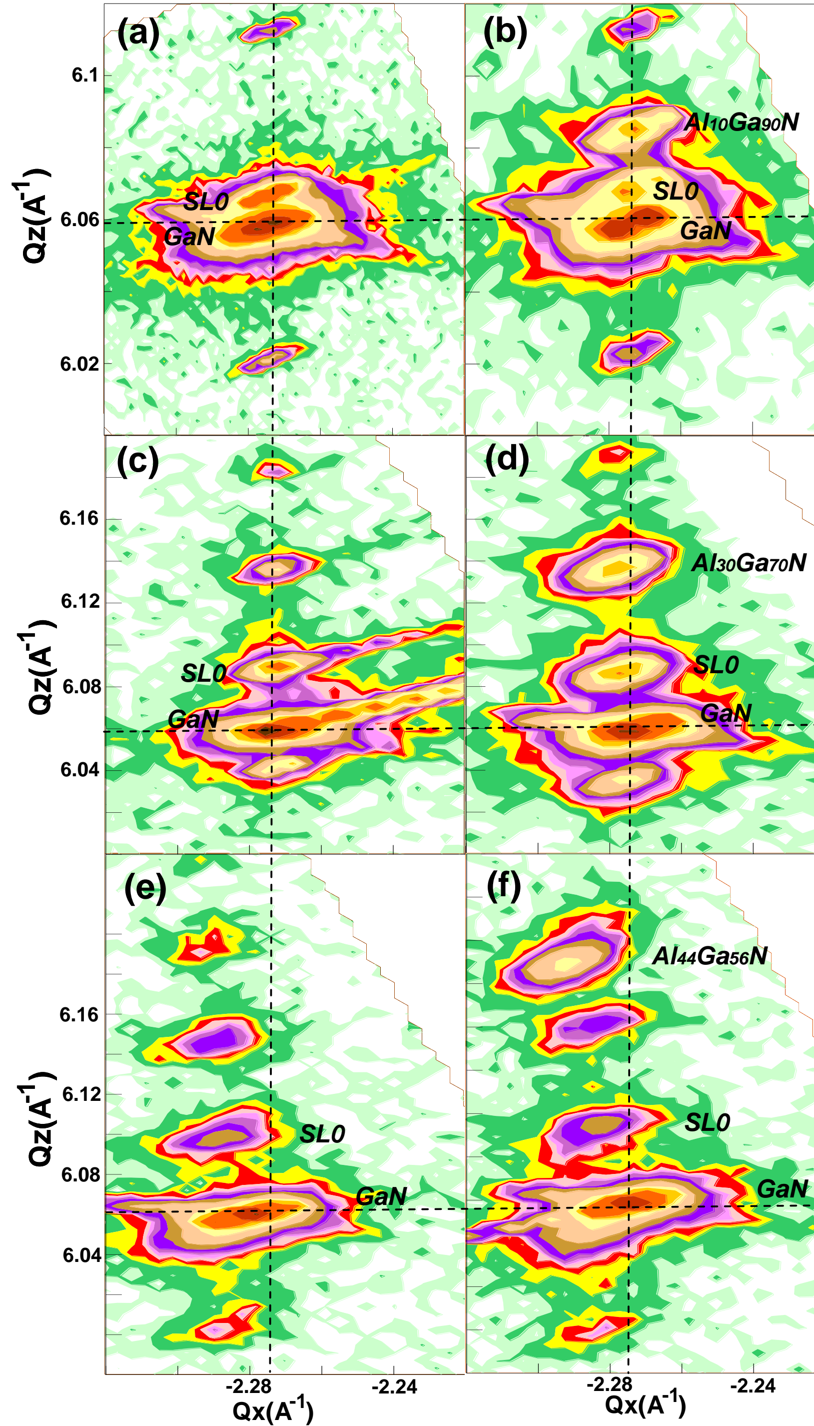

Figure 4.5. *Reciprocal space maps around the asymmetric (10-15) x-ray reflection of* $GaN/Al_xGa_{1-x}N$ *SLs grown on GaN or* $Al_xGa_{1-x}N$ *buffer (a,b) with x = 0.1, (c,d) x = 0.3, (e,f) x = 0.44.*

The defect structure associated to the misfit relaxation in these SLs was analyzed by transmission electron microscopy (TEM). Figure 4.6 presents conventional TEM images viewed along the <1-100> zone axis of $GaN/Al_{0.1}Ga_{0.9}N$ SLs grown on GaN and on $Al_{0.1}Ga_{0.9}N$ buffer layers. In the case of the SL on GaN, Figs. 4.6(a) and (b) are measured close to weak-beam (g,3g) conditions with diffraction vector g = (0002) and g = (11-20), respectively. Considering the invisibility criterion for dislocations g.*b* = 0, where g is the diffraction vector and *b* is the Burgers vector, the line defects in Fig. 4.6, which get in contrast in the image with g = (11-20) and not in the case of g = (0002), are attributed to *a*-type TDs, i.e. with Burgers vector *b* = ⅓<11-20>, generated at the beginning of the SL growth with a density lower than 9×10^{8} cm^{-2}. They are probably connected to plastic relaxation via dislocations in the basal plane, which fold to give rise to TDs. In the case of the structure deposited on $Al_{0.1}Ga_{0.9}N$ [Fig. 4.6(c), measured under two-beam condition with g = (11-20)], a number of dislocations generate within the $Al_{0.1}Ga_{0.9}N$ buffer layer and propagate along the whole structure, terminating at the surface. Then, TDs are also generated inside the SL, with a density double as compared to the SL grown on GaN. All these dislocations present a Burgers vector *b* = ⅓<11-20>, since they are invisible in images with g = (0002) (not shown). This is consistent with the higher plastic relaxation measured by RHEED, and the broadening of the SL reflections in the θ -2θ scan.

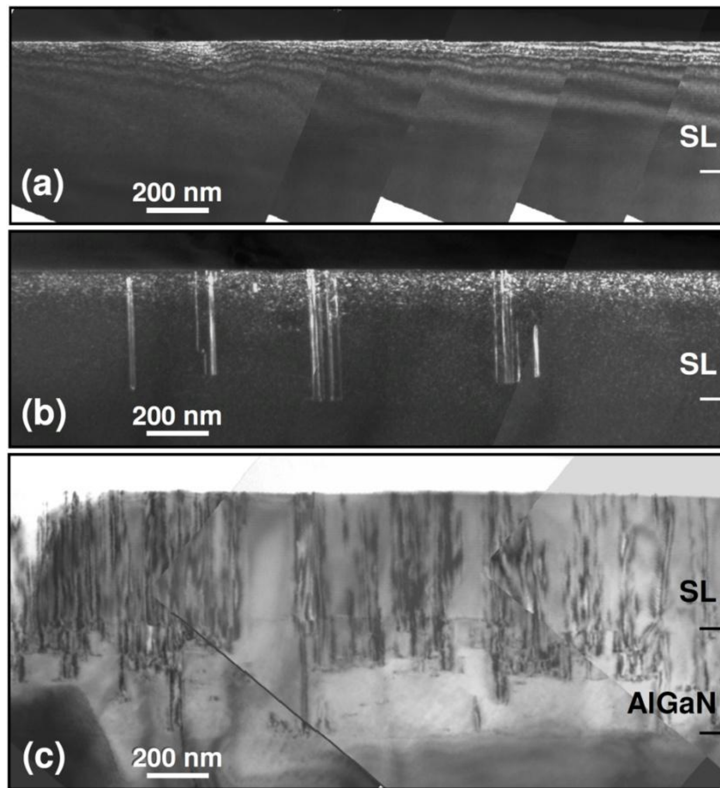

Figure 4.6. *Conventional TEM images of GaN/$Al_{0.1}Ga_{0.9}N$ SLs viewed along the <1-100> zone axis. (a,b) Structure grown on GaN buffer layer measured close to weak-beam (g,3g) conditions with diffraction vector g = (0002) and g = (11-20), respectively. (c) Structure deposited on $Al_{0.1}Ga_{0.9}N$ buffer layer measured under two-beam condition with g = (11-20).*

Increasing the Al content in the barriers and in the buffer layer up to 30%, the relaxation trend remains similar. Figures 4.7(a) and (b) show two-beam TEM images of the SLs grown on GaN and on $Al_{0.3}Ga_{0.7}N$ buffer layers, respectively, viewed along the <1-100> zone axis with diffraction vector g = (11-20). TEM images with g = (0002) did not show line defects in contrast, which confirms that the dislocations involved are *a*-type TDs. The dislocation density in the case of the SL grown on GaN is ~ 2×10^9 cm^{-2}, and it remains slightly lower than the dislocation density generated along the SL deposited on an $Al_{0.3}Ga_{0.7}N$ buffer, about 3×10^9 cm^{-2} .

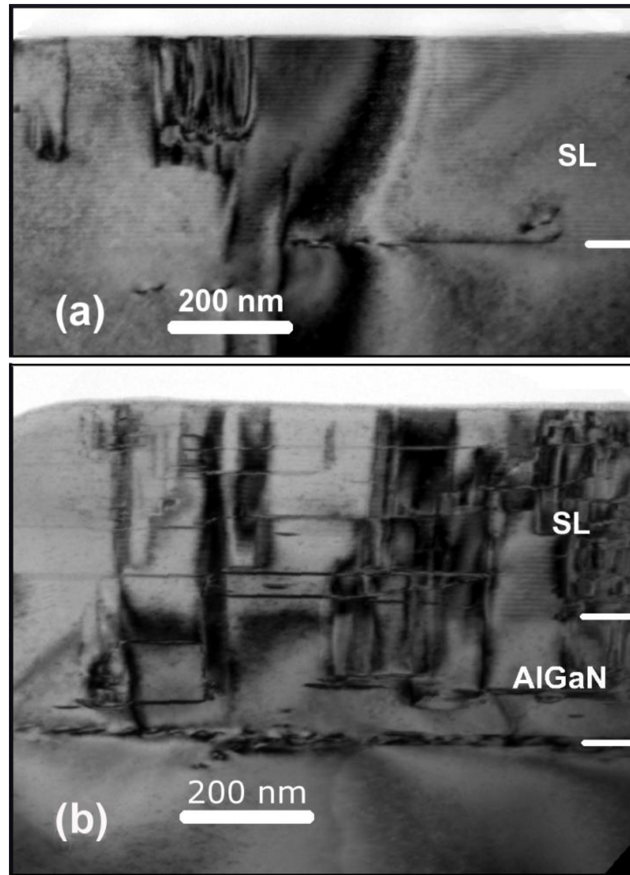

Figure 4.7. *Two-beam TEM images of GaN/$Al_{0.3}Ga_{0.7}N$ SLs deposited (a) on GaN and (b) on $Al_{0.3}Ga_{0.7}N$, viewed along the <1-100> zone axis with diffraction vector g = (11-20).*

Figure 4.8 presents two-beam TEM images viewed along the <1-100> zone axis of the GaN/$Al_{0.44}Ga_{0.56}N$ SLs grown on GaN and $Al_{0.44}Ga_{0.56}N$ buffer layers. In the case of the SL on GaN, Figs. 4.8(a) and (b) are taken with diffraction vectors g = (0002) and g = (11-20), respectively. The plastic relaxation involves the formation of *a*-type TDs [out of contrast in Fig. 4.8(a) and in contrast in Fig. 4.8(b)], but we observe also some screw/mixed dislocations that are present in both (a) and (b) images. In the g = (11-20) image of the sample with an AlGaN buffer layer [Fig. 4.8(c)], we observe a tilt of the threading dislocations in the buffer layer (about 20° from the growth axis), as previously observed in AlGaN layers with high Al mole fraction (Cantu, 2005). During the SL growth, the TD density reaches ~ 1.7×10^{10} cm^{-2}, both for the structure deposited on GaN and on AlGaN. These values of TD density are comparable to the ones observed in GaN/AlN SLs (Kandaswamy, 2009), although in the binary SL the TD tilt approaches 40°.

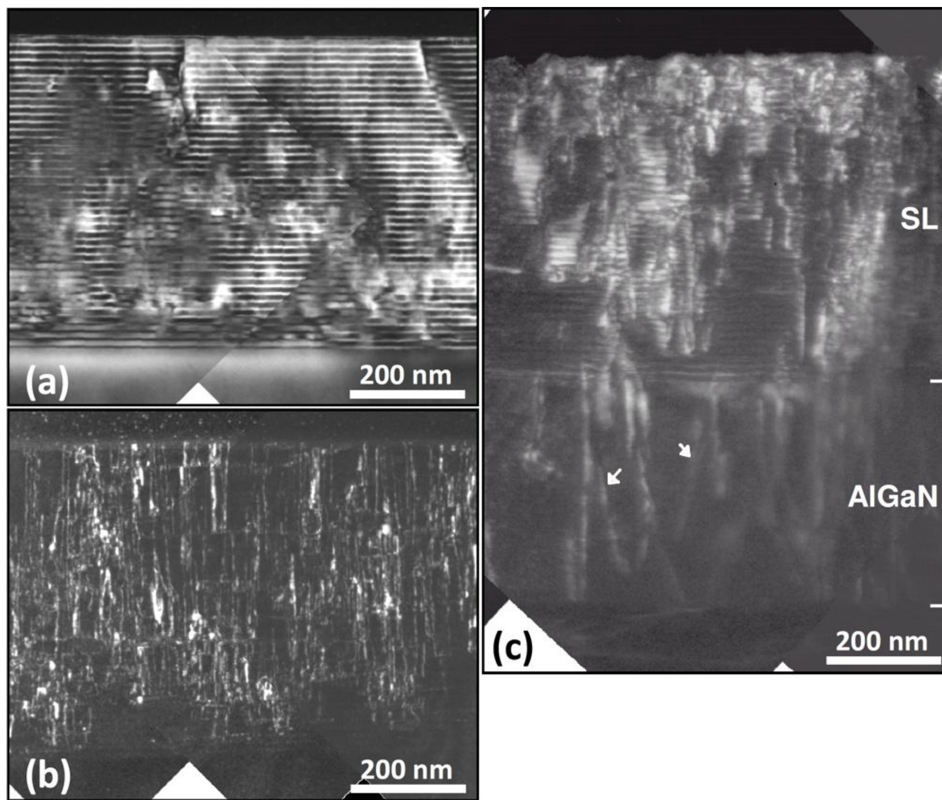

Figure 4.8. *Two-beam TEM images of GaN/$Al_{0.44}Ga_{0.56}N$ SLs viewed along the <1-100> zone axis. (a,b) Structure deposited on GaN measured with g = (0002) and g = (11-20), respectively. (c) SL on $Al_{0.44}Ga_{0.56}N$ buffer layer taken measured g = (11-20). White arrows indicate TDs in the AlGaN buffer layer which are tilted of about 20° from the growth axis.*

High-resolution TEM experiments were performed in order to determine the origin of periodic relaxation observed by RHEED [Fig. 4.2(b)]. Figure 4.9 presents an example of high-resolution viewgraph from the GaN/$Al_{0.44}Ga_{0.56}N$ SL deposited on GaN. Analyzing images from different regions of the samples, both near the <1-100> and near the <11-20> axis, we did not identify any periodical defect structure. In particular, the interfaces appear sharp and the stacking fault loops reported in GaN/AlN SL (Kandaswamy, 2009) were not detected in any of the samples. The lack of *ex situ* evidence of periodic relaxation lead to assign the RHEED observation to an elastic phenomenon related to the growth kinetics.

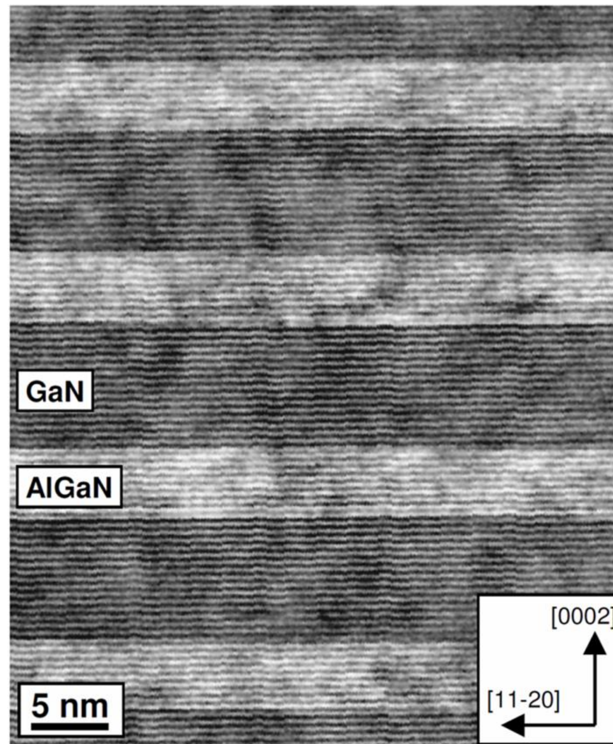

Figure 4.9. *High-resolution TEM image of the GaN/$Al_{0.44}Ga_{0.56}N$ SL deposited on GaN viewed along the <1-100> zone axis.*

The growth of the SLs is performed with a Ga excess layer wetting the growing surface. Therefore, to explain the fluctuation of in-plane lattice parameter illustrated in Fig. 4.2(b), we studied the behavior of (Al,Ga)N surfaces under Ga exposure, using (Al,Ga)N samples with a thickness of at least 200 nm. Figure 4.10 shows RHEED measurements of the evolution of the in-plane lattice parameter when the different surfaces are exposed to a Ga flux. The experiment starts with the (Al,Ga)N surface in vacuum; the Ga shutter opens at $t = 0$. During the first 10 s, we often observe an initial transient, which appears as a negative overshoot particularly marked in the case of GaN and AlN, is associated to an initial undulation of the surface, with the RHEED pattern evolving from well-defined straight lines to undulated lines and back to the straight pattern. This result is consistent with previous reports (Kandaswamy, 2009). After 10s, the lattice parameter stabilizes at a value corresponding to a compressive strain between 0.1% and 0.35%, depending on the Al mole fraction of the surface. When shuttering the Ga cell at 20 s, the lattice slowly recovers to its initial value at $t = 0$ as the Ga excess is desorbed. The complete desorption takes between 40 and

100 s, depending on the nature of the surface and being very sensitive to the surface temperature.

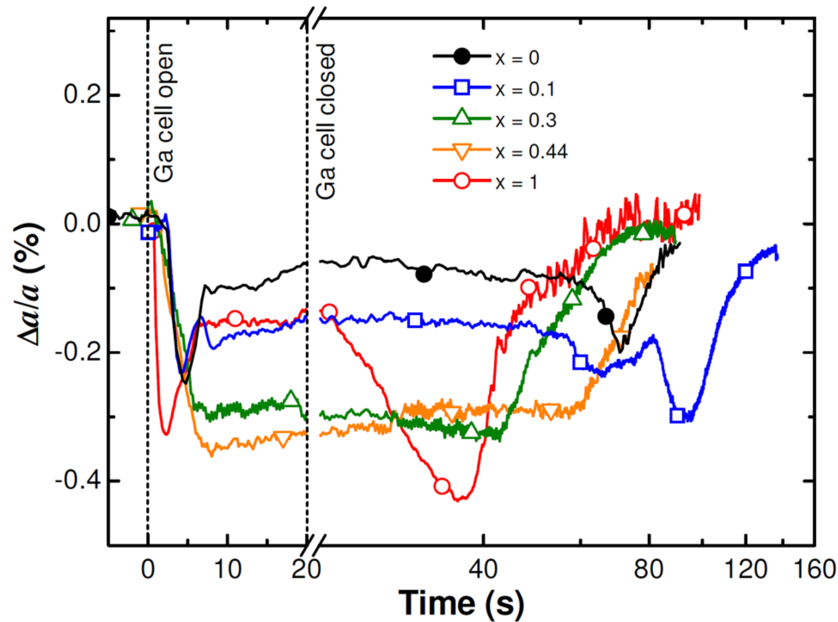

Figure 4.10. *RHEED measurement of the evolution of the in-plane lattice parameter induced by depositing Ga on top of GaN, AlN and* $Al_xGa_{1-x}N$ *(x = 0.1, 0.3, 0.44) surfaces at* T_s*=720ºC. Starting from the bare surface under vacuum, the Ga cell is opened at time t = 0 and shuttered at t = 20 s.*

The fact that after the Ga exposure-desorption process we find the same lattice parameter than at t = 0 indicates that the variations correspond to a purely elastic relaxation, without formation of defects. In the case of the $Al_xGa_{1-x}N$ (x = 0.1, 0.3, 0.44) surfaces, the decrease of the in-plane lattice parameter under Ga exposure ($\Delta a/a$) increases for higher Al mole fractions, reaching a value of 0.35% for 44% Al in the alloy. The magnitude of the fluctuation is enough to explain the variation of the in-plane lattice parameter in each period observed in the RHEED measurements of GaN/AlGaN SLs (Fig. 4.2).

This elastic deformation induced by the Ga excess is larger in the case of ternary alloys than for GaN and AlN. In the GaN/AlN system, the magnitude of the lattice parameter fluctuations cannot be explained just by the Ga excess, as confirmed by the *ex situ* identification of periodic defect structures (Kandaswamy, 2009).

4.5 Conclusions

I have investigated the misfit relaxation process in 40-period 7 nm/4 nm GaN/$Al_xGa_{1-x}N$ SLs (x = 0.1, 0.3, 0.44), designed for mid-infrared ISB absorption in the 5–10 μm spectral range and deposited by PAMBE. In the case of growth on GaN (tensile stress), the SL remains almost pseudomorphic for x = 0.1-0.3, with edge-type TD densities below 9×10^8 cm^{-2} to 2×10^9 cm^{-2}. Increasing the Al mole fraction to 0.44, we observe an enhancement of misfit relaxation resulting in dislocation densities above 10^{10} cm^{-2}. In the case of growth on AlGaN (compressive stress), we observe a stronger relaxation whatever the Al mole fraction (x = 0.1, 0.3, 0.44), with the corresponding increase of the density of edge-type threading dislocations. In addition to the average relaxation trend of the SL, RHEED measurements indicate a periodic fluctuation of the in-plane lattice parameter during the growth. In the case of GaN/AlN, these fluctuations were associated to a plastic deformation with appearance of dislocations associated to stacking fault loops. In contrast, I have demonstrated that in GaN/$Al_xGa_{1-x}N$ (x = 0.1, 0.3, 0.44) SLs the observed fluctuations are explained by different elastic response of the GaN and AlGaN surfaces to the Ga excess at the growth front.

Chapter 5

Effect of the QW doping on ISB absorption in GaN/Al(Ga)N SLs

In this chapter I present a study of silicon doping of GaN/Al(Ga)N SLs designed for near- and mid-IR ISB absorption. When dealing with SLs for mid-IR ISB absorption, i. e. SLs with reduced Al content in the barriers, the issues associated with material and design come out. Achieving efficient ISB absorption at longer wavelengths requires heavy silicon doping of the QWs. Consequently, the two-level single-particle theory, well suited for transitions in the near-IR leads to a large discrepancy between simulations and experimental results in mid-IR spectral range.

The active medium of the ISB devices has to be properly doped in order to observe ISB absorption, i.e. the ground confined state must be populated. High doping levels are required to achieve efficient ISB absorption -which perturbs the idea of two-level single-particle transitions usually employed to understand the absorption process in slightly doped samples with large confinement. Understanding and quantifying the effect of doping becomes a priority for the design of GaN-based ISB structures and devices operating in the mid- and far-IR spectral region.

Previous studies on GaN/AlN SLs designed for ISB absorption at 1.55 μm wavelength demonstrated that doping densities in the range of 5×10^{19} cm^{-3} do not alter the structural properties of the SLs measured by AFM, TEM or XRD (Kandaswamy, 2008). However, Si doping enhances, broadens, and blue shifts the ISB absorption of GaN/AlN SLs (Helman, 2003). In this spectral range, the blue shift of the ISB transition is attributed to many-body effects, mostly to the exchange interaction. No clearly identified effect could be associated to the location of Si donors when comparing samples where Si was introduced in the barriers, in the QWs or by delta doping (Kandaswamy, 2010).

The effect of doping in SLs has already been studied in the arsenide material system. For instance, Manasreh *et al*. (1991) studied the ISB absorption of MBE-

grown $GaAs/Al_{0.3}Ga_{0.7}As$ multiple QWs as a function of the silicon concentration in the GaAs QWs. The low-temperature ISB absorption peak blue shifts when increasing the carrier density, which is opposite to the prediction of single particle calculations. However, taking into account depolarization shift, exciton-like, the ground state electron-electron exchange interaction and the ground state direct Coulomb interaction effects leads to good compliance of calculations with experimental results.

When shifting the ISB transition from the near-IR towards longer wavelengths, using GaN/AlGaN QWs, many-body effects are expected to become more relevant since the relative shift of the ISB transition becomes larger. The reduction of the internal electric field associated to piezoelectric and spontaneous polarization translates into screening effects at lower doping levels, and the magnitude of exchange interaction and depolarization shift must be re-evaluated. In this chapter, I analyze the effect of silicon doping on the optical performance of GaN/AlGaN SLs designed for operation in the near- and mid-IR.

5.1 Modeling of the superlattice electronic structure

I have studied the effect of Si doping in 40 period $GaN:Si/Al_xGa_{1-x}N$ SLs designed to obtain near- and mid-IR ISB absorption. For these experiments, the sample structures (QW width and alloy composition in the barriers) were chosen to have at least two electronic levels in the QWs. The silicon concentration in the QWs was varied from 10^{18} to 10^{20} cm^{-3}. The choice of substrate, either GaN-on-sapphire (AlN-on-sapphire) or HEMT-on-Si, depends on the expected absorption wavelength, silicon being preferred as a base for samples absorbing at wavelengths longer than 4 µm. Figure 5.1 shows the sample structures of the three series and the calculations of band profiles and confined levels calculated using the nextnano^3 8-band k•p Schrödinger-Poisson solver. The band structures present the characteristic sawtooth profile associated to the intense spontaneous and piezoelectric polarization fields. The doping levels and e_1-e_2 (e_2-e_3) energy separations predicted by nextnano^3 solver are summarized in Table 5.1. The nextnano^3 solver accounts only for screening effect of the built in electric field therefore it predicts red shift of the ISB absorption with increasing silicon concentration in QWs.

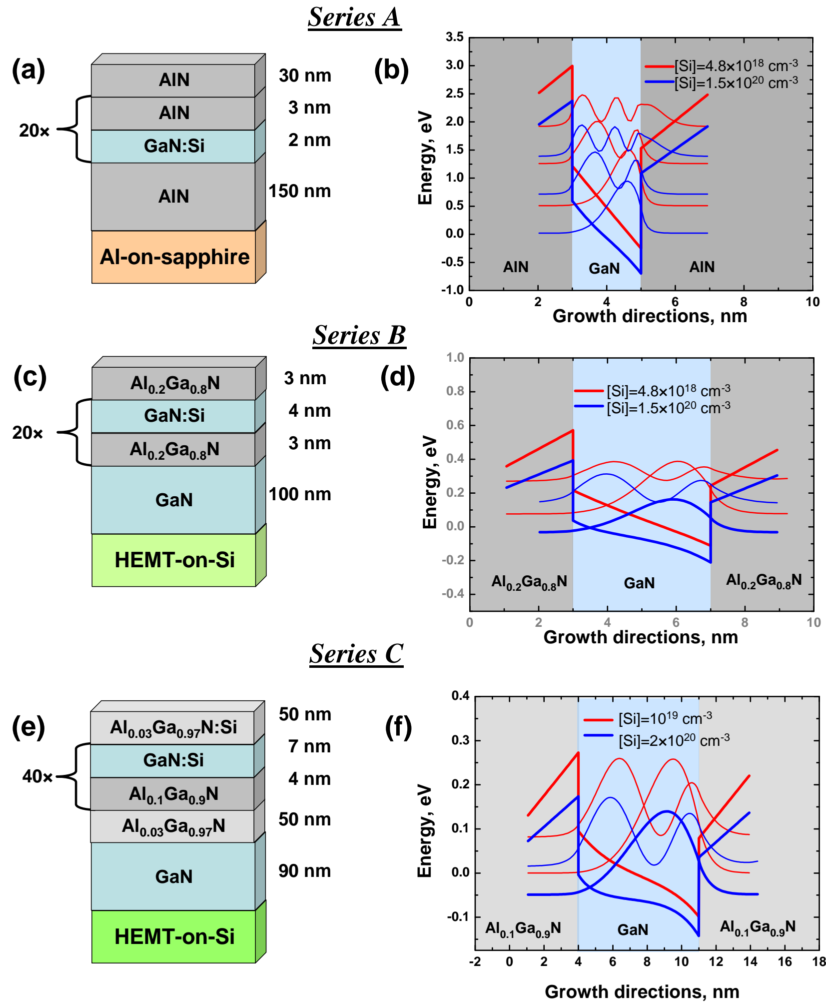

Figure 5.1. *(a, c, d) Sample structures and (b, d, e) band profiles calculated using nextnano[3] solver for the 3 series of SLs with different silicon doping level in QWs.*

Table 5.1. *Series of GaN/Al$_x$Ga$_{1-x}$N SLs designed for near- and mid-IR ISB absorption.*

	Sample number	Si doping in QWs of the SL, cm^{-3}	Calculated e_1-e_2, μm
Series A	E2690	4.8×10^{18}	1.66
	E2691	1.7×10^{19}	
	E2692 (E2694)	5.2×10^{19}	
	E2693	1.5×10^{20}	1.78
Series B	E2740	Undoped	
	E2744	4.8×10^{18}	5.87
	E2747	1.6×10^{19}	
	E2748	5.2×10^{19}	
	E2746	1.5×10^{20}	6.85
Series C	E2165	1×10^{19}	13.9
	E2163	2×10^{19}	
	E2167	5×10^{19}	
	E2161	1×10^{20}	
	E2169 (E2171)	2×10^{20}	17.2

The growth of the GaN/AlGaN SLs described in Fig. 5.1 was performed by PAMBE under Ga-rich conditions and at a substrate temperature $T_S = 720°C$, as described in Chapter 3. The detailed structural analysis of this kind of structures was presented in Chapter 4.

5.2 Silicon location

The calibration of the silicon effusion cell was made by performing Hall-effect measurements on ~700 nm thick GaN layers deposited on AlN-on-sapphire templates and doped with silicon varying the dopant cell temperature, as illustrated in Fig. 5.2.

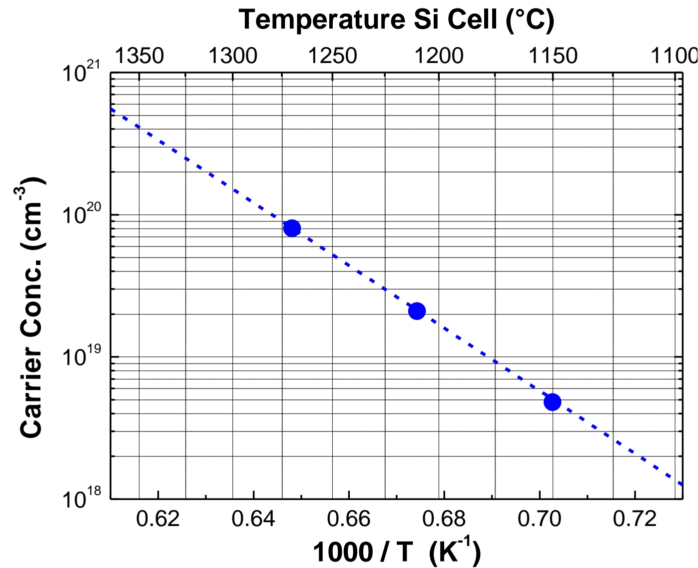

Figure 5.2. *Carrier concentration in 700 nm thick Si-doped GaN layer deduced from Hall-effect measurements versus temperature of silicon effusion cell.*

Then, silicon doping is performed by exposing the growing surface to the silicon flux during the deposition of the GaN quantum wells, and the silicon cell remains shuttered during the growth of the Al(Ga)N barriers. However, diffusion, segregation or selective incorporation can lead to deviations from the nominal doping profile. To confirm the location of Si atoms in the QWs, secondary ion mass spectroscopy (SIMS) of a GaN:Si/AlN (3 nm / 3 nm) SL was performed by Wei Ou at Evans Analytical Group (EAG), using Cs as a primary beam. The obtained Ga, Al, and Si profiles are presented in Fig. 5.3. Within the resolution of the measurement technique, Si is preferentially located within the GaN QWs. However, the fact that the Si distribution

appears shifted towards the bottom of the GaN layer might be attributed to an artifact induced by SIMS method, according to the EAG analysts. The silicon peak concentration, [Si] = $2.5\text{x}10^{19}$ cm^{-3}, is consistent with the expected doping level defined by temperature of the silicon effusion cell. The sharpness (peak to valley ratio) in Fig. 5.3 of the Al and Ga profiles decreases with depth. This dampening in the SL structure is due to the roughening of the samples induced by the SIMS primary beam.

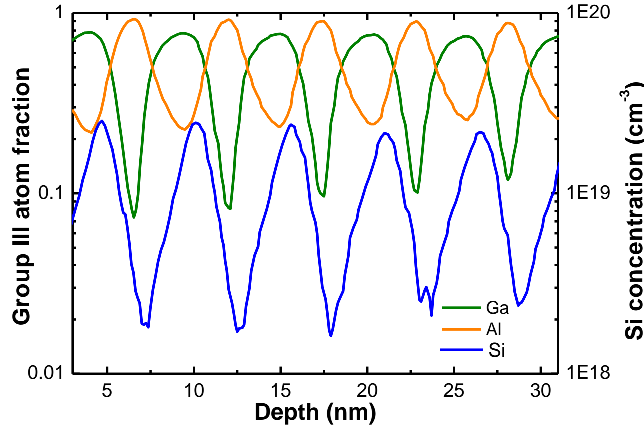

Figure 5.3. *High depth resolution SIMS measurement of* GaN:Si/AlN (3 nm / 3 nm) *SL (performed by Wei Ou at Evans Analytical Group laboratory).*

The annealing associated to the growth of the cap layers and the rapid changes of temperature during the device fabrication process should not lead to the intermixing of the material at the interfaces; however, they may promote the Si diffusion. To assess this issue, Hofstetter *et al*. (2011) studied effect of rapid thermal annealing on the ISB absorption and photovoltage characteristics of Si-doped GaN/AlN SLs. For this purpose, I grew a 40 period GaN/AlN (3 nm/15 nm) SL by plasma-assisted MBE on AlN-on-sapphire template, with silicon concentration in the QWs [Si] = 5×10^{19} cm^{-3} (Fig. 5.4(a)). The deposition of the SL was performed at a growth temperature of 720°C in order to achieve sharp interfaces between GaN and AlN. To study the silicon diffusion, various pieces of the sample were annealed at 1000°C for different time periods under NH_3 atmosphere (1000 mbar) in an MOVPE reactor. The interdiffusion of Si atoms to the barriers results in subsiding of the ISB absorption peak.

Figure 5.4(a) represents a theoretical calculation of the band structure of the sample, and Fig. 5.4(b) illustrates the sample transmission measured by FTIR in samples annealed for different time periods at 1000°C. The absence of a shift in ISB absorption peak position demonstrates that at this temperature the thickness of the GaN

QW remains constant and well defined, i.e. the GaN/AlN interfaces remain unchanged. However, the peak decreases in intensity with the annealing time, which implies a reduction of the number of free carriers in the QWs. Figure 5.4(c) presents room-temperature photovoltage response from structures annealed during different times. The pronounced asymmetric shape of the photovoltage curves is due to two resonance absorption mechanism between the e_1-e_2 transition and higher order transitions. When increasing the annealing time, the damping of the photovoltage response for e_1-e_2 transition occurs faster than for the high order transitions.

In conclusion, annealing Si-doped AlN/GaN SLs at 1000°C results in Si-interdiffusion, which is measured by a decrease of the ISB absorption and photovoltage. However, after 20 min annealing, there is no evidence of intermixing between the Al and Ga atoms.

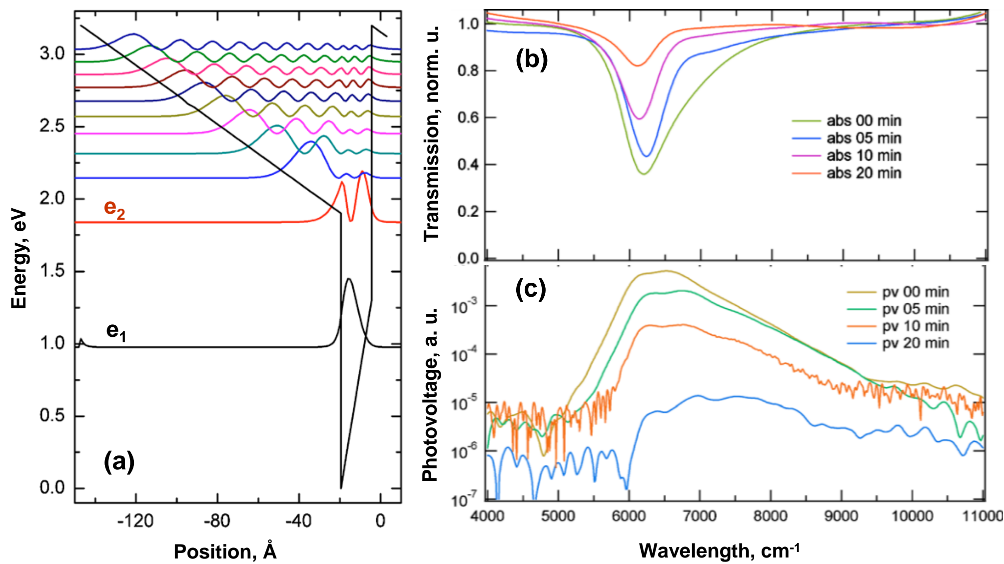

Figure 5.4. *(a) Simulation of the conduction band structure of GaN/AlN (3 nm/15 nm) SL using the 'calculeband' software. (b) FTIR spectroscopy and (c) room-temperature ISB photovoltage spectra from GaN/AlN (3 nm/15 nm) SL annealed during 0, 5, 10 and 20 min.*

5.3 Effect of Si on the interband optical properties

Figures 5.5(a), 5.6(a) and 5.7(a) present low-temperature PL spectra from series A, B and C described in Table 5.1 with various Si concentrations in the QWs. In Fig. 5.7(a), the peak at 349 nm is attributed to the $Al_{0.1}Ga_{0.9}N$ top buffer layer of series C. In all cases the PL emission peak blue shifts with increasing silicon concentration in

the QWs, shift that is accompanied by a broadening of the absorption line. Figs. 5.5(b), 5.6(b) and 5.7(b) present the peak energy position and PL line width versus free carrier concentration, showing the increase of the transition energy and full width at half maximum (FWHM) with increasing carrier concentration.

The magnitude of the blue shift cannot be explained only by the screening of the polarization-induced internal electric field in the QWs, which for instance predicts a maximum PL spectral shift for series C of smaller than 4 nm when increasing the doping concentration from $n = 10^{19}$ cm^{-3} to $n = 2\times10^{20}$ cm^{-3} (calculations performed using the nextnano^3 software). Indeed, for higher doping levels, the PL is strongly affected by band-filling effects, due to the shift of the Fermi level into the conduction band which gives rise to indirect optical transitions. This interpretation of the PL blue shift is in consonance with the broadening and asymmetry of the PL peak, with gradual intensity enhancement in the low energy side and sharper cut off at high energy, typical for momentum non-conserving transitions. This PL trend is consistent with the effect of doping on bulk GaN (Yoshikawa, 1999; Binet, 1999). For bulk GaN layers doped in the $<10^{19}$ cm^{-3} range, the emission first shifts to longer wavelengths, which is attributed to band gap renormalization due to Coulomb effects (Mahan, 1980), and then blue shifts due to band filling. In GaN/AlGaN QWs, the band gap renormalization is overwhelmed by the blue shift induced by screening of the polarization induced internal electric field and, for higher doping levels, by the band filling effect.

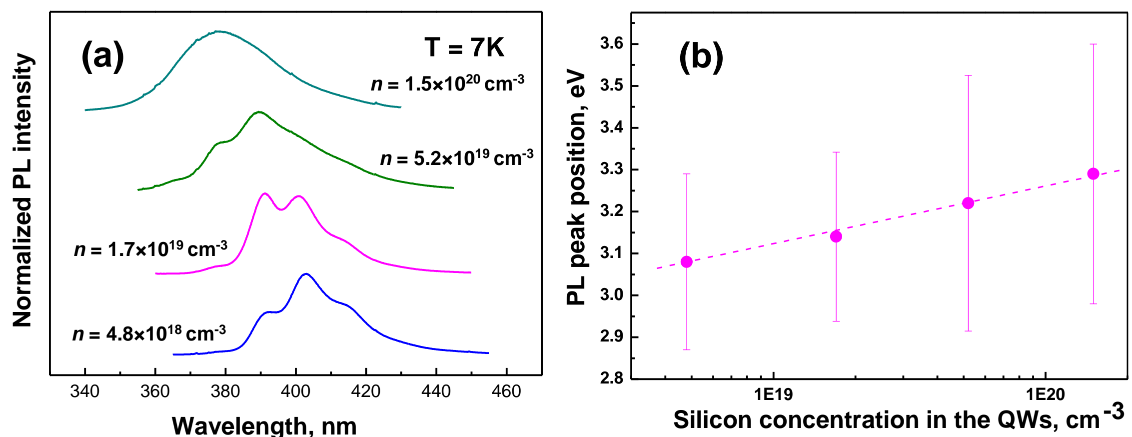

Figure 5.5. *(a) Low-temperature PL spectra from GaN / AlN (2 nm/3 nm) SLs of series A with different doping levels in the QWs. The data are vertically shifted for clarity. (b) Interband peak energy and FWHM (error bars) as a function of the silicon concentration in the QWs.*

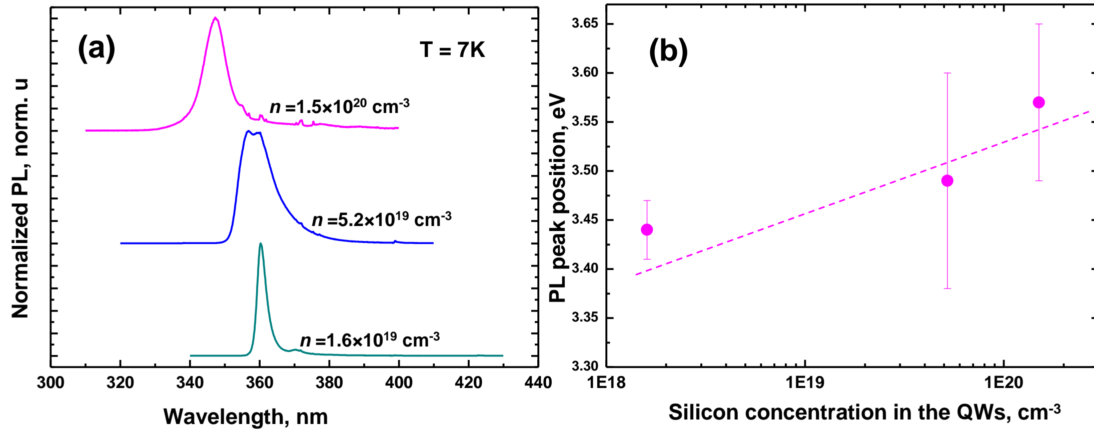

Figure 5.6. (a) Low-temperature PL spectra from GaN / $Al_{0.2}Ga_{0.8}N$ (4 nm/3 nm) SLs in series B. The data are vertically shifted for clarity. (b) Interband peak energy and FWHM (error bars) as a function of the silicon concentration in the QWs.

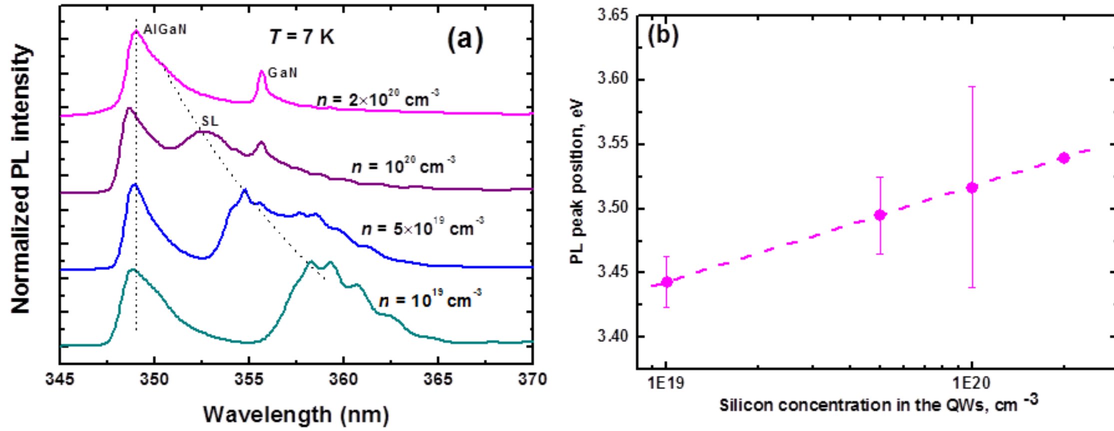

Figure 5.7. (a) Low-temperature PL spectra from GaN / $Al_{0.1}Ga_{0.9}N$ (7 nm/4 nm) SLs in series C. The data are vertically shifted for clarity. (b) Interband peak energy and FWHM (error bars) as a function of the silicon concentration in the QWs.

To confirm the involvement of band-filling effects, I have studied the low temperature (T = 7K) PL relaxation time in GaN:Si / $Al_{0.1}Ga_{0.9}N$ (7 nm/4 nm) SLs. I performed time-resolved photoluminescence (TRPL) measurements on samples of series C by exciting the samples with a femtosecond pulse and monitoring the decay of the photoluminescence. Results are presented in Fig. 5.8(a), which show nonexponential PL decays which slow down for higher doping levels, as the result of the nonvertical transitions involved in the case of band filling, described in Fig. 5.8(b).

This trend is opposite to the acceleration of the transition expected due to the screening of the internal electric field, which leads to an increase of the interband transition oscillator strength. Indeed, the presence of built-in electric fields in III-nitride semiconductor heterostructures induces a spatial separation of the electrons and

holes and results in a significant reduction in the wave function overlap and hence an increase of the carrier lifetime in comparison to the zero-field case. When introducing a large concentration of the silicon in the QW, the electric field can be partially screened, and therefore the carrier lifetime should decrease, in contradiction with the experimental results in Fig 5.8(a). The longer recombination time in heavily doped SLs confirms the dominating role of band filling effect, which is associated with longer recombination time for nonvertical transitions (Fig. 5.8(b)).

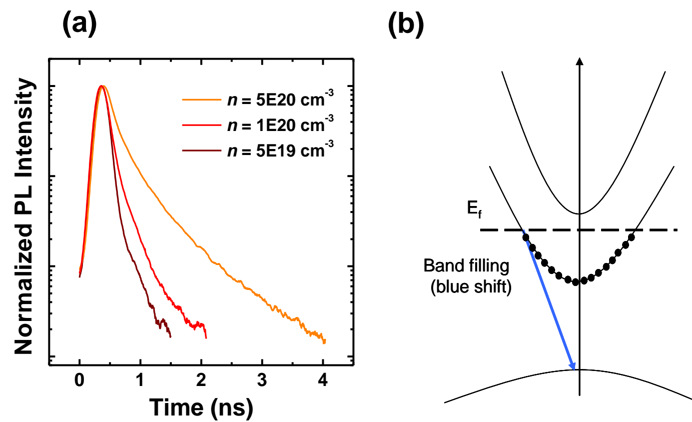

Figure 5.8. *(a) Time-resolved photoluminescence measurements of GaN / $Al_{0.1}Ga_{0.9}N$ (7 nm/4 nm) SLs grown on GaN-on-sapphire template with different doping levels. (b) Band diagram depicting the band filling effect.*

5.4 Effect of Si on the ISB optical properties

To analyze the effect of Si on the ISB optical properties, I performed IR absorption measurements by means of FTIR spectroscopy at room temperature. The ISB absorption spectra of series A for TM-polarized light is depicted in Fig. 5.9. It is important to notice that no absorption was detected for TE-polarized light, which confirms the ISB nature of the transitions.

Looking at the evolution of the ISB absorption peak energy, first it red shifts from 1.7 μm for [Si] = 1.8×10^{18} cm^{-3} to 1.8 μm when increasing Si concentration to 1.6×10^{19} cm^{-3}, probably due to the screening of the built-in electric field. Then, introducing higher silicon concentration leads to a blue shift of the ISB absorption peak due to the dominating the effect of the exchange over the Coulomb screening (Helman, 2003; Tchernycheva, 2006). Along with the spectral shift, we observe a

broadening of the absorption curves, whose relative spectral width, $\Delta\lambda/\lambda$, increases with higher doping level.

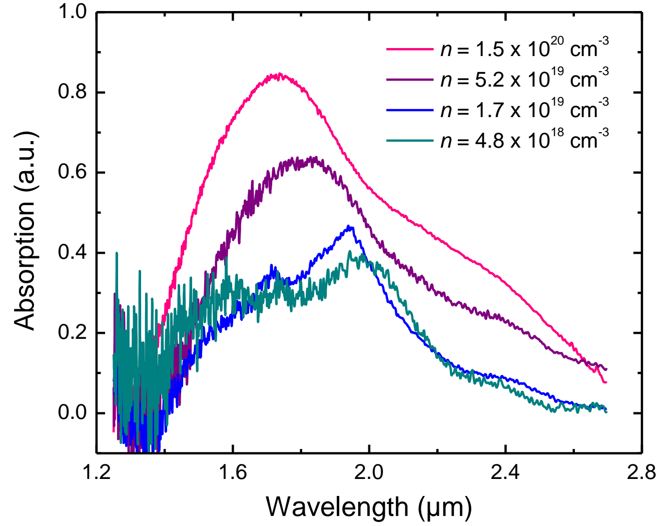

Figure 5.9. *Infrared absorption spectra for TM-polarized light measured from GaN / AlN (2 nm/3 nm) QWs of series A grown on GaN-on-sapphire templates.*

Figures 5.10(a) and (b) present TM-polarized ISB absorption of the series B and C, respectively, designed for mid-IR. In both cases the absorption peak shifts systematically towards shorter wavelength with increasing doping level. The FWHM is in the order of 60-250 meV for series B and C. In case of low Al content in the barriers, the built-in electric field is easily screened by small doping concentrations in the well; however, the screening of the internal electric field would lead to a red shift of the ISB transitions (Fig. 5.11(b)), which is opposite to observations. The discrepancy between simulations and experiments is mostly attributed to many-body effects, namely to the exchange interaction and depolarization shift (Fig. 5.11). It was previously shown that the dominant many-body effect in the case of GaN/AlN QWs absorbing in the near-IR is the exchange interaction, which lowers the ground-state subband energy (Tchernycheva, 2006; Helman, 2003). For QWs absorbing in the mid-infrared, the contribution of the depolarization shift, inversely proportional to the e_2-e_1 energy (Allen, 1976), becomes more important. The magnitude of the shift of ISB absorption in these mid-IR structures is comparable to the value of e_1-e_2, so that approximations that consider many-body effects as a perturbation of the Hartree-Fock equation (Bandara, 1988) are no longer valid, and a rigorous solution of Hartree-Fock equation is required.

On the other hand, the doping levels required to observe ISB transitions are relatively high in comparison to the density of states in the first electronic level of the QWs. For doping levels around 10^{20} cm^{-3}, the Fermi level approaches the second electronic levels, and thus a contribution of the e_2-e_3 transition, located at slightly higher energy than e_1-e_2, might also be present in the IR absorption spectra.

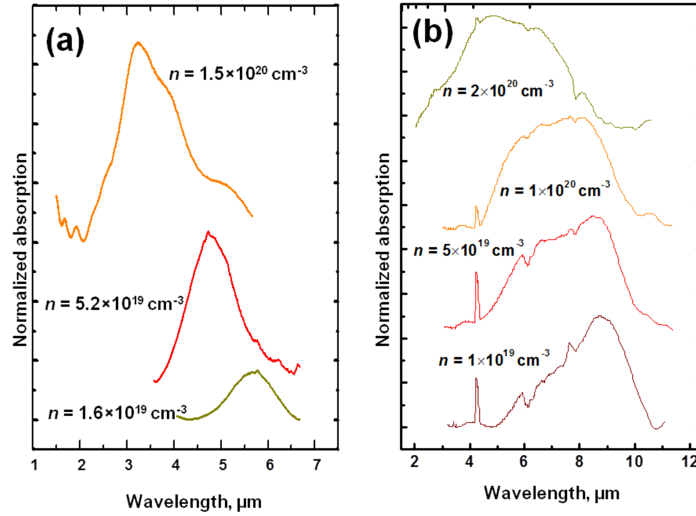

Figure 5.10. *Infrared absorption spectra for TM-polarized light measured from (a) GaN / $Al_{0.2}Ga_{0.8}N$ (4 nm/3 nm) QWs of series B and (b) GaN / $Al_{0.1}Ga_{0.9}N$ (7 nm/4 nm) QWs of series C (Measurements (a) and (b) performed at CEA/INAC, Grenoble and at the University Paris-Sud, respectively).*

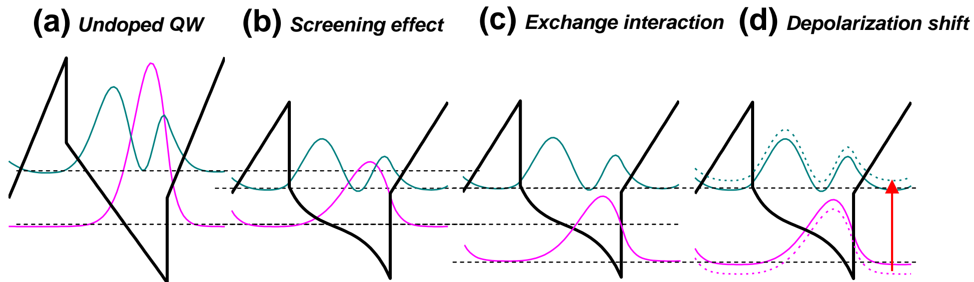

Figure 5.11. *Schematic descriptions of many-body effecs on the ISB transitions in GaN/$Al_xGa_{1-x}N$ SLs: (a) undoped QW; (b) Screening effect; (c) Exchange interaction; (d) Depolarization shift.*

Li *et al*. (2005) have quantatively estimated many-body effects in GaN/AlGaN QWs with low Al content in the barrier. The calculations predicted final blue shift of the ISB absorption revealing exciton-like and direct Coulomb interaction red shifts to be negligible compared to depolarization shift and electron-electron exchange interactions. After accounting for many-body effect the calculation showed a good correlation with the experimental ISB absorbance spectra.

5.5 Conclusions

We have studied effect of silicon doping of GaN QWs on the optical properties of GaN/Al(Ga)N SLs designed to exhibit ISB absorption in near- and mid-IR spectral region. Plasma-assisted MBE permits a good localization and accuracy of silicon doping in GaN QWs during epitaxial deposition, which was confirmed by SIMS measurements. The relatively low growth temperature of SLs is about ≈720°C prevents silicon diffusion from GaN to adjacent layers, which is however observed when annealing the samples at 1000°C in the timescale of minutes.

The doping level in GaN/Al(Ga)N SLs has an influence on both interband and intraband transitions. The increase of Si concentration in the QWs leads to a blue shift of the photoluminescence spectra associated to band-filling effects. In terms of ISB characterization, with increasing doping levels we observe a large broadening of the ISB absorption line width accompanied by a significant blue shift, which results in a considerable discrepancy between 8-band k•p Schrödinger-Poisson calculations and the measured wavelength of intraband transition. The two-level single particle approach is hence inapplicable for the ISB structures targeting the mid-IR spectral range, and the design requires accounting for many-body effects, namely for exchange interaction and depolarization shift.

Chapter 6

Near- and mid-IR quantum cascade detectors

This chapter will be devoted to quantum cascade detectors (QCDs) based on GaN/Al(Ga)N SLs for operation at fiber-optic telecommunication wavelengths (1.5 μm) and for the mid-IR spectral range. I will start with the short introduction to working principle of QCDs, proceed with the presentation of the design and band profile modeling, which takes advantage of internal field inherent to III-nitride materials. The structural and optical investigation of the grown prototypes will be presented. The effect of the doping level on the QCD performance will be discussed.

6.1 Quantum Cascade Detector: Motivation and working principle

The most common design of ISB detector is the quantum well infrared photodetector (QWIP), which is a photoconductive ISB device where the change of the structure resistance under IR illumination is detected by applying external bias (Levin, 1993). The active region of a QWIP consists of a SL with relatively thick barriers, which prevents coupling of the electron confinement states of neighboring QWs and reduces the dark current. The dark current gives rise to the detector noise and defines operating temperature of the device. Photoexcited electrons contribute to the 3D current in the continuum above the barriers (Fig. 6.1). To provide good carrier extraction the QW thickness and conduction band offset are chosen to place the upper electron state close to the barrier conduction band edge.

Nowadays, QWIPs based on GaAs material are highly performance technology for thermal IR imaging, with excellent uniformity and stability properties. However, excessive dark current of QWIPs is the major drawback of these photodetectors.

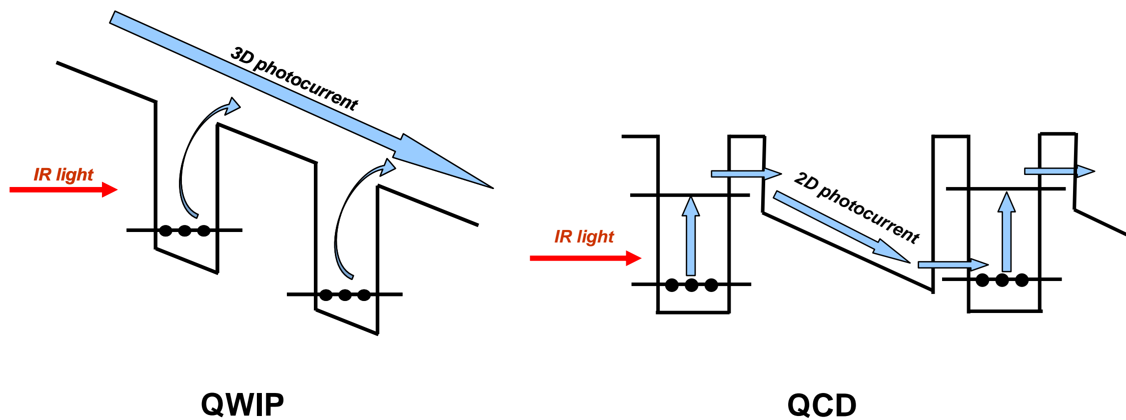

Figure 6.1. *Schematic conduction band diagrams of QWIP (left) and QCD (right).*

The obstacles arising in QWIP technologies can be conquered using photovoltaic devices. In this type of photodetectors, the detection of the IR illumination occurs without any external bias. The relocation of the charge under IR illumination induces a measurable electric field through the entire structure, which can be measured as a photocurrent in the external circuit. In contrast to the photoconductive devices; only effective current due to the IR illumination is present in the photovoltaic detectors. The absence of the dark current permit increase operating temperature of the photovoltaic detector.

In the case of As-based material systems the photovoltaic devices are fabricated by breaking the symmetry of the wave functions in heterostructure, i.e. by growing step QW (Fig. 6.2(a)), coupled QWs (Fig. 6.2(b)), asymmetric barrier etc. In the case of III-nitrides, the asymmetry is spontaneously introduced by the polarization (Hofstetter, 2006).

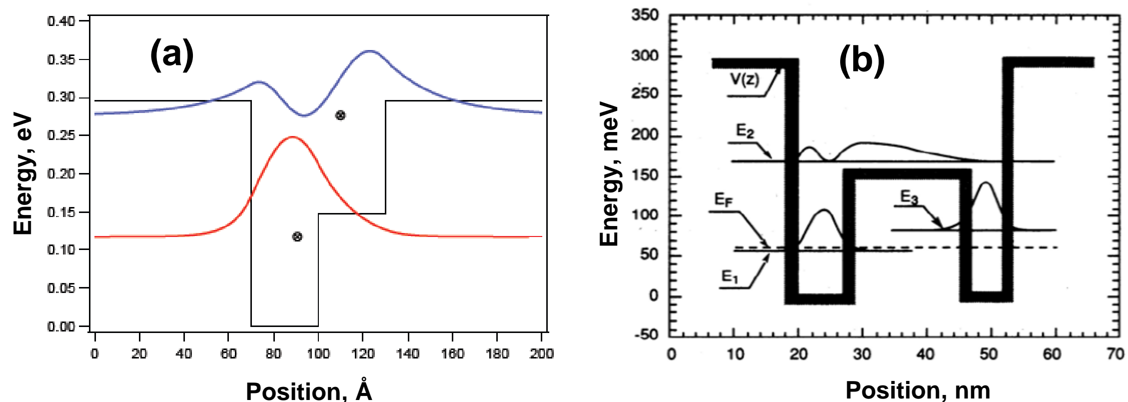

Figure 6.2. *Asymmetric wave functions and conduction band profiles of step QW (a) and (b) coupled QWs.*

The quantum cascade detector (QCD) is an advanced photovoltaic QWIP where the charge separation is enhanced via a quantum cascade. It was first demonstrated at the Univ. of Neuchâtel in the group of D. Hofstetter (Hofstetter, 2002). Compared to QWIPs, QCDs are less mature technology (Gendron, 2004). A main advantage is the suppression of the dark current thanks to the operation at zero-bias, with the subsequent improvements in signal-to-noise ratio and maximum working temperature.

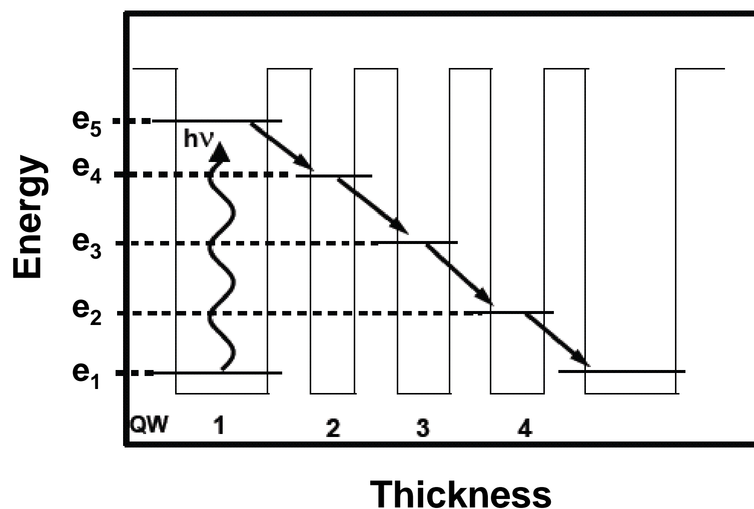

Figure 6.3. *Schematic conduction band of QCD explaing detection mechanism.*

Figure 6.3 presents conduction band profile of one period of QCD. It consists of an active degenerately-doped QW with two confined states, where electrons are photoexcited from the ground to the upper state under illumination (states e_1 and e_5 in Fig. 6.3). The e_1-e_5 energy separation defines the maximum of the spectral response of the device. Under IR illumination the carriers in active QW transferred to the e_5 level. Excited electrons can experience two relaxation processes: scattering back to the ground state and tunneling to the extractor region. Due to strong coupling between QWs 1 and 2 electrons tunnel to level e_4 via electron-phonon interaction, then to adjacent QW 3 and so on until they reach e_1 level of the next active region. Therefore, carriers absorbing photons and undergoing the relaxation process travel through the entire cascade structures and induce voltage due to charge replacement. In general, the extractor region is designed to have difference between ground states of two adjacent QWs equal to the LO phonon energy, in order to achieve efficient phonon-assisted extraction. This type of photovoltaic detectors shows good quantum efficiency due to

strong oscillator force between e_1-e_5 and cascade structure with optimized matrix elements of the confinement energy levels between adjacent QW.

The conventional parameter for characterization of the performance of a photodetector is the ratio between peak responsivity R_p and mean noise current i_n normalized by the detector area A and measurement bandwidth Δf, which is called normalized detectivity:

$$D^* = R_p / i_n \sqrt{A \Delta f} \quad [6.1]$$

The detection of IR light is accompanied by noise which has components with different origin. The noise can be caused by detector itself, by the operating circuit or it may come from the radiation background. In general, at high temperature it is the background fluctuations that, dominating over other types of noises, limit the performance of QCD. This effect is called background-limited infrared photodetection (BLIP). For the QCD, the operation performance below so-called T_{BLIP} is dominated by the Johnson noise, which is independent of the temperature.

6.2 QCD for fiber optics telecommunication

The large conduction band offset between GaN and AlN opens the possibility to realize QCDs in the near-IR spectral range. However, given the uncertainties and particularities in III-nitride material properties, modeling the QCD band structure for short wavelengths is a challenging task; even more as the required thickness of active QW is only a few (4-6) monolayers, which is close to the limits of conventional simulation models. Moreover, a small change of the polarization-induced electric field, for example due to partial relaxation or fluctuation of the layer thickness in real structures (Tchernycheva, 2010), results in a shift of the electron eigenenergies between active and extractor QWs, which deteriorates the detector responsivity. It can as well introduce misalignment in extractor LO-phonon ladder and diminish extraction efficiency of electrons. Therefore the simulations can be used as a guide and not as a perfect tool for the definition of the operating wavelength.

In the case of GaN-based QCD, the strong electron–LO-phonon interaction leads to extremely short relaxation time of about 150-400 fs (Iizuka, 2006), which results in

a high-speed operation of the detector. Usually, the active region is sandwiched between $Al_xGa_{1-x}N$ contact cladding layers with Al mole fraction and doping level chosen in such a way that it prevents depletion of the active QWs due to the difference in spontaneous and piezoelectric polarization between the active region and the claddings.

Fig. 6.4 shows the band profile of a near-IR QCD designed to have absorption at fiber-optic telecommunication wavelength. This structure was proposed by S. Sakr at the University Paris-Sud. The simulations were performed using the Schrödinger-Poisson nextnano^3 solver. For the modeling we assume that the structure is fully strained on AlN. The active 1.5-nm-thick GaN QW doped with [Si] = 5×10^{19} cm^{-3} and contain two electron confinement states to exhibit ISB absorption at 1.5 µm. The active QW separated from the extractor by 1-nm-thick AlN barriers. The electron extraction occurs via a 4 period SL which consists of 1-nm-thick $Al_{0.3}Ga_{0.7}N$ QWs with 1.5-nm-thick AlN barriers.

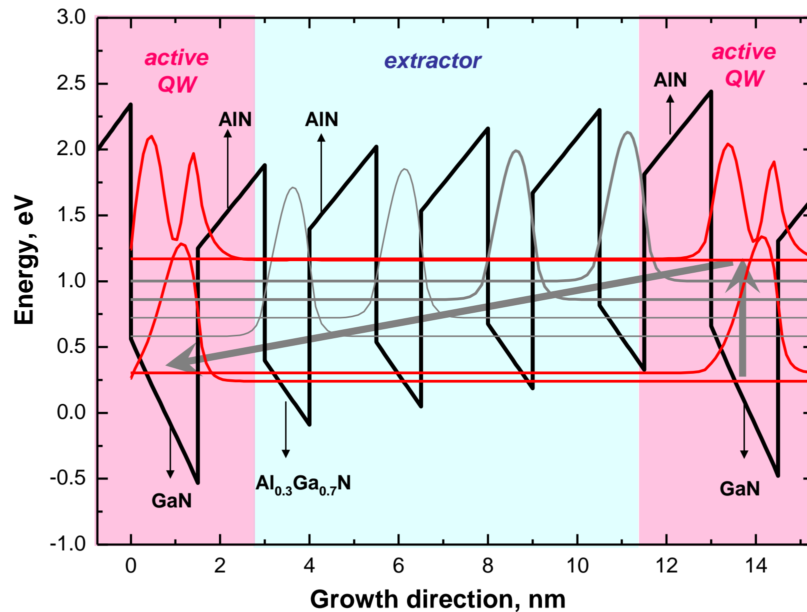

Figure 6.4. *Conduction band profile of a QCD designed for fiber-optic telecommunication wavelength.*

Electrons in the active QWs are excited by external IR illumination from ground to the first excited level, and the tunnel resonantly to the extractor where they relax towards the ground state of the following active QW.

The QCD heterostructure was grown by plasma-assisted MBE on an AlN-on-sapphire template under Ga-rich growth conditions. Low growth temperature (~720°C) results in sharp interfaces between GaN and AlN layers which is crucial for the devices operation at 1.5 μm. The 40 period active region is sandwiched between $Al_{0.3}Ga_{0.7}N$ top and bottom cladding layers doped with [Si] = 1×10^{19} cm^{-3}.

Figure 6.5 presents *θ-2θ* scan of the (0002) x-ray reflection of the QCD heterostructure measured in HR conditions. Several satellite reflections of the cascade structure are present in the *θ-2θ* curve which confirms good periodicity of the heterostructure. Two closely placed reflections peaked at $2\theta \approx 35{,}9^{o}$ are associated to the bottom and top $Al_{0.3}Ga_{0.7}N$ cladding layers. The difference of the interplane distances of the claddings is explained by the different strain state of the epilayers.

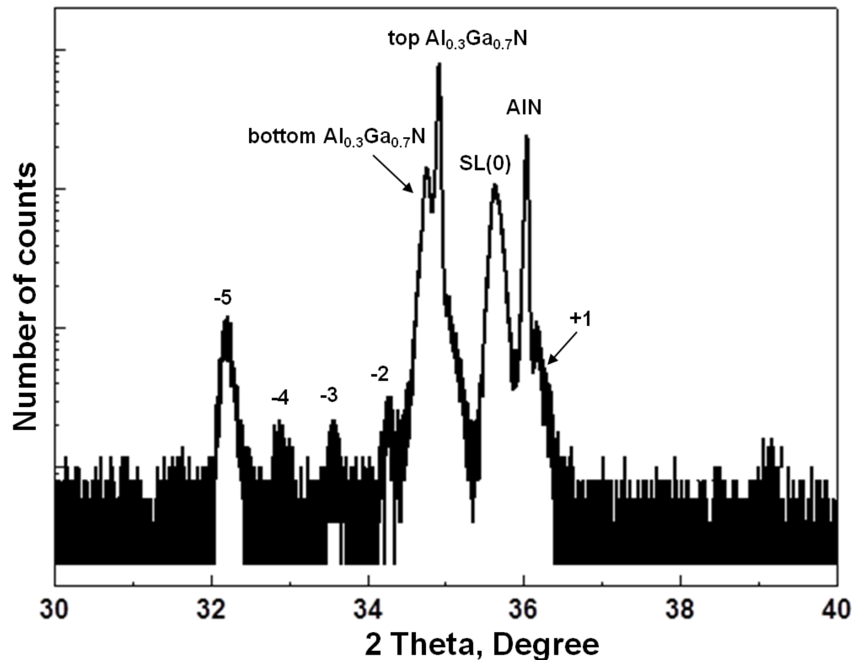

Figure 6.5. *X-ray Θ-2Θ scan of the (0002) reflection (black) for the QCD (E2236).*

The structural quality of the sample was analyzed by TEM technique (Fig. 6.6). The structure has abrupt interfaces and good reproducibility of the layer thicknesses. The well and the barrier layers in the extractor are deduced to be 1 ± 0.15 nm and 1.5 ± 0.15 nm, respectively, and the active QW thickness is 1.6 ± 0.26 nm. Stacking faults were not observed in the HRTEM images, however, the structure reveals relaxation via formation of inclined threading dislocations, indicated by arrows in Fig. 6.6(b) as previously observed in GaN/AlN SLs (Kandaswamy, 2009).

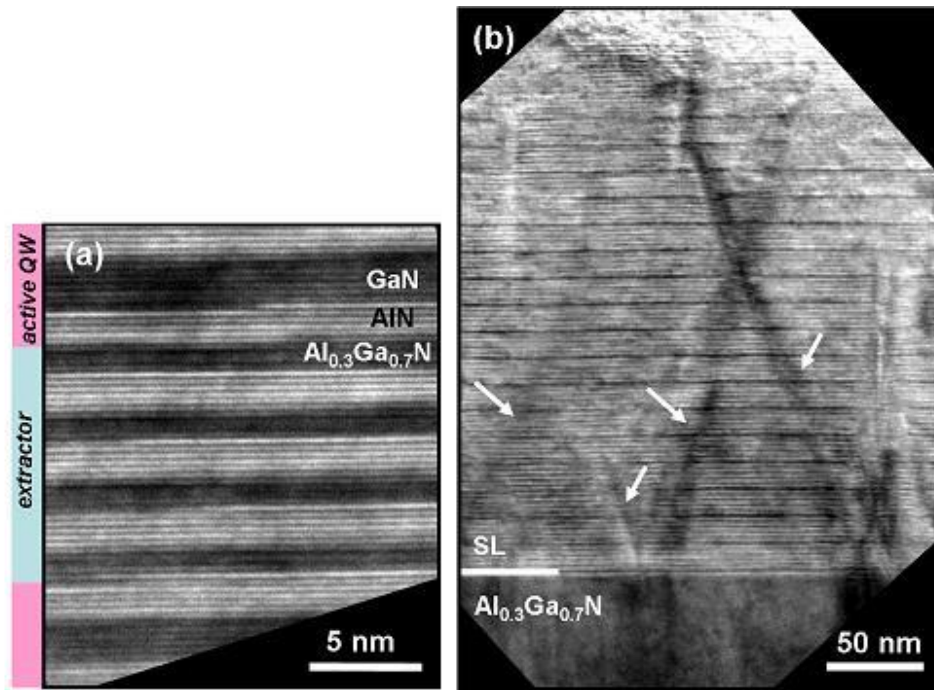

Figure 6.6. *(a) High-resolution TEM image and (b) two-beam TEM image of QCD designed for fiber-optic telecommunication wavelength viewed along the <1-100> zone axis with diffraction vector g = (11-20). White arrows indicate inclined threading dislocations.(Sample E2236)* (TEM observations performed at Grenoble-INP by Dr. E. Sarigiannidou).

The transmission and photovoltage (PV) measurements were performed at the University Paris-Sud by the group of Prof. F. H. Julien. The ISB transitions in the QCD structure were measured by FTIR spectrometer. The sample was mechanically polished into a multipass waveguide with 45° facets. Then, QCD devices have been processed in the form of square mesas with a size of 700 × 700 μm^2 using an inductive coupled plasma reactive ion dry etching. Ti/Al/Ti/Au metals were deposited to form the top and bottom contacts. The center of the top contact was left unmetallised to allow direct illumination of the semiconductor surface.

Fig. 6.7 presents transmission measurements superimposed over the PV response. Both curves display two clearly resolved peaks at 1.42 µm and 1.50 µm with a FWHM of 120 meV. The correlation between transmission and photoresponse behavior is a proof that the ISB mechanism is responsible for the observed PV peaks.

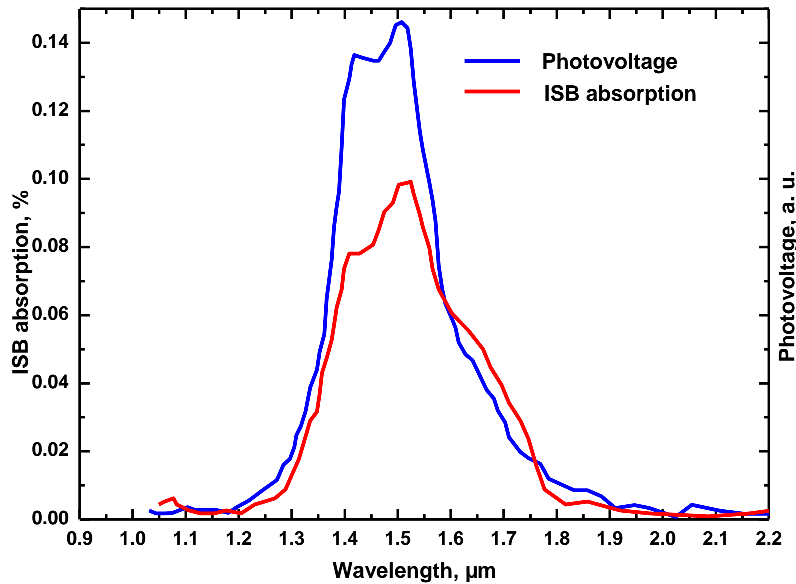

Figure 6.7. *Photovoltage (blue curve) and ISB absorption (red curve) spectra at room temperature for TM-polarized light measured from QCD designed for fiber-optic telecommunication wavelength (Measurements were performed at Technion, Israel).*

The responsivity has been measured using a Photonic Tunics source at 1.55 µm wavelength amplified by an erbium-doped fiber amplifier. The QCD was illuminated by the collimated light exiting the fiber at 45° angle of incidence. The peak responsivity corrected for the beam intensity profile and the surface of the detector is estimated to be 15 V/W at room temperature for TM-polarized light and 6 mA/W on a 50 Ω resistor.

6.3 QCDs for the 3-5 µm spectral range

In order to tune the operation to the longer wavelength, two types of QCD structures were designed by S. Sakr at the University Paris-Sud (Fig. 6.8). The active region of both samples consists of GaN/$Al_xGa_{1-x}N$ SLs with silicon doped 3-nm-thick active QW, 1.5-nm-thick $Al_{0.35}Ga_{0.65}N$ and 1-nm-thick $Al_{0.65}Ga_{0.35}N$ barriers for structures of type *A* and *B*, respectively. The thickness of the QWs in extractor region is 1 nm. The QCD heterostructures are sandwiched between $Al_xGa_{1-x}N$ silicon doped 700-nm-thick bottom and 100-nm-thick top layers. The Al mole fraction and doping level of the contact layers are chosen in such a way which prevents band bending and keeps ground state of the active QWs populated with electrons.

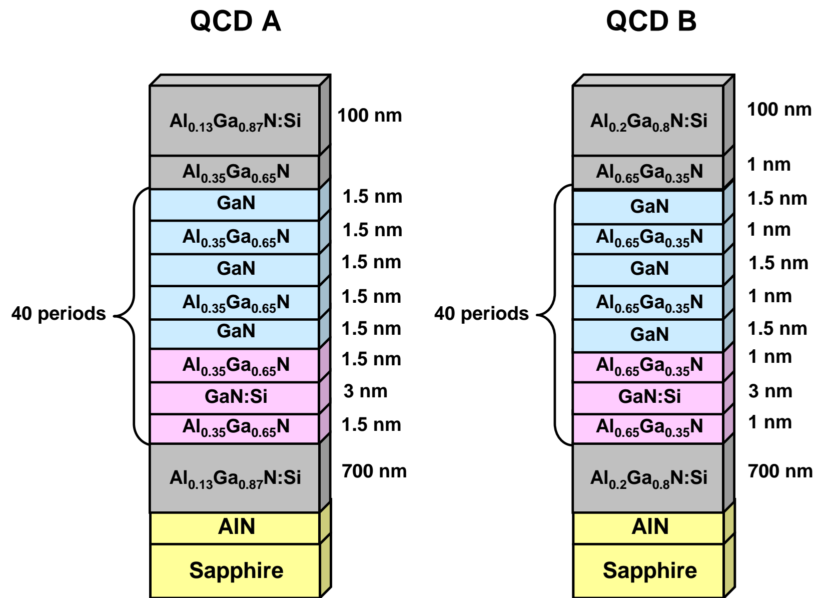

Figure 6.8. *Schematic sample structures of two types of QCDs for operation in 3-5 μm spectral range.*

Figure 6.9 and Figure 6.10 present nextnano[3] calculations of the conduction band profile which predicts ISB absorption in the active QWs at 4 μm and 3.3 μm for QCD of types *A* and *B*, respectively. The simulated structures are assumed to be fully strained on AlN. The energy separation between the ground states of the extractor adjacent QWs is close to the LO-phonon energy, which provides fast relaxation of electrons from excited state in one active QW to the ground state of active QW in the next period.

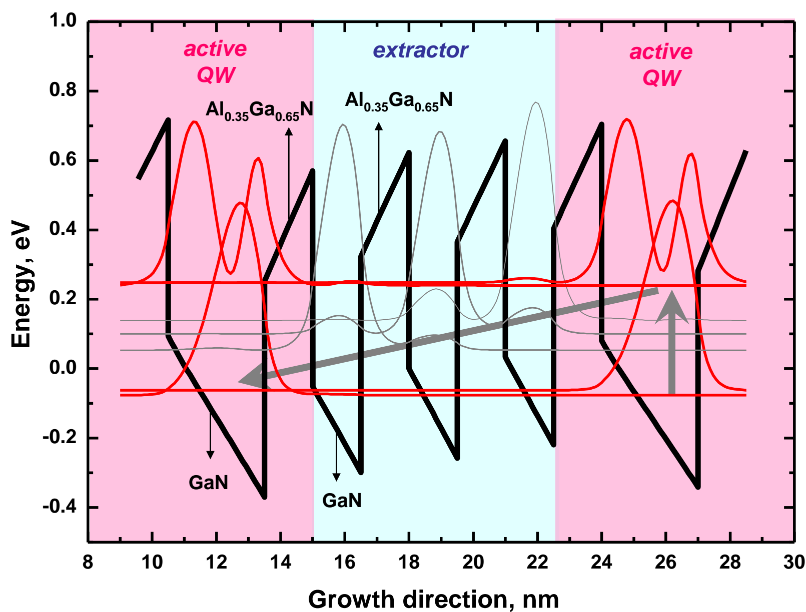

Figure 6.9. *Conduction band profile of QCD A.*

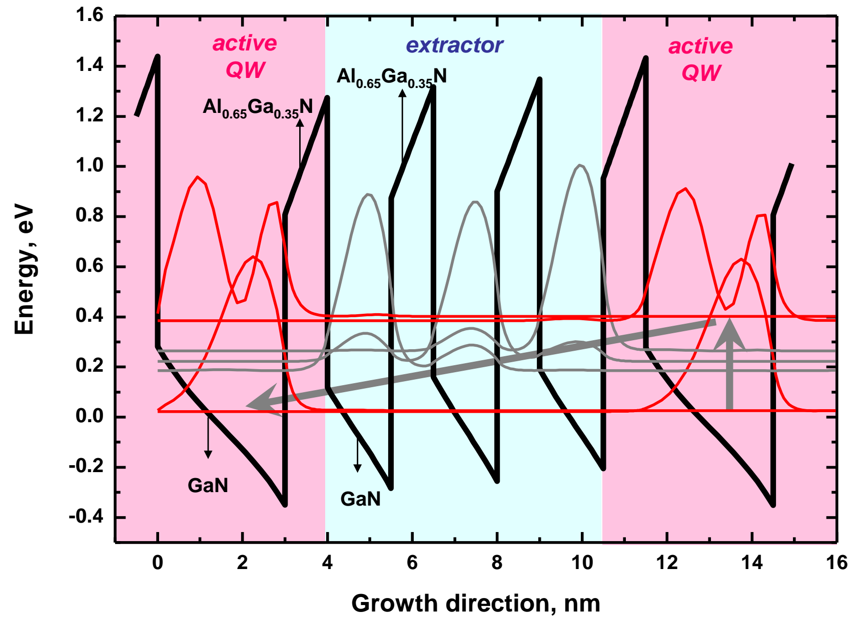

Figure 6.10. *Conduction band profile of QCD B.*

In order to study and identify the optimal carrier concentration in the detector structure I have synthesized the series of QCDs varying silicon doping level in active QWs (Table 6.1). QCD structures were grown by plasma-assisted MBE under Ga-rich conditions on AlN-on-sapphire templates. The growth was performed at reduced substrate temperature of about 700°C in order to prevent intermixing between GaN and AlGaN layers. The calibration of the required Al mole fraction for the AlGaN barrier growth was made using RHEED intensity oscillations during AlN deposition under Al-limited conditions. Figure 6.11 presents typical AFM surface images of QCD *A* and *B*. The samples present atomic terraces and hillocks inherent to PAMBE growth method. The RMS roughness for both structures does not exceed 5 nm in large area scan up to 20×20 μm^2. The growth under compressive strain (on AlN-on-sapphire templates) prevents crack formation in the layers. However, some nanocracks (Fig. 6.11) were observed in the top $Al_xGa_{1-x}N$ layers which might be indication of insufficient Ga excess during the growth.

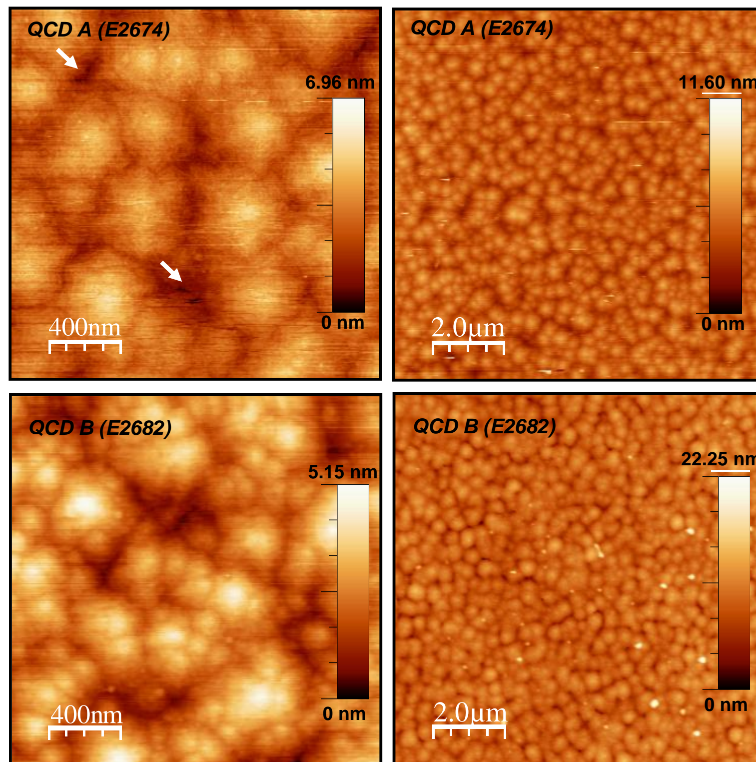

Figure 6.11. *AFM surface images of QCD A and B. White arrows indicate microcracks presented on the surface of top $Al_xGa_{1-x}N$ contact layer.*

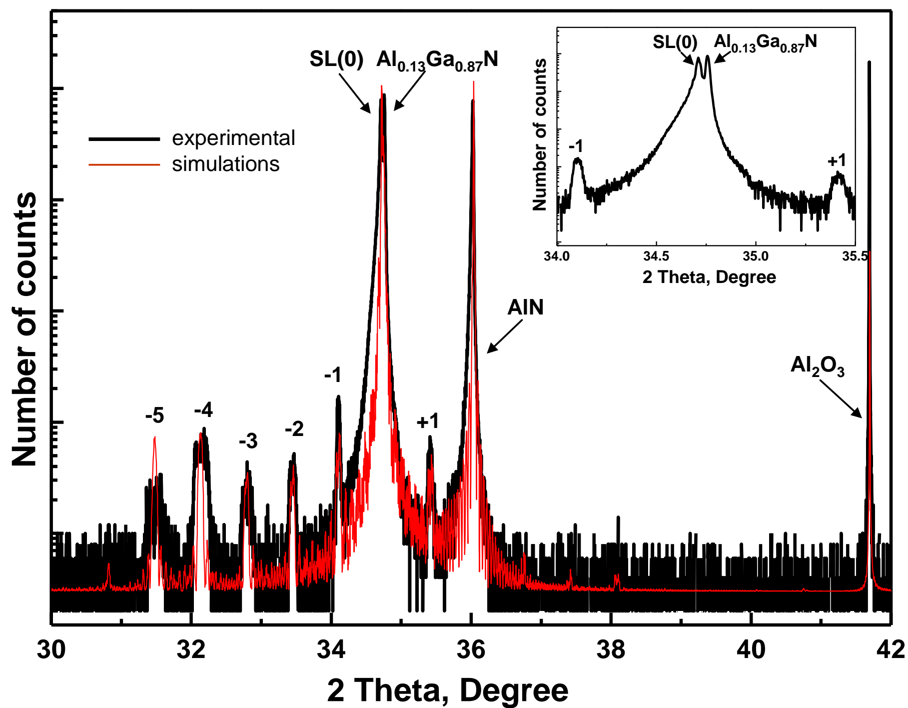

Figure 6.12. *X-ray Θ-2Θ scan of the (0002) reflection (black) for the QCD A (E2674). The insert is the zoom of the scan for the SL and buffer layers peaks. The superimposed thinner simulations (red) were performed using the program X'Pert Epitaxy 4.0 from Phillips Analytical.*

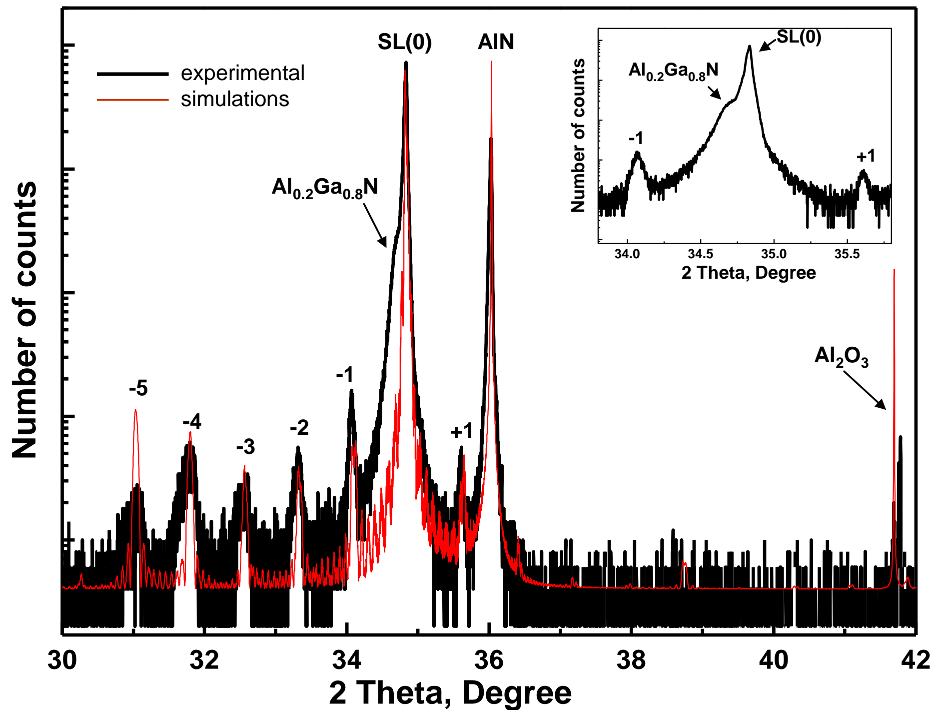

Figure 6.13. *X-ray Θ-2Θ scan of the (0002) reflection (black) for the QCD B (E2682). The insert is the zoom of the superimposed SL and buffer layers peaks. The superimposed thinner simulations (red) were performed using the program X'Pert Epitaxy 4.0 from Phillips Analytical.*

Fig. 6.12 and 6.13 present θ-2θ scans of the (0002) x-ray reflection of the QCD heterostructures A and B, respectively, measured in HR conditions. Several satellite reflections of the cascade structure are present in the θ-2θ curve which confirms good periodicity of the heterostructure. The proximity of the main SL and the buffer peaks confirms similar strain state of the whole structure wich result in reducided density of dislocation in active region.

TEM observations were made at Grenoble-INP by Dr. E. Sarigiannidou. The images of the QCD A structure with 35% Al mole fraction in the barriers reveals a good quality of the layers with some threading dislocation (indicated by white arrows in Fig. 6.14 (b)) and rare basal stacking faults (indicated by red arrows in Fig. 6.14(b)). In contrast, the QCD B structure with 65% Al mole fraction in the barriers had a higher density of basal stacking faults and similar density of threading dislocations. The samples present a good control over the layer thicknesses. The interfaces in a structure with lower Al content in the barriers (QCD A) reveals more abrupt and well defined interfaces in comparison with structure with higher Al mole fraction in the barriers.

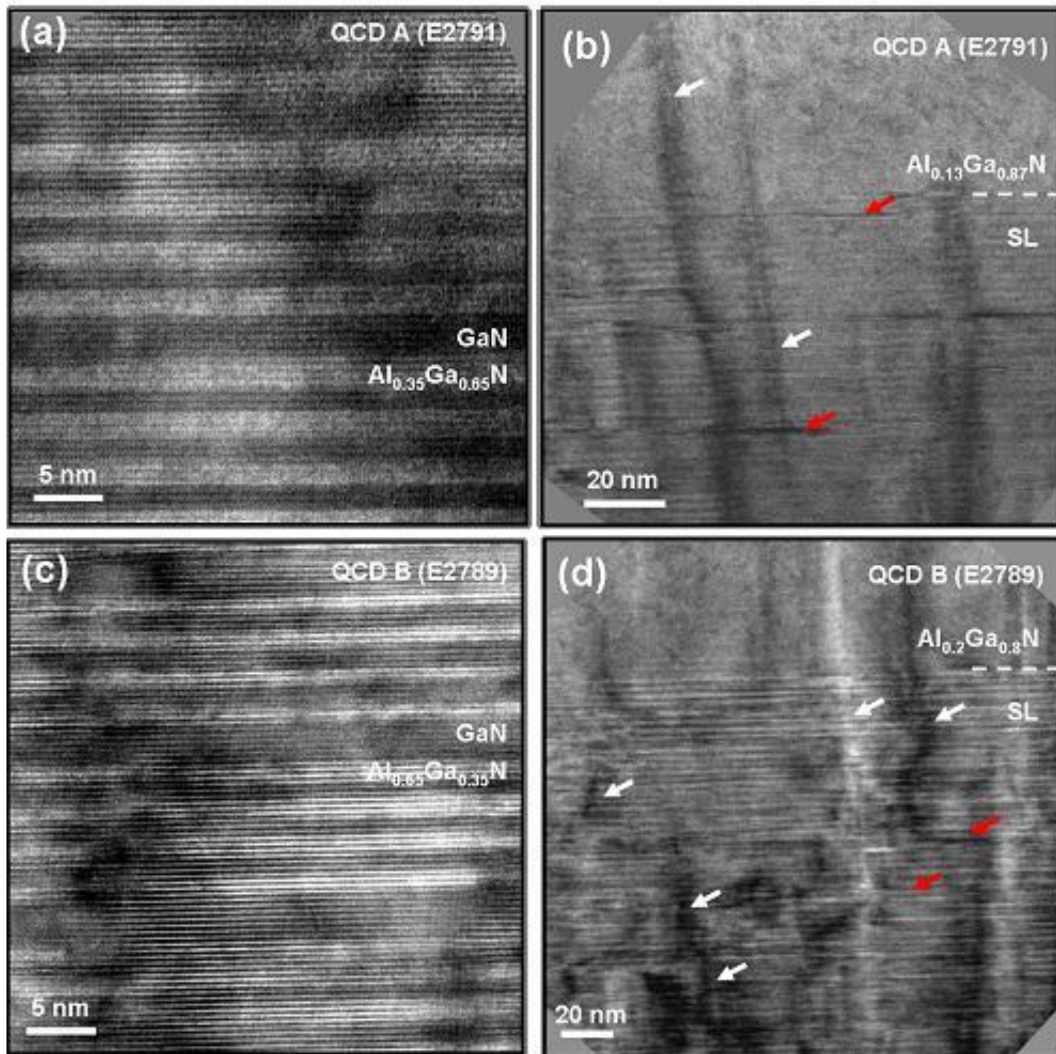

Figure 6.14. *(a,c) High-resolution TEM images and (b,d) two-beam TEM images of QCD A (a,b) and QCD B (c,d) viewed along the <1-100> zone axis with diffraction vector g = (11-20).White and red arrows are indications of the threading dislocations and basal stacking faults, respectively. The boundaries between cascade heterostructure and top AlGaN capping layers are indicated by dashed white lines* (TEM observations performed at Grenoble-INP by Dr. E. Sarigiannidou).

In order to identify the optimum doping level to obtain a measurable ISB absorption while keeping a resistive enough active region, I have grown several QCD structures following the above-described designs with different silicon concentration in the active QWs. The QCD structures of type A and B that has been grown varying the temperature of silicon effusion cell. Grown QCD structures and corresponding temperatures of the silicon cell (silicon concentration) are presented in Table 6.1.

Table 6.1. *FTIR spectroscopy and photovoltage response measured from series of QCDs of type A and B.*

Sample	Structure type	Temperature of Si cell (concentration), °C (cm^{-3})	ISB absorption energy (wavelength), eV (μm)	Energy (wavelength) of photovoltage response, eV (μm)
E2674		1200 (1.7×10^{19})	0.299 (4.15)	4.3
E2886	A	1220 (2.7×10^{19})	0.313 (3.96)	no signal
E2836		1230 (3.5×10^{19})	0.326 (3.8)	no signal
E2739		1250 (5.2×10^{19})	0.332 (3.74)	no signal
E2791		1270 (8.2×10^{19})	0.354 (3.5)	no signal
E2729		1300 (1.5×10^{20})	0.417 (2.97)	no signal
E2682		1200 (1.7×10^{19})	no absorption	3.4
E2845	B	1230 (3.5×10^{19})	0.382 (3.25)	no signal
E2789		1270 (8.2×10^{19})	0.405(3.06)	no signal

The ISB absorption spectra measured by FTIR spectrometer at room temperature are presented in Figs. 6.15 and 6.16 for QCD *A* and *B*, respectively. The lower limit for absorption is higher for the structure B. It might be associated with poor quality of the sample and treading dislocations which behaves as acceptor center along the dislocation lines and capture electrons leading to enhanced of minimal doping (Iizuka, 2006). Like in the case of simple GaN/Al(Ga)N SLs, when introducing higher silicon concentration into the active QWs the ISB absorption peak blue shifts for both QCDs *A* and *B*. When increasing the silicon concentration in the QWs of the QCD A structure from [Si] = 1.7×10^{19} cm^{-3} to 1.5×10^{20} cm^{-3} the ISB absorption peak blue shifts by ≈ 1.5 μm.

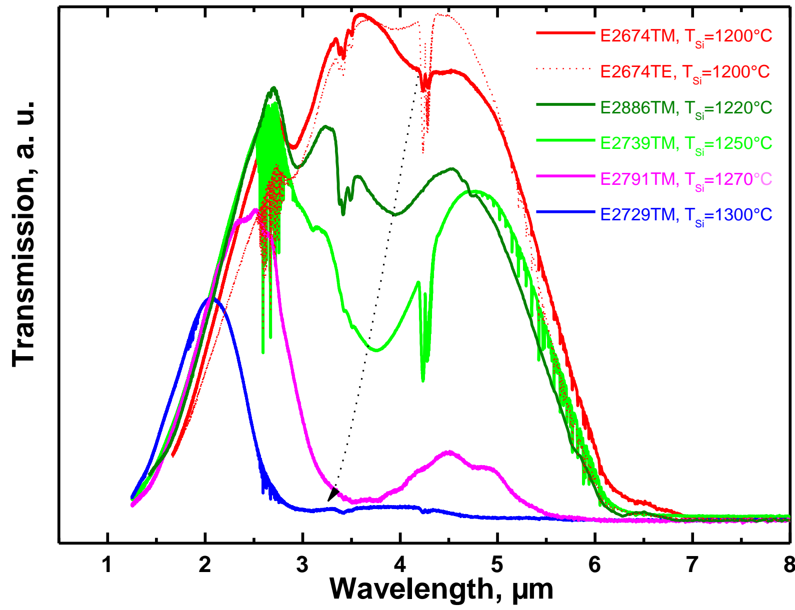

Figure 6.15. *Infrared ISB absorption spectra for TM- (solid curves) and TE-polarized (dotted curve) light from QCD A with different doping levels in active QWs (Measurements were performed at INAC, Grenoble).*

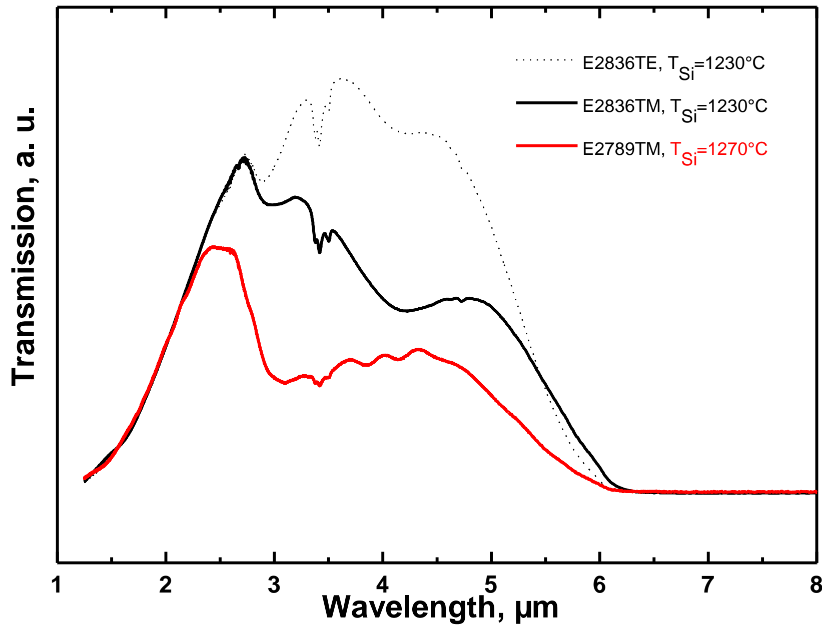

Figure 6.16. *Infrared transmission spectra for TM- (solide curves) and TE-polarized (dotted curve) light from QCD B (*E2789 *with silicon concentration in active QWs of about* 8.2×10^{19} cm^{-3} *(Measurements were performed at INAC, Grenoble).*

The samples were processed into 200×200 μm^2 devices at Technion (Israel) in the group of G. Bahir. Mesa etching was performed using standard inductively coupled plasma (ICP) etching. Ohmic contacts were fabricated by the deposition of

Ti/Al/Ti/Au on the top and bottom $Al_xGa_{1-x}N$ layers. The photovoltaic response was detected only for the sample A and B with low silicon doping in QWs of $[Si] = 1.7\times10^{19}$ cm^{-3}.

Figure 6.17 shows PV measurements of sample E2674. A clear response of the detector at zero bias is observed at ≈ 4.3 μm, in good correlation with the absorption results. However, the signal is present only at low temperatures up to 80 K and it deteriorates with the time of work. The peak responsivity of the detector at 14 K is estimated to be R = 0.5 mA/W for TM-polarized light and Jonhnson noise limited detectivity $D^* = 2 \times 10^{11}$ Jones.

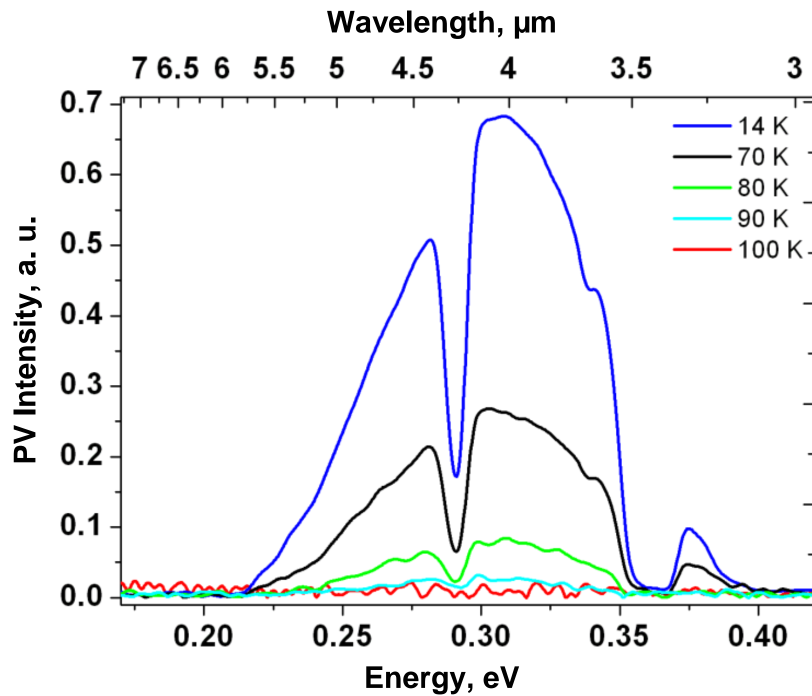

Figure 6.17. *Photovoltage response at deferent temperatures for TM-polarized light measured from QCD A (Measurements were performed at Technion, Israel).*

The PV measurement at 14 K for TM-polarized light of QCD structure *B* is presented in Fig. 6.18. The photoresponse peaks at 3.4 μm, which corresponds to the ISB absorption data. A weaker reproducible peak at 1.5 μm was observed in the spectra, but its origin is not clear.

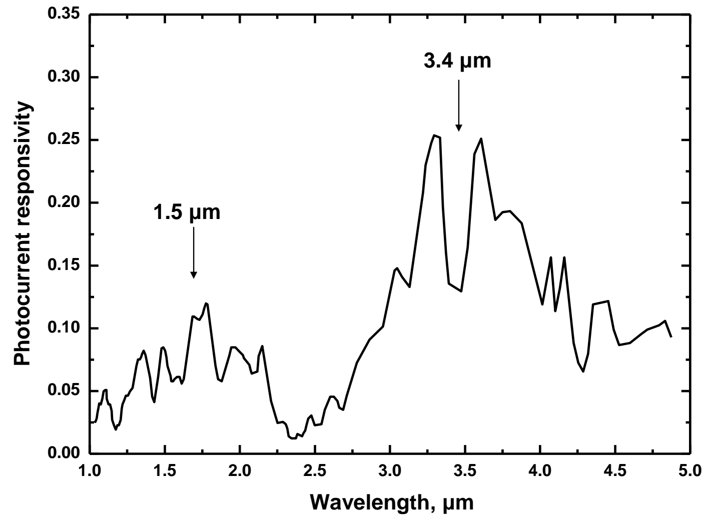

Figure 6.18. *Photocurrent responsivity at 14 K for TM-polarized light measured from QCD B (Measurements were performed at Technion, Israel).*

It is important to notice that electrical signal from the QCD structures was observed in the case when resistance of active medium was ≈ 10^3 larger than the one of the Ohmic contacts. The specific contact resistance of these samples was found to be on the order of 10^5 Ω at 14K compared to the resistance of the active region on the order of 10^8 Ω at 14K. This confirms the minor effect of the contacts on the electrical measurement.

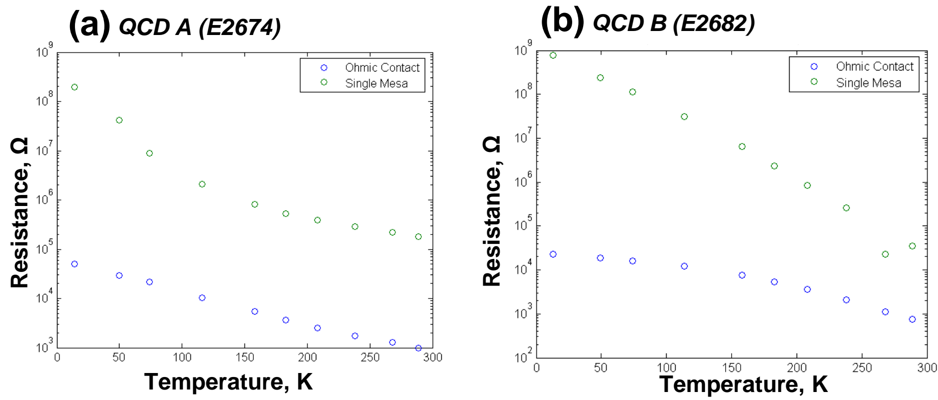

Figure 6.19. *Resistance of the contacts and of the mesa heterostructures for (a) QCD A (E2674) and (b) QCD B (E2682) (Measurements were performed at Technion, Israel).*

Figure 6.20 presents current-voltage (*I*-*V*) characteristics and differential resistance (R_{diff} = d*V*/d*I*) calculated from the experimental *I*-*V* curves for QCD A (sample E2836) and QCD B (sample E2845) under forward and reverse bias. Being a potential current path, dislocations revealed in the TEM images can also contribute to the transport

properties. As expected the resistance is higher at 14 K than at 294 K which is determined by the active region. At low temperatures the majority of the electrons settle near the bottom of the occupied subbands. The curves of both structures have symmetric nature.

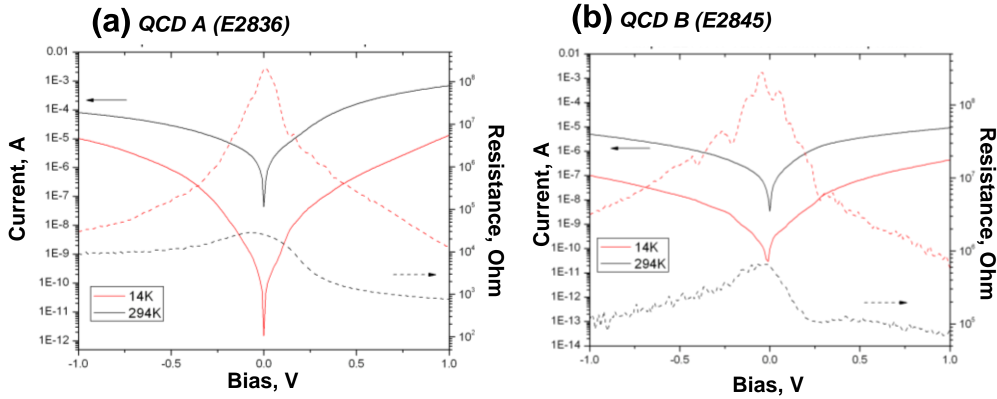

Figure 6.20. *I(R)-V measurements of QCD A (E2836) and B(E2845) performed at 14 K and 249 K (Measurements were performed at Technion, Israel).*

6.4 Conclusions

GaN/Al(Ga)N QCD operating at room temperature with the spectral sensitivity peaked at 1.5 μm have been demonstrated. The responsivity of the detector is estimated to be 15 V/W at 300 K. This device meant a record shortest operating wavelength for QCDs ever presented in any material system.

Two series of QCDs for the 3-5 μm spectral range where synthesized with different silicon concentration in the active QWs. The QCD based on a $GaN/Al_{0.35}Ga_{0.65}N$ chirped SL with moderate doping display well-resolved room-temperature ISB absorption, and PV response at 14 K. Like in the case of QW superlattices, increasing doping levels results in an enhancement of the ISB absorption, associated to blue shift and broadening. However, high doping levels result also in a decrease of the resistance of the active region, which hinders the photovoltaic response. Therefore, I have proved that the doping level is a critical parameter defining the optical and electrical response of the detector.

Chapter 7

Terahertz ISB absorption

In this chapter I introduce the material issues which one meets when designing GaN-based ISB devices in the terahertz spectral range. A step-QW structure is presented as a possible design to achieve a flat band potential. The plasma-assisted MBE growth of the sample and the challenges associated to its structural characterization are described. Finally, low-temperature TE- and TM-polarized ISB absorption measurements are compared in order to confirm ISB absorption in the terahertz spectral range.

7.1 Motivation

T-rays, often called terahertz radiation, are electromagnetic waves in the far infrared part of the spectrum from 30 μm to 1,000 μm, or the frequencies from 300 GHz to 10 THz. This nonionizing radiation is studied as a potential replacement of X-rays for medical screening. Applications of T-rays include biological and medical sciences, industrial, for example non-destructive testing of semiconductor integrated circuit chips, pharmaceutical quality control, security screening, e.g. recognition of explosives and hazardous materials (Tonouchi, 2007), communications technology and ultrafast spectroscopy. T-rays can penetrate paper and clothing, but not very far through the skin or biological molecules, so that objects hidden beneath clothing can be revealed by analyzing the scattered and reflected radiation. T-rays are already used in airports for security scanning for explosives and drug detection.

In spite of their interesting applications, T-rays remain one of the least developed spectral regions, characterized by a relative lack of convenient radiation sources, detectors and transmission technology. The traditional source of coherent T-rays is the optically-pumped THz laser (OPTL). An OPTL system consists of a grating-tuned CO_2 pump laser that excites a far-infrared (FIR) gas cell mounted in a laser resonator. OPTLs can operate at many discrete frequencies, ranging from less than 300 GHz to more than 10 THz.

Greatly desired for many applications is a compact, continuous-wave solid-state source which comes to bridge the gap between the FIR lasers and the transistor oscillators in gigahertz electronics. At these high frequencies, the power generated by solid-state electronic devices, such as transistors, Gunn oscillators or Schottky diode multipliers, rolls off owing to both transit-time and resistance-capacitance effects. Even for the best devices, the available power generated above 1 THz is generally below the milliwatt level. From the photonic viewpoint, direct terahertz generation is limited by the lack of appropriate materials with sufficiently small bandgap. Despite this limitation, a wide variety of techniques have been developed to generate radiation above 1 THz, many, for example, based on photomixing of near-infrared lasers, or by direct multiplication up from the millimeter-wave regime. Backward-wave oscillators can also be used to generate tunable output at the long-wavelength end of the THz spectrum. Table 7.1 compares some of the techniques for generating T-rays. All these technologies are really bulky, and their replacement by compact solid-state devices has impelled worldwide research efforts in the last decade.

Table 7.1. *Techniques for generationTHz radiation.*

	OPTL	**Time domain spectroscopy**	**Backward wave oscillators**	**Direct multiplied sources**	**Frequency mixing**
Average power	>100 mW[a]	~1 μW	10 mW	mW to μW (decreasing with increasing frequency)	Tens of nW
Usable range	0.3-10 THz	~0.1-2 THz	0.1-1.5 THz	0.1-1 THz	0.3-10 THz
Tunability	discrete lines[b]	N/A	200 GHz	~10-15% of center frequency	Continuous
cw / pulsed	cw / pulsed	Pulsed	Cw	Cw	Cw

[a] *More than 1 W can be obtained at selected frequencies.*
[b] *Can be converted to tunable output using a Schottky-based sideband generator.*

A significant breakthrough took place in 2002 with the first demonstration of a GaAs-based QCL operating at ~4.4 THz (Köhler, 2002). Rapid progress has been made in terms of device performance. To date, QCL has been demonstrated in the 0.85-5 THz range (Williams, 2007), with pulsed operation up to 186 K (Kumar, 2009), and output powers of up to 250 mW pulsed (Williams, 2001). There are two major processes that

cause the degradation of population inversion (and thus gain) in THz QCLs at higher temperatures: thermal backfilling and thermally activated phonon scattering. Backfilling of the lower radiative state with electrons from the heavily populated injector occurs either by thermal excitation (according to the Boltzmann distribution), or by reabsorption of non-equilibrium LO-phonons, the hot-phonon effect (Lu, 2006). The other main degradation mechanism is the onset of thermally activated LO-phonon scattering, as electrons in the upper radiative state acquire sufficient in-plane kinetic energy to emit an LO-phonon and relax nonradiatively to the lower radiative state. This causes the upper-state lifetime to decrease exponentially according to

$$\tau_{12} \propto \exp[-(E_{LO} - h\nu).k_B T_e] \qquad [7.1]$$

where $h\nu$ is the THz photon energy, and k_B is the Boltzmann constant. Both of these mechanisms sensitively depend on the electron gas temperature T_e, which is 50-100 K higher than the lattice temperature during device operation.

Figure 7.1 presents survey of the reported performances of THz QCL in terms of operating temperature as a function of the lasing frequency. In general, resonant photon (RP) designs have better temperature performance than bound-to-continuum (BTC) designs. The explicit inclusion of an LO-phonon scattering event for depopulation means that RP designs present a larger energetic barrier (about 36 meV) to thermal backfilling than most BTC designs (about 15-20 meV). Therefore, BTC designs tend to top out around 100-115 K, whereas well-designed RP lasers can operate up to 150-180 K in pulsed mode. However, the low LO-phonon energy in arsenide compounds constitutes a major bottleneck for operation at higher temperatures. Room-temperature operation of THz QCLs requires an additional revolution in the field through the use of a new material system. III-nitride semiconductors, with an LO-phonon energy of 92 meV, are the most promising choice to develop solid-state coherent THz sources operating at room temperature.

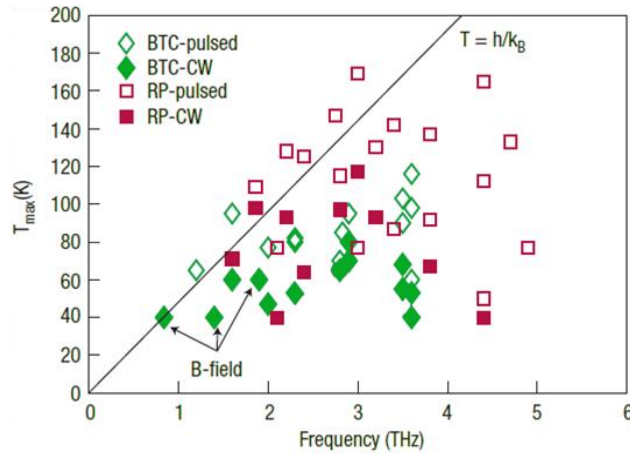

Figure 7.1. *Survey of the reported performance of THz QCLs in terms of operating temperature as a function of the lasing frequency(after Williams, 2007). Data are sorted by pulsed or cw performance and active region design (BTC or RP). Several of the low-frequency designs operate with the assistance of a magnetic field (B-field).*

7.2 Step-QW superlattices for terahertz absorption

There are a number of theoretical proposals for nitride devices operating in the far-IR region (Jovanovic, 2004; Sun, 2005; Vukmirovic, 2005; Bellotti, 2008; Bellotti, 2009). However, the demonstration of a nitride-based THz QCL must still face two major challenges: a more robust design of the active QWs to obtain ISB transitions in the far-IR, and the leakage currents associated to threading dislocations arising from the heteroepitaxial growth of GaN.

The presence of a polarization-related built-in electrical field in wurtzite III-N materials makes it impossible to tune ISB absorption to longer wavelengths just by increasing the QW width. Figure 7.2 presents a schematic of conduction band profiles and electron wave functions for two GaN/AlGaN QWs with the same Al mole fraction in the barriers and relatively large well thickness. When increasing the GaN layer thickness beyond a certain threshold, the energy separation between first electronic levels remains almost unchanged as the e_1 and e_2 levels get trapped into triangular potential. In this situation the energy states are governed by the internal electrical field and not by the geometry of the QW.

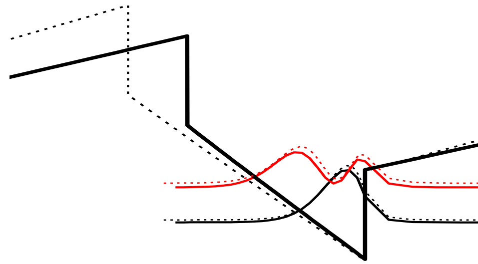

Figure 7.2. *(a)* ***Schematic of*** *conduction band profiles and envelope functions for two QWs with different well thicknesses designed for operation in far infrared.*

One way to overcome this problem is to approach a flat band potential by engineering the built-in electric field in a more complex design, which should include coupled QWs or QWs with asymmetric barriers. In our case, we have investigated a structure containing a 40 period SL of step-QWs which consists of 3-nm-thick GaN QW, 10-nm-thick $Al_{0.05}Ga_{0.95}N$ step and 3-nm-thick $Al_{0.1}Ga_{0.9}N$ spacer barrier. Figure 7.3 presents nextnano^3 calculations of the step-QW band profile and envelope functions. As it is seen from the simulations, the potential of the $Al_{0.05}Ga_{0.95}N$ step is almost flat and e_1 and e_2 levels are confined by the $Al_{0.1}Ga_{0.9}N$ barriers. The energy separation predicted by the calculations is about 4.3 THz.

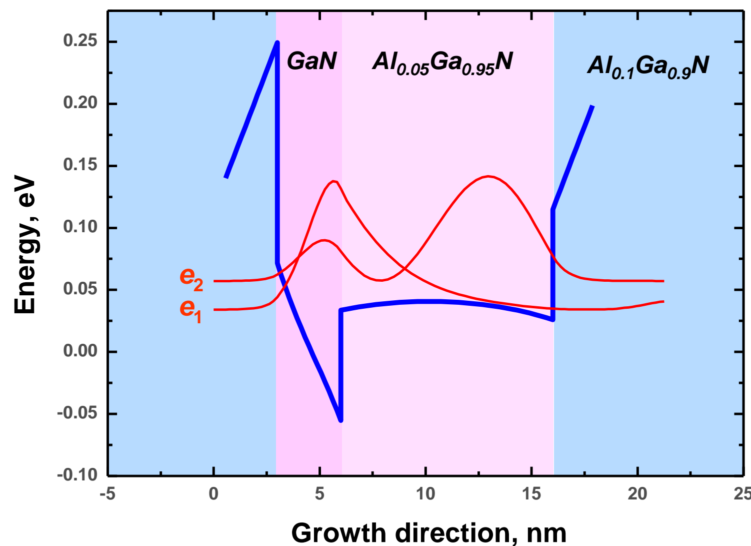

Figure 7.3. *Conduction band profile and envelope functions of a $GaN/Al_{0.05}Ga_{0.95}N/Al_{0.1}Ga_{0.9}N$ step QW within a superlattice.*

The step-QW SL was grown on a GaN-on-Si(111) template by plasma-assisted MBE under Ga-rich growth conditions, as described in Chapter 3. The GaN was doped

with [Si] = 1×10^{19} cm^{-3} and the active region was sandwiched between 50-nm-thick $Al_{0.05}Ga_{0.95}N$ non-intentionally-doped cladding layers.

As expected for a heterostructure with low Al content, TEM experiments reveal a good quality of the grown step-QW SL with, low density of threading dislocations, generated mainly at the $Al_{0.05}Ga_{0.95}N$ buffer / SL interface (Fig. 7.4). High-resolution images did not show stacking faults or any other extended defects in the active region.

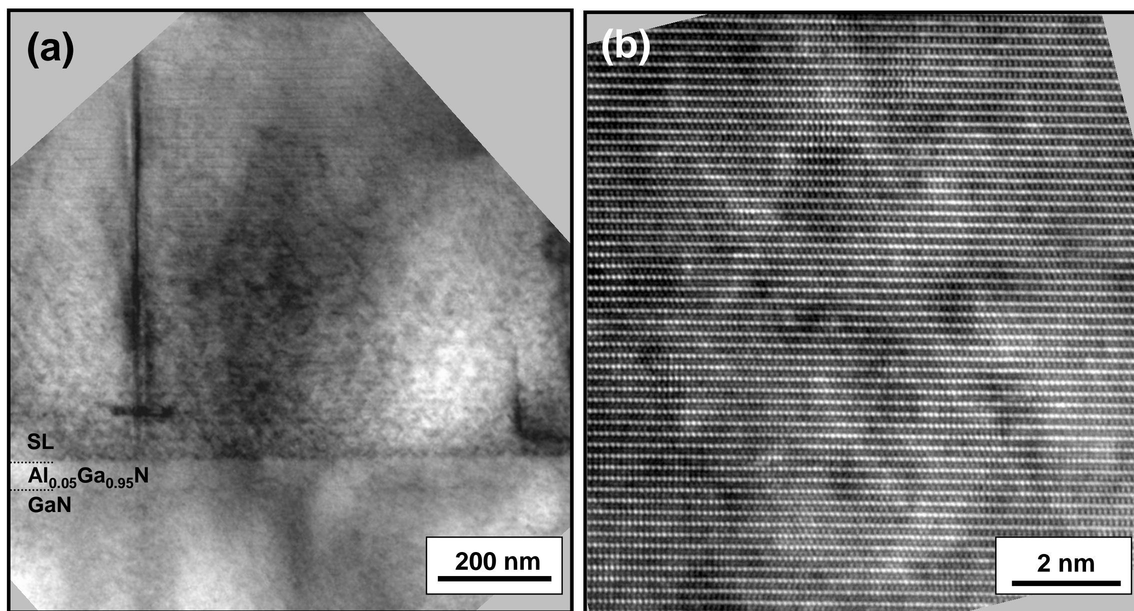

Figure 7.4. *(a) TEM and (b) high-resolution TEM images of a step QW SL.*

Figure 7.5 shows high-resolution $\omega - 2\Theta$ scan around (0002) reflection of the SL. Presence of several SL satellites in the scan which is a confirmation of a high quality heterostructure is in a good agreement with TEM data. The period extracted from XRD points to be about 6% smaller than the nominal one, with Al mole fractions that could be smaller by 10%.

The various layer thicknesses were verified by cross-section conventional TEM, as illustrated in Figure 7.5 (on the right), since high-resolution images do not provide enough chemical contrast or difference in the lattice parameters to identify the various materials [see Fig. 7.4(b)].

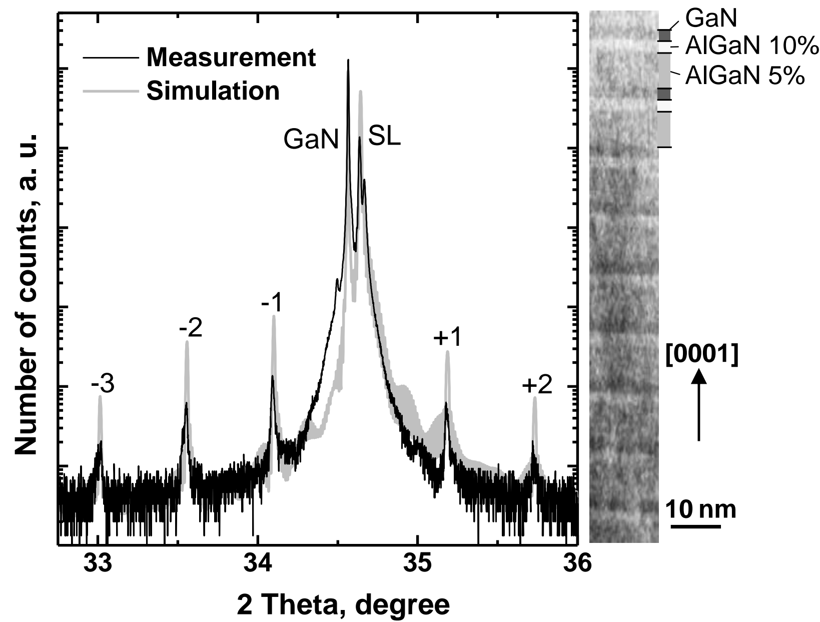

Figure 7.5. *High-resolution ω – 2Θ scan around (0002) x-ray reflection of step QW SL (black) and theoretical calculations (gray) using X'Pert Epitaxy 40 software from Philips Analytical. On the right is the cross-section conventional transmission electron microscopy image of the active region of the sample. The image contrast qualitatively correlates with the chemical composition of the layers.*

IR transmission measurements were performed at University Paris-Sud by the group of Prof. F. H. Julien. The sample was diced in two pieces with equal length of 3.9 mm, and the opposite facets of the two pieces were mechanically polished at an angle of 30°. In order to achieve enhancement of the ISB absorption the pieces were placed face-to-face under mechanical pressure on the cold finger of a liquid helium-cooled cryostat. The experiment was performed at $T = 4.7$ K using a Bruker FTIR spectrometer and detection was provided by a liquid helium-cooled silicon bolometer. Two pieces of GaN-on-Si(111) templates placed face-to-face were used were used as a reference. Each piece had piece had a length of 3.6 nm and thickness of 0.55 mm.

The IR transmission spectra for TM- and TE-polarized light for a step-QW SLs is presented in Fig. 7.6. The spectra from heterostructure are divided by the transmission spectra from the GaN-on-Si(111) template and normalized to 1 at low frequency. The sample exhibit ISB absorption peaked at 4.2 THz for TM-polarized which is in a good agreement with the theoretical calculations. The broadening factor $\Delta\lambda/\lambda$ is about 54%. This experiment was the first of observation of ISB absorption in the THz region using the III-nitride material system.

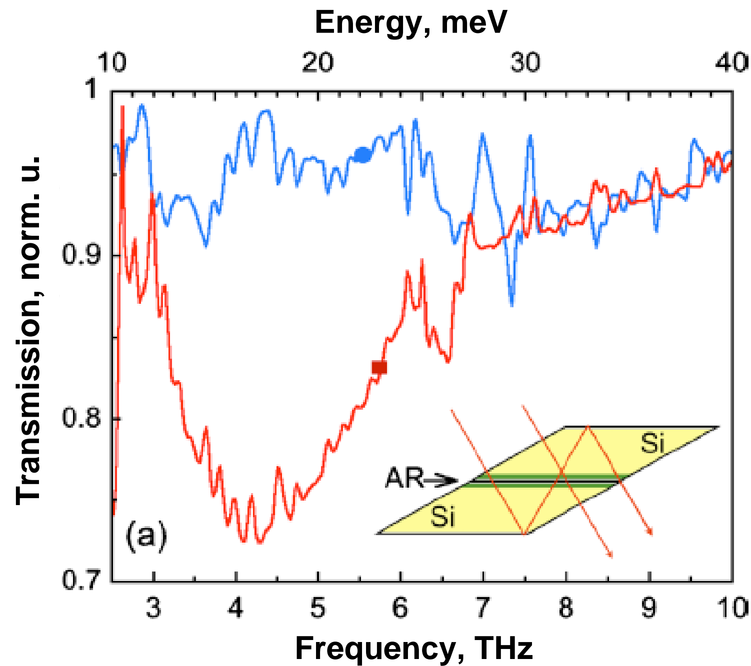

Figure 7.6. *Transmission spectra for TM- (red) and TE-polarized (blue) light at 4.7 K for a step-QW SL. The inset shows the experimental configuration with two pieces face-to-face and the ray tracing. The active region is shown by an arrow.*

7.2 Conclusions

One approach to make III-N material optically active in the technologically-relevant terahertz spectral region was presented. The issues of wurtzite III-nitride materials related to built in electric field were overcome by using asymmetric QWs in order to achieve a flat band potential of the heterostructure. Therefore, I grew a $GaN/Al_{0.05}Ga_{0.95}N/Al_{0.1}Ga_{0.9}N$ step-QW SL which exhibited ISB absorption peaked at 4.2 THz. The potential tuning of the transition wavelength and reduction of the FWHM of the peak could be achieved by varying the geometry of the step QW and optimizing the silicon distribution in the structure.

Chapter 8

Conclusions and perspectives

8.1 Conclusions

The aim of this work was directed to improve the performance and the understanding of the material issues involved in the GaN/AlGaN ISB technology, mainly targeting mid-IR operation, and to try to achieve operation of nitride based heterostructures at even longer wavelength. The accomplishments in these fields are described below.

I have first investigated the misfit relaxation processes during PAMBE growth of GaN/AlGaN SLs designed for ISB absorption in the 5–10 μm spectral range. I have analyzed SL grown with various Al content in the barriers and deposited on different buffer layers. The growth under tensile stress (using a GaN buffer) allows almost pseudomorphically deposited GaN/AlGaN SLs with Al content in the barrier not exceeding ≈30%, keeping edge-type TD densities below 2×10^{9} cm^{-2}. Increasing the Al mole fraction, results in an enhancement of misfit relaxation and in dislocation densities above 10^{10} cm^{-2}. In the case of growth under compressive stress (on AlGaN buffer), stronger relaxation occurs whatever the Al mole fraction, with the corresponding increase of the density of edge-type threading dislocations. In addition to the average relaxation trend of the SL, *in situ* strain measurements indicate a periodic fluctuation of the in-plane lattice parameter during the growth. In the case of GaN/AlN, we had demonstrated that this relaxation is associated to a plastic deformation with appearance of dislocations associated to stacking fault loops (Kandaswamy, 2010). In contrast, in GaN/AlGaN SLs, the observed fluctuations are explained by the different elastic response of the GaN and AlGaN surfaces to the Ga excess at the growth front.

On the other hand, I have studied effect of silicon doping of GaN QWs on the optical transitions in GaN/AlGaN SLs. PAMBE allows a good control of the amount and location of silicon doping during the growth of III-nitride heterostructures. The increase of the doping level in GaN/Al(Ga)N SLs has an influence on both interband and intraband transitions, resulting in a blue shift of the optical lines in both cases. The main mechanisms responsible for these shifts are the band-filling effect, in the case of interband transition, and exchange interaction together with depolarization shift, in the case of ISB transitions. These effects lead to a considerable discrepancy between 8-band k•p Schrödinger-Poisson calculations and the experimental operation wavelength of ISB devices. The two-level single particle approach is hence inapplicable for the ISB structures targeting the mid-IR spectral range and theoretical models for calculation ISB transitions should be revised.

Taking into account the relaxation and silicon doping studies described above, I have grown a GaN/Al(Ga)N QCD operating at room temperature with the spectral sensitivity peaked at 1.5 μm. The responsivity of the detector is estimated to be 15 V/W at 300 K. This device meant a record shortest operating wavelength for QCDs ever presented in any material system. QCDs for the 3-5 μm spectral range where also synthesized, with different silicon concentration in the active QWs. Like in the case of QW superlattices, increasing doping levels results in an enhancement of the ISB absorption, associated to blue shift and broadening. However, high doping levels result also in a decrease of the resistance of the active region, which hinders the photovoltaic response. Therefore, I have proved that the doping level is a critical parameter defining the optical and electrical response of the detector.

Finally, I have grown a III-nitride based step-QW heterostructure with ISB absorption in terahertz region peaked at 4.2 THz. The step-QW approach permitted to achieve the flat band potential and overcome material issues related to III-nitrides.

8.2 Perspectives

The interest for the development of a III-N ISB technology for the near-IR stems from the potential application for ultrafast photonic devices for optical telecommunication networks, as well as for application in a variety of chemical and

biological sensors. Different types of ISB devices has been demonstrated in this spectral range: all-optical switches, photodetectors, electro-optical modulators... The introduction of these devices in the market requires efforts in terms of improving their compatibility with silicon CMOS technology, their scalability and reducing their cost. The performance of these devices can and must be further improved. All-optical switches should take advantage on nanostructuring technologies to reduce the switching energy; the photodetector responsivity should be enhanced by improved device design (for instance, precisely tuning the coupling of the active quantum well with the extractor in quantum cascade detectors); the introduction of new concepts like phase modulation should lead to more compact and efficient waveguide-based switches.

In this work the first prototype of III-N based QCD photodetector for mid-IR spectral region was presented. However, bandgap engineering requires an exquisite control of material growth and modeling that are notoriously difficult in GaN/AlGaN. A slight misalignment between confinement states of the extractor region, caused for example by relaxation processes, would lead to inefficient electron extraction and hence deteriorating the device response. As well the quality of the epitaxial heterostructures is an important factor. Presence of threading dislocation and high silicon concentration may result in a short circuit of the device. Therefore the minimal dislocation density and optimal silicon doping level are needed to maintain the high resistance of the device active region in order to perform efficient detection.

An emerging field for GaN-based ISB devices is the extension towards the far-IR, with several theoretical designs of a GaN-based THz QCL recently reported. At far-IR wavelengths, the large GaN LO-phonon energy (92 meV) becomes a valuable property to achieve ISB operation at relatively high temperatures, and also to cover IR wavelengths that are not accessible by other III-V semiconductors due to Reststrahlen absorption. The success of nitride technology in this spectral range depends on the development of novel strategies for the device design and advanced growth and processing technologies. To achieve the low defect density required for QCL fabrication, two approaches can considered: (i) fabrication of planar structures on high-quality bulk GaN substrates, and (ii) synthesis of the structures on nanostructures substrates using localized growth, method that can provide defect-free material at a

lower cost and with additional advantages in terms of low dimensionality. Then, targeting longer wavelengths requires also an effort to improve the modeling tools to achieve a better fit to the experiment for ternary alloys with low Al mole fraction and to account for many-body effects such as exchange interaction and depolarization shift. Furthermore, band schemes based on coupled-QWs or asymmetric QWs are required, and several iterations between design and experiments will be required to attain a reasonable band diagram for a nitride QCL.

References

(Adachi, 1994) S. Adachi (1994) '*GaAs and Related Materials: Bulk Semiconducting and Superlattice Properties*', World Scientific Publishing Company.

(Adelmann, 2003) C. Adelmann, E. Sarigiannidou, D. Jalabert, Y. Hori, J.-L. Rouviere, B. Daudin (2003), '*Growth and optical properties of GaN/AlN quantum wells'*, Appl. Phys. Lett. 82, 4154.

(Ando, 1982) T. Ando, A. B. Fowler, F.Stern (1982) '*Electronic properties of two-dimensional electronic systems*', Rev. Mod. Phys. 54, 437-672.

(Ambacher, 1998) O. Ambacher (1998) '*Growth and application of group III-nitrides*', J. Phys. D: Appl. Phys. 31, 2653-2710.

(Ambacher, 1999) O. Ambacher, J. Smart, J. R. Shealy, N. G. Weimann, K. Chu, M. Murphy, W. J. Schaff, and L. F. Eastman (1999) '*Two-dimentional electron gas induced by spontaneous and piezoelectric polarization charges in N- and Ga-face AlGaN/GaN heterostructures*', J. Appl. Phys. 85, 3222.

(Allen, 1976) S. J. Allen, Jr., D. C. Tsui, B. Vinter (1976) '*On the absorption of infrared radiation by electrons in semiconductor inversion layers*', Solid State Commun. 20, 425.

(Bandara, 1988) K. M. S. V. Bandara, D. D. Coon, O. Byungsung (1988) '*Exchange interaction in quamtum well subbands*', Appl. Phys. Lett. 53, 1931.

(Bayram, 2012) C. Bayram (2012) '*High-quality AlGaN/GaN superlattices for near- and mid-infrared intersubband transitions*', J. Appl. Phys. 111, 013514.

(Bernardini, 1997) F. Bernardini, V. Fiorentini, D. Vanderbilt (1997) '*Spontaneous polarization and piezoelectric constants of III-V nitrides*', Phys. Rev. B 56, R10025.

(Bernardini, 1998) F. Bernardini, V. Fiorentini (1998) '*Macroscopic polarization and band offsets at nitride heterojunctions*', Phys. Rev. B 57, R9421 – R9430.

(Bernardini, 2001) F. Bernardini, V. Fiorentini (2001) '*Nonlinear macroscopic polarization in III-V nitride alloys*', Phys. Rev. 64, 085207.

(Bernardini, 2002) F. Bernardini, V. Fiorentini (2002) '*Nonlinear behavior of spontaneous and piezoelectric polarization in III-V nitride alloys*', Phys. Stat. Sol. 190, 65-73.

(Birner, 2007) S. Birner, T. Zibold, T. Andlauer, T. Kubis, M. Sabathil, A. Trellakis, P. Vogl (2007) '*Nextnano: General Purpose 3-D Simulations*' (2007), IEEE Trans. On Electron Dev. 54, 2137.

(Bloom, 1974) S. Bloom, G. Harbeke, E. Meier, I. B. Ortenburger (1974) *'Band structure and reflectivity of GaN*', Physica Status Solidi B 66, 161-168.

(Bloss, 1989) W. L. Bloss (1989) '*Effect of Hartee, exchange, and correlation energy on intersubband transitions*', J. Appl. Phys. 66, 3639.

(Boguslawski, 2000) P. Boguslawski, K. Rapcewicz, J. J. Bernholc (2000) '*Surface segregation and interface stability of AlN/GaN, GaN/InN, and AlN/InN \{0001\} epitaxial systems*', Phys. Rev. B 61, 10820 – 10826

(Bougrov, 2001) V. Bougrov, M. E. Levinshtein, S. L. Rumyantsev, A. Zubrilov A (2001) '*Properties of Advanced SemiconductorMaterials GaN, AlN, InN, BN, SiC, SiGe'*. Eds. M.E. Levinshtein, S.L. Rumyantsev, M.S. Shur, John Wiley & Sons, Inc., New York, 1-30.

(Bourne, 1972) J. Bourne, R. L. Jacobs (1972) '*The band structure of GaN*', J. Phys. C: Solid State Phys.

(Bykhovski, 1997) A. D. Bykhovski, B. L. Gelmont, M. S. Shur (1997) '*Elastic strain relaxation and piezoeffect in GaN-AlN, GaN-AlGaN and GaN-InGaN superlattices*', J. Appl. Phys. 81, 6332.

(Cantu, 2005) P. Cantu, F. Wu, P. Waltereit, S. Keller, A. E. Romanov, S. P. DenBaars, J. S. Speck (2005) '*Role of inclined threading dislocations in stress relaxation in mismatched layers'*, J. Appl. Phys. 97, 103534.

(Carvalho, 2010) L. C. de Carvalho, A. Schleife, F. Fuchs, F. Bechstedt (2010) '*Valence-band splitting in cubic and hexagonal AlN, GaN, and InN*', Appl. Phys. Lett. 97, 232101.

(Chang, 1996) S. L. Chuang, C. S. Chang (1996) '*The k.p method for strained wurtzite semiconductors*', Phys. Rev. B 54, 2491.

(Cociorva, 2002) D. Cociorva, W. G. Aulbur, J. W. Wilkins (2002) '*Quasipartical calculations of band offsets at AlN-GaN interface*', Solide State Comm.124, 63 – 66.

(Chen, 1996) G. D. Chen, M. Smith, J. Y. Lin, H. X. Jiang, S.-H. Wie, M. A. Khan, C. J. Sun (1996) '*Fundamental optical transition in GaN*', J. Appl. Phys. 68, 2784.

(Cherns, 2008) P. D. Cherns, C. McAleese, M. J. Kappers, C. J. Humphreys (2008) '*A TEM study of AlN interlayer defects in AlGaN/GaN heterostructures'*, Springer Proc. In Physics 120, 25.

(Chow, 1996) T.P Chow, Ghezzo. 'SiC power devices. In *III-Nitride, SiC, and Diamond Materials for Electronic Devices'* (1996), Eds. D.K Gaskill, C.D. Brandt and R.J. Nemanich, Material Research Society Symposium Proceedings, Pittsburgh, 423, 69-73.

(Davydov, 2002) V. Yu. Davydov, A.A. Klochikhin, V.V. Emtsev, D.A. Kurdyukov, S.V. Ivanov, V.A. Vekshin, F. Bechstedt, J. Furthmüller, J. Aderhold, J. Graul, A.V. Mudryi, H. Harima, A. Hashimoto, A. Yamamoto, E.E. Haller (2002) '*Band Gap of Hexagonal InN and InGaN Alloys*', Physica Status Solidi B, 34, 787 – 795.

(De-Sheng, 1982) Jiang De-Sheng, Y. Makita, K. Ploog, H. J. Queisser (1982) '*Electrical properties and photoluminescence of Te- doped GaAs grown by molecular beam epitaxy*', J. Appl. Phys. 53, 999.

(Einfeldt, 2001) S. Einfeldt, H. Heinke, V. Kirchner, D. Hommel (2001) '*Strain relaxation in AlGaN/GaN superlattices grown on GaN*', J. Appl. Phys. 89, 2160.

(Faist, 1994) J. Faist, F. Capasso, D. L. Sivco, C. Sirtori, A. L. Hutchinson, A. Y. Cho (1994), '*Quantum Cascade laser*', Science 264, 553.

(Fiorentini, 2002) V. Fiorentini, F. Bernardini, O. Ambacher (2002) '*Evidence for nonlinear macroscopic polarization in III–V nitride alloy heterostructures*', Appl. Phys. Lett. 80, 1204.

(Floro, 2004) J. A. Floro, D. M. Follstaedt, P. Provencio, S. J. Hearne, S. R. Lee (2004) '*Misfit dislocation formation in the AlGaN/GaN heterointerface*', J. Appl. Phys. 96, 7087.

(Fonoberov, 2003) V. A. Fonoberov, A. A. Balandin (2003) '*Excitonic properties of strained wurtzite and zinc-blende GaN/$Al_xGa_{1-x}N$ quantum dots*', J.

Appl. Phys. 94, 7178.

(Gendron, 2004) L. Gendron, M. Carras, A. Huynh, V. Ortiz, C. Koeniguer, V. Berger (2004) '*Quantum cascade detector*', Appl. Phys. Lett. 85, 2824.

(Giorgetta, 2002) F. R. Giorgetta, E. Baumann, D. Hofstetter, C. Manz, Q. Yang, K. Köhler, M. Graf (2007) *'InGaAs/AlAsSb quantum cascade detectors operating in the near infrared*', Appl. Phys. Lett. 91, 111115.

(Giorgetta, 2007) F. R. Giorgetta, E. Baumann, M. Graf, L. Ajili, N. Hoyler, M. Giovannini, J. Faist, D. Hofstetter, P. Krötz, G. Sonnabend (2007) '*16.5 µm quantum cascade detector using miniband transport'*, Appl. Phys. Lett. 90, 231111.

(Gunapala, 2005) S. D. Gunapala, S. V. Bandara, J. K. Liu, C. J. Hill, S. B. Rafol, J. M.Mumolo, J. T. Trinh, M. Z. Tidrow, P. D. LeVan (2005) '*Development of midwavelength and long-wavelength megapixel portable QWIP imaging cameras*', Infrared Phys. Technol. 47, 67 – 75.

(Guo, 1994) Q. Guo, A. Yoshisa (1994) '*Temperature dependence of band gap change in InN and AlN*', Jpn. J. Appl. Phys. 33, 2453 – 2456.

(Hearne, 2000) S. J. Hearne, J. Han, S. R. Lee, J. A. Floro, D. M. Follstaedt, E. Chason, I. S. T. Tsong (2000) '*Brittle-ductile relaxation kinetics of strained AlGaN/GaN heterostructures*', Appl. Phys. Lett. 76, 1534.

(Hellman, 1998) E. S. Hellman (1998) '*The polarity of GaN: a critical review*', MRS Internet J. N. S. R. 3, 1-12.

(Helman, 2003) A. Helman, M. Tchernycheva, A. Lusson, E. Warde, F. H. Julien, Kh. Moumanis, G. Fishman, E. Monroy, B. Daudin, D. Le Si Dang, E. Bellet-Amalric, D. Jalabert (2003) '*Intersubband spectroscopy of doped and undoped GaN/AlN quantum wells grown by molecular-beam epitaxy*', Appl. Phys. Lett. 83, 5196.

(Hofstetter, 2002) D. Hofstetter, M. Beck, J. Faist (2002) '*Quantum-cascade-laser structures as photodetectors*', Appl. Phys. Lett. 81, 2683.

(Hofstetter, 2006) D. Hofstetter, E. Baumann, F. R. Giorgetta, M. Graf, M. Maier, F. Guillot, E. Bellet-Amalric, E. Monroy (2006) '*High-quality AlN/GaN-superlattice structures for the fabrication of narrow-band 1.4 µm photovoltaic intersubband detectors*', Appl. Phys. Lett. 88, 121112.

(Hofstetter, 2011) D. Hofstetter, J. D. Francsco, D. Martin, N. Grandjean, Y. Kotsar, E. Monroy (2011) '*Si-interdiffusion in heavily doped AlN-GaN-based quantum well intersubband photodetectors*', Appl. Phys. Lett. 98, 241101.

(Jain, 2000) S. C. Jain, M. Willander, J. Narayan, R. V. Overstraeten (2000) '*III-nitrides: Growth, characterization, and properties'*, J. Appl. Phys. 87, 965.

(Iliopoulos, 2002) E. Iliopoulos, T. D. Moustakas (2002) '*Growth kinetics of AlGaN films by plasma-assisted molecular-beam epitaxy'*, Appl. Phys. Lett. 81, 295.

(Ibbeston, 2000) J. P. Ibbeston, P. T. Fini, K. D. Ness, S. P. DenBaars, J. S. Speck, U. K. Mishra (2000) '*Polarization effects, surface states, and the source of electrons in AlGaN/GaN heterostructure field effect transistors*', Appl. Phys. Lett. 77, 250.

(Iizuka, 2000) N. Iizuka, K. Kaneko, N. Suzuki, T. Asano, S. Noda, O. Wada, (2000), '*Ultrafast intersubband relaxation (150 fs) in AlGaN/GaN multiple quantum wells*', Appl. Phys. Lett., 77, 648.

(Iizuka, 2006) N. Iizuka, K. Kaneko, N. Suzuki (2006) '*All-optical switch utilizing*

intersubband transition in GaN quantum wells', *IEEE J. Quantum Electron*,. 42, 765.

(Kandaswamy, 2008) P. K. Kandaswamy, F. Guillot, E. Bellet-Amalric, E. Monroy, L. Nevou, M. Tchernycheva, A. Michon, F. H. Julien, E. Baumann, F. R. Giorgetta, D. Hofstetter, T. Remmele, M. Albrecht, S. Bilner, and Le Si Dang (2008) '*GaN/AlN short-period superlattices for intersubband optoelectronics: A systematic study of their epitaxial growth, design, and performance*', J. Appl. Phys. 104, 093501.

(Kandaswamy, 2009) P. K. Kandaswamy, H. Machhadani, C. Bougerol, S. Sakr, M. Tchernycheva, F. H. Julien, E. Monroy (2009) '*Effect of doping on the mid-infrared intersubband absorption in GaN/AlGaN superlattices grown on Si(111) templates*', Appl. Phys. Lett. 95 141911.

(Kandaswamy, 2010) P. K. Kandaswamy, H. Machhadani, Y. Kotsar, S. Sakr, A. Das, M. Tchernycheva, L. Rapenne, E. Sarigiannidou, F. H. Julien, E. Monroy (2010) '*Effect of doping on the mid-infrared intersubband absorption in GaN/AlGaN superlattices grown on Si(111) templates*', Appl. Phys. Lett. 96, 141903.

(Kandaswamy, 2010a) P. K. Kandaswamy (2010), doctorate dissertation title '*Al(Ga)N/GaN nanostructures for Near- and Mid infrared intersubband optoelectronics*' performed at NPSC / INAC / CEA - Grenoble, France.

(Kang, 2006) S. W. Kang, H. W. Shim, D.-Y. Lee, S.-H. Han, D. J. Kim, J. W. Kim, B. W. Oh, O. Kryliouk, T. J. Anderson (2006) '*Effects on Optical Characteristics of GaN Polarity Controlled by Substrate*', J. Semic. Techn. And Sc. 6.

(Kehagias, 2005) Th. Kehagias, A. Delimitis, Ph. Komninou, E. Iliopoulos, E. Dimakis, A. Georgakilas, G. Nouet (2005) '*Misfit accommodation of compact and columnar InN epilayers grown on Ga-face GaN (0001) by molecular-beam epitaxy*', Appl. Phys. Lett. 86, 151905.

(Keller, 2006) S. Keller, N. Fichtenbaum, F. Wu, G. Lee, S. P. Denbaars, J. S. Speck, U. K. Mishra (2006) '*Effect of the nucleation conditions on the polarity of AlN and GaN filmsgGrown on C-face 6H–SiC*', Jpn. J. Appl. Phys. 45, L322 – L325.

(Kim, 1997) K. Kim, W. R. L. Lambrecht, B. Segall (1997) '*Effective masses and valence-band splittings in GaN and AlN*', Phys. Rev. B 56, 7363.

(Kisielowski, 1996) C. Kisielowski, J. Krüger, S. Ruvimov, T. Suski, J. W. Ager, III, E. Jones, Z. Liliental-Weber, M. Rubin, E. R. Weber (1996) '*Strain-related phenomena in GaN thin films*', Phys. Rev. B 54, 17745–17753.

(Kobayashi, 1983) A. Kobayashi, O. F. Sankey, S. M. Volz, J. D. Dow (1983) '*Semiempirical tight-binding band structures of wurtzite semiconductors: AlN, CdS, CdSe, ZnS, and ZnO*', Phys. Rev. B 28, 935.

(Kohler, 2002) R. Köhler, A. Tredicucci, F. Beltram, H. E. Beere, E. H. Linfield, A. Giles Davies, D. A. Ritchie, R. C. Iotti, F. Rossi (2002) '*Terahertz semiconductor-heterostructure laser*', Nature 417, 156-159.

(Köhler, 2002) R. Köhler, A. Tredicucci, F. Beltram, H. E. Beere, E. H. Linfield, A. G. Davies, D. A. Ritchie, R. C. Iotti, F. Rossi (2002) '*Terahertz semiconductor-heterostructure laser*', Nature 417, 156-159.

(Kumar, 2009) Sushil Kumar, Qing Hu, John L. Reno (2009) '*186 K operation of terahertz quantum-cascade lasers based on a diagonal design*', Appl. Phys. Lett. 94, 131105.

(Lang, 2011) J. R. Lang, C. J. Neufeld, C. A. Hurni, S. C. Cruz, E. Matioli, U. K. Mishra, J. S. Speck (2011) '*High external quantum efficiency and fill-factor InGaN/GaN heterojunction solar cells grown by NH_3-based molecular beam epitaxy*', Appl. Phys. Lett. 98, 131115.

(Li, 1997) Y. Li, Y. Lu, H. Shen, M. Wraback, M. G. Brown, M. Schurman, L. Koszi, R. A. Stall (1997) '*temperature dependence of energy band gap in GaN thin film studied by thermomodulation*', Appl. Phys. Lett. 70, 2458.

(Li, 2004) J. M. Li, X. X. Han, J. J. Wu, X. L. Liu, Q. S. Zhu, Z. G. Wang (2005) '*Origin of the blue shift in the infrared absorbance of the intersubband transitions in $Al_xGa_{1-x}N$/GaN multiple quantum wells*', Physica E 25, 575 – 581.

(Li, 2005) J. M. Li, X. X. Han, J. J. Wu, X. L. Liu, Q. S. Zhu, Z. G. Wang (2005) '*Origin of the infrared absorbance of intersubband transitions in $Al_xGa_{1-x}N$/GaN multiple quantum well*', Physica E 25, 575.

(Limtimein, 2002) F. Litimein, B. Bouhafs, Z. Dridi, P. Ruterana (2002) '*The electronic structure of wurtzite and zincblende AlN: an ab initio comparative study*', New J. Phys. 4, 64.

(Liu, 2006) R. Liu, J. Mei, S. Srinivasan, F. A. Ponce, H. Omiya, Y. Narukawa, T. Mukai (2006) '*Generation of misfit dislocations by basal-plane slip in InGaN/GaN heterostructures*', Appl. Phys. Lett. 89, 201911.

(Lu, 2006) J. T. Lü, J. C. Cao (2006) '*Coulomb scattering in the Monte Carlo simulation of terahertz quantum-cascade lasers*', *Appl. Phys. Lett.* 88, 061119.

(Ma, 2007) B. S. Ma, W. J. Fan, Y. X. Dang, W. K. Cheah, W. K. Loke, W. Liu, D. S. Li, S. F. Yoon, D. H. Zhang, H. Wang, C. H. Tung (2007) '*GaInNAs double-barrier quantum well infrared photodetector with the photodetection at 1.24 μm*', Appl. Phys. Lett. 91, 051102.

(Machhadani, 2009) H. Machhadani, P. Kandaswamy, S. Sakr, A. Vardi, A. Wirtmüller, L. Nevou, F. Guillot, G. Pozzovivo, M. Tchernycheva, A. Lupu, L. Vivien, P. Crozat, E. Warde, C. Bougerol, S. Schacham, G. Strasser, G. Bahir, E. Monroy, F. H. Julien (2009) '*GaN/AlGaN intersubband optoelectronic devices*', N. J. Phys. 11**,** 125023.

(Manasreh, 1991) M. O. Manasreh, F. Szmulowicz, T. Vaughan, K. R. Evans, C. E. Stutz, D. W. Fischer (1991) '*Origin of the blueshift in the intersubband infrared absorption in GaAs/$Al_{0.3}Ga_{0.7}As$ multiple quantum wells*', Phys. Rev. B , 43.

(Mahan, 1980) G. D. Mahan (1980) '*Energy gap in Si and Ge: Impurity dependence*', J. Appl. Phys. 51, 2634.

(Martin, 1996) G. Martin, A. Botchkarev, A. Rockett, H. Morcos (1996) '*Valenceband discontinuities of wurtzite GaN, AlN, and InN heterojunctions measured by xray photoemission spectroscopy*', Appl. Phys. Lett. 68, 2541.

(Masui, 2010) H. Masui, S. Nakamura, S. P. DenBaars, U. K. Mishra (2010) '*Nonpolar and Semipolar III-Nitride Light-Emitting Diodes: Achievements and Challenges*', IEEE Transactions on Electron Devices 57, 88-100.

(Mathis, 2001) S.K. Mathis, A.E. Romanov, L.F. Chen, G.E. Beltz,W. Pompe, J.S. Speck (2001) '*Modeling of threading dislocation reduction in growing GaN layers*', J. Cryst. Growth 231, 371 – 390.

(Matsumoto, 1974) T. Matsumoto, M. Aoki (1974) '*Temperature dependence of photoluminescence from GaN*', Jpn. J. Appl. Phys. 13, 1804 – 1807.

(Monroy, 2003) E. Monroy, B. Daudin, E. Bellet-Amalric, N. Gogneau, D. Jalabert, F. Enjalbert, J. Brault, J. Barjon, Le Si Dang (2003) '*Surfactant effect of In for AlGaN growth by plasma-assisted molecular beam epitaxy'*, J. Appl. Phys.93, 1550.

(Moran, 2004) B. Moran, F. Wu, A.E. Romanov, U.K. Mishra, S.P. Denbaars, J.S. Speck (2004) '*Structural and morphological evolution of GaN grown by metalorganic chemical vapor deposition on SiC substrates using an AlN initial layer*', J. Cryst. Growth 273, 38.

(Ng, 2001) H.M. Ng, R. Harel, S.N.G. Chu, A.Y. Cho (2001) '*The Effect of Built-in Electric Field in GaN/AlGaN Quantum Wells with High AlN Mole Fraction*', J. Electron. Mat. 30.

(Nicolay, 2007) S. Nicolay, E. Feltin, J.-F. Carlin, N. Grandjean, L. Nevou, F. H. Julien,M. Schmidbauer, T. Remmele, M. Albrecht (2007) '*Strain-induced interface instability in GaN/AlN multiple quantum wells'* , Appl. Phys. Lett. 91, 061927.

(Northrup, 1999) J. E. Northrup, J. Neugebauer (1999) '*Indium-induced changes in GaN(0001) surface morphology*', Phys. Rev. B 60, R8473.

(Olszakier, 1989) M. Olszakier, E. Ehrenfreund, E. Cohen, J. Bajaj, G. J. Sullivan (1989) '*Photoinduced intersubband absorption in undoped multi-quantum-well structures*', Phys. Rev. Lett. 62, 2997-2999.

(Pankove, 1975) J.I. Pankove, S. Bloom, G. Harbeke (1975) '*Optical properties of GaN*', *RCA Rev.* 36, 163.

(Ponce, 1997) F.A. Ponce (1997) '*Defects and interfaces in GaN epitaxy'*, MRS Bulletin 22. 8.

(Ramos, 2001) L. E. Ramos, L. K. Teles, L. M. R. Scolfaro, J. L. P. Castineira, A. L. Rosa, J. R. Leite (2001) '*Structural, electronic, and effective-mass properties of silicon and zinc-blende group-III nitride semiconductor compounds*', Phys. Rev. B 63, 165210.

(Salvador, 1995) A. Salvador, G. Liu, W. Kim, O. Aktas, A. Botchakarev, H. Morkoc (1995) '*Properties of a Si-doped GaN/AlGaN quantun well*', Appl. Phys. Lett. 67, 3322.

(Santic, 2003) B. Santic (2003) '*On the hole effective mass and the free hole statistics in wurtzite GaN*', Semicond. Sci. Technol. 18, 219–224.

(Scalari, 2009) G. Scalari, C. Walther, M. Fisher, R. Terazzi, H. Beere, D. Ritchie, J. Faist (2009) '*THz and sub-THz quantum cascade lasers*', Laser and Photon. Rev. 3, 45 (2009)

(Schuster, 1999) M Schuster, P O Gervais, B Jobst, W Hösle[I], R Averbeck, H Riechert, A Iberl, R Stömmer (1999) '*Determination of the chemical composition of distorted InGaN/GaN heterostructures from x-ray diffraction data*', J. Phys. D: Appl. Phys. 32 A56.

(Shtrichman, 2001) I. Shtrichman, C. Metzner, E. Ehrenfreund, D. Gershoni, K. D. Maranowski, A. C. Gossard (2001) '*Depolarization shift of the intersubband resonance in a quantum well with an electron-hole plasma*', Phys. Rev. B 65, 0.35310.

(Slack, 2002) G.A. Slack, L. J. Schowalter, D. Morelli, J. J. Freitas (2002) '*Some Effects of Oxygen Impurities on AlN and GaN*', J. Cryst. Growth 246, 287.

(Song, 2005) T. L. Song (2005) '*Strain relaxation due to V-pit formation in* $In_xGa_{1-x}N$*/GaN epilayers grown on sapphire*', J. Appl. Phys. Lett. 98, 084906.

(Sun, 1994) C. J. Sun, P. Kung, A. Saxler, H. Ohsato, E. Bigan, M. Razeghi, and D. K. Gaskill (1994) '*Thermal stability of GaN thin films grown on (0001)* Al_2O_3*, (0112)* Al_2O_3 *and* $(0001)_{Si}$ *6H-SiC substrates*', J. Appl.

Phys. 76, 236.

(Sun, 2008) Q. Sun, Y. S. Cho, I.-H. Lee, J. Han, B. H. Kong, and H. K. Cho (2008) '*Nitrogen-polar GaN growth evolution on c-plane sapphire*', Appl. Phys. Lett. 93, 131912.

(Suzuki, 1995) M. Suzuki, T. Uenoyama, A. Yanase (1995) '*First-principle calculations of effective-mass parameters of AlN and GaN*', Phys. Rev. B 52, 8132-8139.

(Teisseyre, 1994) H. Teisseyre, P. Perlin, T. Suski, I. Grzegory, S. Porowski, J. Jun, A. Pietraszko, T. D. Moustakas (1994) '*Temperature dependence of the energy gap in GaN bulk single crystals and epitaxial layer*', J. Appl. Phys. 76, 2429.

(Tchernycheva, 2006) M. Tchernycheva, L. Nevou, L. Doyennette, F. H. Julien, E. Warde, F. Guillot, E. Monroy, E. Bellet-Amalric, T. Remmele, M. Albrecht (2006) '*Systematic experimental and theoretical investigation of intersubband absorption in GaN/AlN quantum wells*', Phys. Rev. B 73, 125347.

(Tchernycheva, 2010) M. Tchernycheva, L. Nevou, L. Vivien, F. H. Julien, P. K. Kandasamy, E. Monroy, A. Vardi, G. Bahir (2010) '*Intersubband optics in a GaN-based nanostructures – physics and applications*', Phys. St. Sol. 247, 1622 – 1627.

(Tonouchi, 2007) M. Tonouchi (2007) '*Cutting-edge terahertz technology*', Nature Photonics 1, 97.

(Tu, 1992) K.-N. Tu, J. W. Mayer, L. C. Feldman (1992) '*Electronic Thin Film Science for Electrical Engineers and Material Scientist'*, Macmillan, New York.

(Varshni, 1967) Y. P. Varshni (1967) '*Temperature dependence of te energy gap in semiconductors*', Physica 34, 149 – 154.

(Vardi, 2008) A. Vardi, N. Kheirodin, L. Nevou, H. Machhadani, L. Vivien, P. Crozat, M. Tchernycheva, R. Colombelli, F. H. Julien, F. Guillot, C. Bougerol, E. Monroy, S. Schacham, G. Bahir (2008) '*High-speed operation of GaN/AlGaN quantum cascade detectors at $\lambda \approx 1.55\ \mu m$*', J. Appl. Phys. 93, 193509.

(Vardi, 2011) A. Vardi, S. Sakr, J. Mangeney, P. K. Kandaswamy, E. Monroy, M. Tchernycheva, S. E. Schacham, F. H. Julien, G. Bahir (2011) '*Femto-second electron transit time characterization in GaN/AlGaN quantum cascade detector at 1.5 micron*', Appl. Phys. Lett. 99, 202111.

(Vurgaftman, 2001) I. Vurgaftman, J. R. Meyer, L. R. Ram-Mohan (2001) '*Band parameters for III–V compound semiconductors and their alloys'* J. Appl. Phys. 89, 5815.

(Vurgaftman, 2003) I. Vurgaftman, J. R. Meyer (2003) '*Band parameters for nitrogen-containing semiconductors*', J. Appl. Phys. 94, 3675.

(Walther, 2007) C. Walther, M. Fischer, G. Scalari, R. Terazzi, N. Hoyler, J. Faist, "*Quantum cascade lasers operating from 1.2 to 1.6 THz*," Appl. Phys. Lett. 91, 131122.

(Winkelnkemper, 2006) M. Winkelnkemper, A. Schliwa, D. Bimberg (2006) '*Interrelation of structural and electronic properties in $In_xGa_{1-x}N/GaN$ quantum dots using an eight-band $k \cdot p$ model*', Phys. Rev. B 74, 155322.

(Williams, 2001) B. S. Williams, S. Kumar, Q. Hu, J. L. Reno (2001) '*Magnetotunneling spectroscopy of resonant anticrossing in terahertz intersubband emitters*', *Appl. Phys. Lett.* 79, 4444.

(Williams, 2007) B. S. Williams (2007) '*Terahertz quantum-cascade lasers*', Nature Photonics 1, 517.

(Wu, 2009) J. Wu (2009) '*When group-III nitrides go infrared: New properties and perspectives*', J. Appl. Phys., 106, 011101.

(Xu, 1993) Y.N Xu, W.Y. Ching (1993) '*Electronic, optical, and structural properties of some wurtzite crystals*',. Phys Rev. B 48, 4335-4351.

(Yang, 2006) Q. K. Yang, C. Manz, W. Bronner, K. Kohler, J. Wagner (2006) '*Room-temperature short-wavelength (λ ~ 3.7–3.9 μm) GaInAs/AlAsSb quantum-cascade lasers*', Appl. Phys. Lett. 88, 121127.

(Yoshikawa, 1999) M. Yoshikawa, M. Kunzer, J. Wagner, H. Obloh, P. Schlotter, R. Schmidt, N. Herres, U. Kaufmann (1999) '*Band-gap renormalization and band filling in Si-doped GaN films studied by photoluminescence spectroscopy*', J. Appl. Phys. 86, 4400-4402.

(Yun, 2002) F. Yun, M. A. Reshchikov, L. He, T. King, H. Morkoc, S. W. Novak, L. Wei (2002) '*Energy band bowing parameter in $Al_xGa_{1-x}N$ alloys*', J. Appl. Phys. 92, 4837.

Glossary

2D	two-dimensional
3D	three-dimensional
AFM	atomic force microscopy
BLIP	background limited infrared photodetection
BSF	basal stacking fault
BTP	bound-to-continuum
CCD	charge-couple device
FET	field-effect transistor
FTIR	fourier transform infrared spectroscopy
FWHM	full fidth at half maximum
HEMT	high-electron mobility transistor
XRTEM	high resolution transmission electron microscopy
HRXRD	high-resolution X-ray difraction
IR	infrared
ISB	inetrsubband
LED	light-emitting diodes
LO	longitudinal optical
OPTL	optically-pumped THz laser
PAMBE	plasma-assisted molecular beam epitaxy
PL	photoluminescence
PV	photovoltage
MBE	molecular beam epitaxy
MBMS	modulated beam mass spectrometry
MD	misfit dislocation
MOCVD	metalorganic chemical vapor deposition
PSF	prismatic stacking fault
RHEED	reflection high-energy electron diffraction
RMS	root mean square
RP	resonant photon

SF	stacking fault
SIMS	secondary ion mass spectroscopy
SL	superlattice
SS	stacking sequence
TEM	transmission electron microscopy
TD	threading dislocation
THz	terahertz
TRPL	time-resolved photoluminescence
UHV	ultra high vacuum
QCL	quantum cascade laser
QCD	quantum cascade detector
QW	quantum well
QWIP	quantum well infrared photodetector
XRD	X-ray difraction

Publications and conference contributions

BOOK CHAPTERS

[1] **Infrared Emitters using III-Nitride Semiconductors**
Y. Kotsar and E. Monroy
in *"Nitride semiconductor LEDs: materials, performance and applications",* edited by J. J. Huang, H.-C. Kuo, and S.-C. Shen (Woodhead Publishing Limited, Cambridge, UK, to appear in 2012).

PUBLICATIONS IN INTERNATIONAL JOURNALS

2010

[1] **THz intersubband absorption in GaN/AlGaN step quantum wells**
H. Machhadani, Y. Kotsar, S. Sakr, M. Tchernycheva, R. Colombelli, J. Mangeney, E. Bellet-Amalric, E. Sarigiannidou, E. Monroy, and F.H. Julien
Appl. Phys. Lett. 97, 191101 (2010)

[2] **GaN-based quantum cascade photodetector with 1.5 µm peak detection wavelength**
S. Sakr, Y. Kotsar, S. Haddadi, M. Tchernycheva, L. Vivien, I. Sarigiannidou, N. Isac, E. Monroy, and F. H. Julien
Electron. Lett. 46, 1685 (2010)

[3] **Effect of doping on the mid-infrared intersubband absorption in GaN/AlGaN superlattices grown on Si(111) templates**
P. K. Kandaswamy, H. Machhadani, Y. Kotsar, S. Sakr, A. Das, M. Tchernycheva, L. Rapenne, E. Sarigiannidou, F. H. Julien, and E. Monroy
Appl. Phys. Lett. 96, 141903 (2010)

[4] **Indium kinetics during the plasma-assisted molecular-beam epitaxy of semipolar (11-22) InGaN layers**
A. Das, S. Magalhaes, Y. Kotsar, P. K. Kandaswamy, B. Gayral, K. Lorenz, E. J. C. Alves, P. Ruterana, and E. Monroy
Appl. Phys. Lett. 96, 181907 (2010)

2011

[5] **Strain relaxation in GaN/$Al_xGa_{1-x}N$ superlattices grown by plasma-assisted molecular-beam epitaxy**
Y. Kotsar, B. Doisneau, E. Bellet-Amalric, A. Das, E. Sarigiannidou, and E. Monroy
J. Appl. Phys. 110, 033501 (2011)

[6] **Strain relaxation in GaN/$Al_{0.1}Ga_{0.9}N$ superlattices for mid-infrared intersubband absorption**
Y. Kotsar, P. K. Kandaswamy, A. Das, E. Sarigiannidou, and E. Monroy
J. Crystal Growth 323, 64 (2011)

[7] **III-nitride semiconductors for intersubband devices**
Y. Kotsar, H. Machhadani, S. Sakr, P. K. Kandaswamy, M. Tchernycheva, E. Bellet-Amalric, F. H. Julien, and E. Monroy
Proc. SPIE 7945, 79451D (2011)

[8] **Improved luminescence and thermal stability of semipolar (11-22) InGaN quantum dots**
A. Das, G. P. Dimitrakopulos, Y. Kotsar, A. Lotsari, Th. Kehagias, Ph. Komninou, and E. Monroy
Appl. Phys. Lett. 98, 201911 (2011)

[9] **Si-interdiffusion in heavily doped AlN-GaN-based quantum well intersubband photodetectors**
D. Hofstetter, J. Di Francesco , D. Martin , N. Grandjean , Y. Kotsar, and E. Monroy
Appl. Phys. Lett. 98, 241101 (2011)

[10] **Internal Quantum Efficiency of III-nitride Quantum Dot Superlattices Grown by Plasma-Assisted Molecular-Beam Epitaxy**
Ž. Gačević, A. Das, J. Teubert, Y. Kotsar, P. K. Kandaswamy, Th. Kehagias, T. Koukoula, Ph. Komninou, and E. Monroy
J. Appl. Phys. 109, 103501 (2011)

[11] **Growth and characterization of polar (0001) and semipolar (11-22) InGaN/GaN quantum dots**
A. Das, P. Sinha, Y. Kotsar, P. K. Kandaswamy, G. P. Dimitrakopulos, Th. Kehagias, Ph. Komninou, G. Nataf, P. De Mierry, and E. Monroy
J. Crystal Growth 323, 161 (2011)

2012

[12] **Electroabsorption and refractive index modulation induced by intersubband transitions in GaN/AlN multiple quantum wells**
A. Lupu, M. Tchernycheva, Y. Kotsar, E. Monroy, and F. H. Julien
Optics Express 20, pp. 12541–12549 (2012)

[13] **Resonant Tunneling Transport in a GaN/AlN Multiple-Quantum-Well Structure**
S. Sakr, Y. Kotsar, M. Tchernycheva, E. Warde, N. Isac, E. Monroy, and F. H. Julien
Appl. Phys. Express 5, 052203 (2012)

[14] **Morphology and origin of V-pits in semipolar (11-22) InGaN**
A. Lotsari, A. Das, Th. Kehagias, Y. Kotsar, E. Monroy, Th. Karakostas, P. Gladkov, Ph. Komninou, G.P. Dimitrakopulos
J. Cryst. Growth 339, pp. 1-7 (2012)

[15] **III-nitride intersubband photonics**
S. Sakr, M. Tchernycheva, J. Mangeney, E. Warde, N. Isac, L. Rigutti, R. Colombelli, A. Lupu, L. Vivien, F. H. Julien, A. Vardi, S. E. Schacham, G. Bahir, Y. Kotsar, E. Monroy, E. Giraud, D. Martin, and N. Grandjean
Proc. SPIE 8262, 82621Q (2012)

CONTRIBUTIONS TO INTERNATIONAL CONFERENCES

[1] (Oral) **Study of Indium incorporation during the MBE growth of polar and semipolar InGaN layers**
A. Das, Y. Kotsar, P. K. Kandaswamy, B. Gayral, and E. Monroy
E-MRS Spring Meeting, Strasbourg, France. May 2010

[2] (Oral) **Effect of doping on the mid-infrared intersubband absorption in III-nitride superlattices grown on Si(111) templates**
P. K. Kandaswamy, Y. Kotsar, H. Machhadani, S. Sakr, A. Das, M. Tchernycheva, F. H. Julien, and E. Monroy
E-MRS Spring Meeting, Strasbourg, France. May 2010

[3] (Poster) **Different In incorporation in polar and semipolar InGaN layers during MBE growth**
A. Das, S. Magalhães, Y. Kotsar, P. K. Kandaswamy, B. Gayral, K. Lorenz, E. Alves, and E. Monroy
3rd Int. Symposium on the Growth of III-Nitrides (ISGN3). Montpellier, France. July 2010

[4] (Oral) **Effect of doping on the interband and intersubband properties of III-nitride superlattices grown on Si(111) templates**
Y. Kotsar, P. K. Kandaswamy, H. Machhadani, S. Sakr, A. Das, M. Tchernycheva, F. H. Julien, and E. Monroy
3rd Int. Symposium on the Growth of III-Nitrides (ISGN3). Montpellier, France. July 2010

[5] (Invited) **III-nitride nanostructures for intersubband optoelectronics**
E. Monroy, Y. Kotsar, P. Sinha, A. Das, L. Lahourcade, P. K. Kandaswamy, H. Machhadani, S. Sakr, M. Tchernycheva, and F. H. Julien
3rd Int. Symposium on the Growth of III-Nitrides (ISGN3). Montpellier, France. July 2010

[6] (Oral) **Study of strain relaxation in GaN/AlGaN superlattices for mid-infrared intersubband absorption**
Y. Kotsar, P. K. Kandaswamy, A. Das, L. Rapenne, E. Sarigiannidou, and E. Monroy
16th Int'l Conference on Molecular Beam Epitaxy (MBE2010). Berlin, Germany. August 2010

[7] (Oral) **Growth and characterization of polar (0001) and semipolar (11-22) InGaN/GaN quantum dots**
A. Das, P. Sinha, Y. Kotsar, P. K. Kandaswamy, S. Magalhães, K. Lorenz, E. Alves, and E. Monroy
16th Int'l Conference on Molecular Beam Epitaxy (MBE2010). Berlin, Germany. August 2010

[8] (Invited) **Quantum Cascade Detectors and Emitters**
E. Monroy, Y. Kotsar, and P. K . Kandaswamy, H. Machhadani, S. Sakr, M. Tchernycheva, F. H. Julien, A. Vardi, and G. Bahir
International Workshop on Nitride Semiconductors (IWN-2010), Tampa, USA. September 2010

[9] (Invited) **III-Nitride semiconductors for intersubband devices**
E. Monroy, Y. Kotsar, P. K . Kandaswamy, A. Das, A. Wirthmüller, H. Machhadani, S. Sakr, M. Tchernycheva, F. H. Julien, A. Vardi, and G. Bahir
Photonics West (SPIE), San Francisco, U.S.A. January 2011

[10] (Invited) **Quantum Cascade Detectors based on III-Nitride heterostructures**
E. Monroy, Y. Kotsar, Q. Li, P. K . Kandaswamy, S. Sakr, M. Tchernycheva, and F. H. Julien, A. Vardi and G. Bahir
Photonics West (SPIE), San Francisco, U.S.A. January 2011

[11] (Oral) **Improved luminescence and thermal stability of MBE-grown semipolar (11-22) InGaN quantum dots**
A. Das, Y. Kotsar, A. Lotsari, Th. Kehagias, Ph. Komninou, and E. Monroy
16th European Molecular Beam Epitaxy, Alpe d'Huez, France. March 2011

[12] (Oral) **GaN/AlGaN superlattices grown by PAMBE for intersubband applications in the infrared spectral range**
Y. Kotsar, A. Das, E. Bellet-Amalric, E. Sarigiannidou, H. Machhadani, S. Sakr, M. Tchernycheva, F. H. Julien, and E. Monroy
16th European Molecular Beam Epitaxy, Alpe d'Huez, France. March 2011

[13] (Oral) **Intersubband transitions at THz frequencies in GaN/AlGaN step quantum wells**
S. Sakr, H. Machhadani, Y. Kotsar, M. Tchernycheva, R. Colombelli, J. Mangeney, E. Warde, E. Bellet-Amalric, E. Sarigiannidou, E. Monroy, and F.H. Julien
E-MRS Spring Meeting, Nice, France. May 2011

[14] (Oral) **Plasma-assisted MBE of GaN/AlGaN multiple-quantum-well structures for intersubband optoelectronics**
Y. Kotsar, S. Sakr, E. Sarigiannidou, H. Machhadani, E. Bellet-Amalric, M. Tchernycheva, A. Das, F. H. Julien, and E. Monroy
E-MRS Spring Meeting, Nice, France. May 2011

[15] (Poster) **Ultrafast 1.5 μm GaN-based quantum cascade detector**
S.Sakr, A. Vardi, J. Mangeney, Y. Kotsar, M. Tchernycheva, N. Isac, E. Warde, E. Monroy, G. Bahir, and F.H. Julien
E-MRS Spring Meeting, Nice, France. May 2011

[16] (Oral) **Internal Quantum Efficiency of InGaN quantum dots: Polar vs. Semipolar**
A. Das, A. Lotsari, Y. Kotsar, G. P. Dimitrakopulos, Th. Kehagias, Ph. Komninou, and E. Monroy
E-MRS Spring Meeting, Nice, France. May 2011

[17] (Poster) **Plasma-assisted MBE of GaN/AlGaN multiple-quantum-well structures for intersubband optoelectronics**
Y. Kotsar, S. Sakr, E. Bellet-Amalric, H. Machhadani, B. Doisneau, E. Sarigiannidou, M. Tchernycheva, A. Das, F. H. Julien, and E. Monroy
9th International Conference on Nitride Semiconductors (ICNS9), Glasgow, UK. July 2011

[18] (Poster) **Latest developments towards GaN/AlGaN THz quantum cascade lasers**
F. H. Julien, H. Machhadani, S. Sakr, M. Tchernycheva, R. Colombelli, E. Warde, J. Mangeney, Y. Kotsar, E. Bellet-Amalric, E. Sarigiannidou, and E. Monroy
9th International Conference on Nitride Semiconductors (ICNS9), Glasgow, UK. July 2011

[19] (Oral) **Ultrafast GaN-based quantum cascade detector at record short infrared wavelength**
S. Sakr, A. Vardi, Y. Kotsar, M. Tchernycheva, L. Vivien, J. Mangeney, N. Isac, E. Monroy, and F. H. Julien
9th International Conference on Nitride Semiconductors (ICNS9), Glasgow, UK. July 2011

[20] (Poster) **Plasma-assisted MBE of semipolar (11-22)-oriented III-nitrides: 2D layers and nanostructures**
A. Das, Y. Kotsar, L. Lahourcade, G.P.Dimitrakopulos, Th. Kehagias, A. Lotsari, T. Koukoula, Ph. Komninou, and E. Monroy
9th International Conference on Nitride Semiconductors (ICNS9), Glasgow, UK. July 2011

[21] (Invited) **Latest developments towards GaN/AlGaN THz quantum cascade lasers**
F. H. Julien, H. Machhadani, S. Sakr, M. Tchernycheva, R. Colombelli, E. Warde, J. Mangeney, Y. Kotsar, E. Bellet-Amalric, E. Sarigiannidou, E. Monroy
9th International Conference on Nitride Seminconductors (ICNS-9), Glasgow, UK, July 2011

[22] (Oral) **Latest developments in GaN-based short-infrared-wavelength quantum cascade detectors**
S. Sakr, A. Ghrib, M. Tchernycheva, J. Mangeney, L. Vivien, N. Isac, F. H. Julien, A. Vardi, G. Bahir, Y. Kotsar, E. Monroy, A. Dussaigne, E. Giraud, and N. Grandjean
Int. Conf. on Intersubband Transitions in Quantum Well (ITQW'11), Badesi, Italy. Sept. 2011

[23] (Oral) **Latest developments towards GaN/AlGaN THz quantum cascade lasers**
F. H. Julien, S. Sakr, H. Macchadani, M. Tchernycheva, R. Colombelli, E. Warde, J. Mangeney, Y. Kotsar, E. Bellet-Amalrci, E. Sarigiannidou, and E. Monroy
Int. Conf. on Intersubband Transitions in Quantum Well (ITQW'11), Badesi, Italy. Sept. 2011

[24] (Invited) **Fabrication and Characterization of Al(Ga)N/GaN ISB Devices**
E. Monroy, Y. Kotsar, A. Das, S. Valdueza-Felip, P. K. Kandaswamy, R. Songmuang, S. Sakr, M. Tchernycheva, F. H. Julien, E. Gross, A. Pesach, and G. Bahir
Int'l Workshop on SMART Energy Harvestin and Saving with III-Nitride Semiconductors "Frontier of Nitride Semiconductor Alloy Photonics (NSAP 2012), Chiba, Japan. May 2012

[25] (Invited) **Strain relaxation in GaN/AlGaN superlattices grown by PAMBE for intersubband applications**
B. Doisneau, Y. Kotsar, E. Sarigiannidou, E. Bellet-Amalric, A. Das, and E. Monroy
Extended Defects in Semiconductors EDS2012. Thessaloniki, Grece. June 2012

[26] (Invited) **GaN quantum devices for infrared optoelectronics**
E. Monroy, Y. Kotsar, A. Das, S. Valdueza-Felip, E. Bellet-Amalric, C. Bougerol, R. Songmuang, L. Rapenne, E. Sarigiannidou, S. Sakr, M. Tchernycheva, F. H. Julien, E. Gross, A. Pesach, and G. Bahir
4th Int. Symposium on the Growth of III-Nitrides (ISGN4), St. Petersburg, Russia. July 2012

[27] (Submitted) **Electroabsorption and refractive index modulation induced by intersubband transitions in GaN/AlN heterostructure waveguides**
A. Lupu, S. Sakr, Y. Kotsar, M. Tchernycheva, N. Isac, E. Monroy, and F. H. Julien
Photonics West (SPIE), San Francisco, U.S.A. January 2013

This work reports on electronic design, epitaxial growth and characterization of GaN/Al(Ga)N quantum wells which constitute the active region of intersubband (ISB) devices for near-, mid- and far-infrared. The design of the GaN/Al(Ga)N quantum wells to tune the ISB transitions in the infrared spectrum was performed using the 8-band k.p Schrödinger-Poisson Nextnano^3 solver. The investigated structures were synthesized using plasma-assisted molecular beam epitaxy (PAMBE).

The strain issues arising due to the lattice mismatch during the epitaxial growth of GaN/Al(Ga)N heterostructures are investigated by combination of *in-situ* and *ex-situ* techniques. The optimal buffer layer, Al content and relaxation mechanisms during the PAMBE growth are determined. Achieving efficient ISB absorption at longer wavelengths requires heavy silicon doping of the quantum wells, so that the single-particle theory leads to a large discrepancy with the experimental results. Therefore, a study of silicon doping of GaN/Al(Ga)N superlattices for near- and mid-infrared spectral region are presented.

This work also contributes to a better understanding of the infrared quantum cascade detector technology. Relevant achievements of room-temperature detection at 1.5 µm and 3-5 µm spectral range are demonstrated. Finally, the first observation of far-infrared (4.2 THz) ISB absorption in III-nitrides is reported.
Keyworkds: Nanostructures, nitrides, molecular beam epitaxy, intersubband, infrared

---

Ce mémoire résume des efforts dans la conception électronique, la croissance épitaxiale et la caractérisation des puits quantiques GaN/Al(Ga)N qui constituent la région active des composants inter-sous-bande (ISB) à base de semi-conducteurs nitrures pour l'optoélectronique dans l'infrarouge proche, moyen et lointain. Le dessin des puits quantiques GaN/Al(Ga)N pour ajuster la longueur d'onde d'absorption dans le spectre infrarouge a été réalisé en utilisant la méthode k.p à 8 bandes du logiciel Nextnano3 pour la résolution des équations de Schrödinger-Poisson. Les structures ont été synthétisées par épitaxie par jets moléculaires assistée par plasma (PAMBE).

Les problèmes de gestion de la contrainte qui apparaissent liés au désaccord de maille pendant la croissance épitaxiale des hétérostructures GaN/Al(Ga)N ont été investigués par combinaison de techniques *in-situ* et *ex-situ*. La couche tampon optimale, la teneur en aluminium et les mécanismes de relaxation pendant la croissance par PAMBE ont été déterminés. Pour obtenir une absorption ISB efficace, on a besoin de niveaux élevés de dopage au silicium dans le puits quantiques, situation dans laquelle les théories à une particule conduisent à des déviations significatives par rapport aux résultats expérimentaux. Donc une étude du dopage au silicium des super-réseaux GaN/Al(Ga)N pour les régions spectrales infrarouges proche et moyen est présentée.

Ce travail contient aussi une contribution à la compréhension de la technologie de photodétection à cascade quantique. Des résultats importants tels que l'obtention de photodétecteurs cascade fonctionnant à 1.5 µm et dans la plage spectrale de 3-5 µm sont démontrés. Finalement, on décrit la première observation de l'absorption ISB dans l'infrarouge lointain (4.2 THz) utilisant des nanostructures à base de semi-conducteurs nitrures.
Mot clés : Nanostructures, nitrures, épitaxie par jets moléculaires, inter-sous-bande, infrarouge